LOCAL STRESSES IN PLATED STRUCTURES

A Thesis presented for the Degree of Ph.D. (Engineering)

in the University of London

by

Suraj Prakash Sarna, B.E. (Hons), D.I.C.

Imperial College of Science and Technology,
London

January, 1966

ABSTRACT

This thesis deals with some problems of local and general stress distribution in the presence of certain discontinuities that occur in ship structures.

Photoelasticity and experiments on a steel model have been used to arrive at a new shape of cut-out which considerably reduces the stress concentration at the root of expansion joints in superstructures. Finite difference displacement solutions have been obtained to calculate the effect of the depth of a cut (representing an expansion joint) on the general stress distribution in idealised plate-projections. A method of grading the net close to discontinuities has been used to find the stress distribution in these regions.

The effect of certain geometrical parameters on the elastic stress concentration factor in plates with rectangular openings (representing hatch openings in ships) has been studied experimentally. The general stress distribution was found by using the finite difference method. Machined specimens of ship steel with rectangular openings have been tested under repeated loading in the high cycle as well as the low cycle range. The fatigue strength reduction factor is correlated with the elastic stress concentration factor taking into account the geometrical size-effect. The correlation was found to be good. Using the existing theories the probable fatigue behaviour of a large-size plate with a square opening was studied.

TO MY PARENTS

ACKNOWLEDGEMENT

The work described in this thesis was carried out in the Civil Engineering Department of Imperial College under the direction of Dr. J. C. Chapman as part of a programme of research on ship structures sponsored by the British Ship Research Association.

The author is greatly indebted to Dr. J. C. Chapman for his valuable suggestions, constant guidance and encouragement.

The author is also deeply grateful to Professor S. R. Sparkes for the opportunity to take part in the research programme.

The author wishes to thank Messrs. J. Neale, N. Scott and P. J. D. Guile and other members of the structures laboratory and workshop staff for their help with the experimental work.

The author wishes to express his thanks to his friends and colleagues for their help, particularly Mr. P. F. Taylor, also to Dr. A. K. Basu, Dr. H. C. Chan, Mr. D. Williams and Dr. P. Krishna. Special thanks are also due to Messrs. A. Duke, S. H. Gadre, H. R. Milner, K. A. Segun, and H. K. Sen.

Special thanks are due to Miss C. Beresford for typing the thesis, Miss J. Gurr for taking the photographs, and Mrs. J. Hotten of the Mechanical Engineering Department for taking the surface finish records.

The author wishes to record his gratitude to the Government of Madhya Pradesh (India) and the Ministry of Overseas Development of the Government of the United Kingdom for granting him the study leave and scholarship which enabled his post-graduate study and research at the Imperial College, London.

CONTENTS

Page No.

SECTION II

HATCH OPENINGS

Experiments

Theory

INTRODUCTION

General

The static failure of a ductile structure or component in tension is generally governed by the average value of stress over the load-bearing area, and not by local stress concentrations. The condition becomes quite different if the structure is subjected to repeated loads. Although the average stress level may be quite small, local concentrations of stress may lead to failure by fatigue. This is because the failure of metals by fatigue depends mainly on the maximum value of the stress and not on the average value. The study of stress concentrations therefore becomes important for structures subjected to repeated loads. Aircraft, ships, bridges and machines may be quoted as examples of such structures.

Stress concentrations are caused by discontinuities such as holes or changes of section in shafts, hatch openings, superstructures or expansion joints in ships. It is difficult to eliminate stress concentrations completely from a structure with discontinuities, but attempts are made to reduce their severity.

Stress concentration studies date back to the middle of the nineteenth century when Rankine [1] gave an explanation for railway axle failures. Since then, a vast amount of research has been done in studying and reducing stress concentrations occurring in various engineering structures and machines. A large number of

problems of stress concentrations arising out of simple geometrical discontinuities have been solved theoretically. Experimental techniques such as brittle coatings, strain gauging and photo-elasticity have been developed and used for investigating stress concentrations. Data sheets and handbooks giving geometrical stress concentration factors have been prepared from the results of the theoretical and experimental investigations.

This thesis is concerned with certain discontinuities which occur in ship structures. The resulting stress concentrations are investigated by experimental and numerical methods; in the case of hatch openings their effect on fatigue strength is considered. The review of literature which follows is limited to that which is directly relevant to these topics.

Superstructures

A long superstructure, being of light construction for reasons of stability, will be subjected to heavy stresses because of its distance from the neutral axis of the hull girder. It is sometimes the practice to introduce "expansion joints" in the form of cuts in order to reduce the stress. The introduction of an expansion joint causes a high stress concentration at the root, and a crack commonly develops at this point as a consequence.

The effect of expansion joints has been studied experimentally on a box structure [2] and measurements on actual ships [3] show that the stress at the top of the deckhouse may be reduced almost

to zero. There is no general agreement as to whether expansion joints should be provided and where they are used there is no accepted basis for determining their depth and spacing. There is no general theory for determining the overall or local stresses (which are interrelated) in the presence of expansion joints, although the short superstructure has been treated [4].

The contribution which a superstructure or a deckhouse makes to the overall longitudinal strength of a ship depends upon a number of factors, such as the length and width of the superstructure, the transverse stiffness of the hull and the nature of bending moment applied. Neglecting the effect of shear lag and applying the simple theory of bending separately to the superstructure and the hull, the effect of some of the factors has been studied theoretically and by model experiments [5] [7]. An energy method has also been applied to calculate stresses in deckhouses [6].

The superstructure is loaded at its lower edge by shearing and vertical forces which impose a longitudinal and vertical displacement on this edge. The sides of the superstructure can be to some extent idealised as a plate-projection, and the relaxation technique has been used to find the stresses in plate projections subjected to constant strain or constant curvature

at the boundary [8]. In this thesis the effect of cuts in plate projections has been studied numerically with the help of the Atlas computer. A method of grading of net is indicated for finding the stress distribution near the end of a projection or a cut.

Investigations on a passenger liner of 24000 tons with one expansion joint were made during the acceptance trial [9]. Measurements were taken on two alternative stress relieving cut-outs. Stress concentration factors of 17 and 8.6 were observed and cracks developed during this initial voyage. Similar cracks were reported in S.S. Leviathan [10]. Various types of stress relieving device have been studied at Imperial College and measurements on a new type of anchor-shaped cut-out are described in this thesis [11].

Hatch openings

The high stresses occurring at the corners of hatch openings are well known and have caused a large number of failures. During World War II, Liberty ships were made with sharp hatch corners and there were 10 hatch corner failures per 100 shipyears [1]. Attempts to understand and reduce stress concentrations around hatches have since been made. A considerable amount of theoretical and experimental work has been reported. Efforts are now being made to apply the knowledge to actual practice by the ship classification societies by specifying minimum corner radii [26]. Full scale welded hatch corners have been tested to determine the effectiveness of the various modifications used [12]. The complex variable technique has been used to investigate the stress distribution around simple and reinforced rectangular openings [13], [14]. Photoelastic investigations have been made to study the effect of various parameters on stress concentration at the corner of a rectangular opening in a plate of finite width [15]. Using the results of photoelastic investigations, attempts have been made to arrive at empirical relations for calculating stress concentration factors [16]. Some tests on model steel decks have been reported [6]; and others are being conducted by the British Ship Research Association to study the effect of various geometrical and structural parameters (e.g. insert plates, coamings) [17].

An empirical formula (taking account of the geometrical parameters) for the calculation of stress concentration factors has been suggested [18]. Measurements on actual ships have been taken to correlate them with model studies [6], [19].

In all the above investigations, only the geometrical stress concentration factors have been studied, but the effect of various parameters on the fatigue behaviour has not been investigated. Whereas the geometrical stress concentration factor is a function of the geometry of the discontinuity and is valid for any stress within the elastic limit, the reduction of fatigue strength depends upon a number of factors. For example, the volume of highly stressed material, the amount of plastic deformation, the size of the specimen and the presence of residual stresses are all important factors. A study of the effect of some of the parameters on the fatigue behaviour of small plate specimens is reported in this thesis. An attempt is made to correlate the fatigue behaviour with the geometrical stress concentration factor taking into account the geometrical size-effect. The stress concentration has been found experimentally. The general stress distribution in the plate has been found by the finite difference method using the Atlas computer.

Fatigue in ship structures

The importance of fatigue in ship structures has been the subject of discussion and controversy for some years. The views generally held in this country have been at variance with those held on the continent [20]. At the international conference on fatigue of metals (1956), out of about 80 papers presented, only one (by Russian authors [21]) was on fatigue in ships. It has been suggested that fatigue failures have not been recognised because pressure for immediate repairs to enable ships to continue their voyages has prevented detailed investigation of the nature of cracks found in practice [20]. After the second world war, in a survey of 210 tankers 66 were found to have cracks in deck or shell and of these 65 were considered to be due to fatigue [22]. It is now generally recognised that fatigue cracks do occur in ships [23] [34].

A ship is subjected to reversals of longitudinal bending moment in service. The cumulative frequency distribution found in certain ships [24] can be approximated to a straight line if the logarithm of the number of reversals is plotted against the stress levels at which they take place. A small number of reversals take place at a high stress level and cause cracking at points of stress concentrations. This low cycle fatigue phenomenon in ships has received some attention in recent years [25]. However, the damaging effect of the reversals

at lower stress levels can not be ignored. Assuming a straight line spectrum and applying Miner's cumulative damage law it can be shown that the damage rate is considerable at low stress levels. Although the Miner's hypothesis provides a method of determining the life under random loading condition, its applicability is itself a subject of discussion. It does not take into account the damaging effect of stresses below the endurance limit, and takes no account of the sequence of stress cycles. There is evidence to believe that these factors do have effects on the fatigue life [34][35]. In some parts of the ship, fatigue is likely to be caused by vibrations from machinery or pressure pulses from the screw. The problem will become more important with the use of high tensile steel which will result in higher design stresses without any increase in fatigue strength. The damaging effect of discontinuities on fatigue life is further aggravated by additional concentrations created by welding.

Perhaps the most realistic approach to the fatigue problem in ships is the programmed fatigue testing of full size structural elements under corrosive conditions. This will require extremely elaborate testing arrangements and may still not take into account the restraints exerted on the element when it is part of a ship. Due to the scatter inherent in all fatigue testing, it may sometimes seem difficult to draw too definite conclusions from

such tests unless several of them are done. Tests on smaller specimens on the other hand give the possibility to compare the effect of different parameters even though they fall short of providing a firm basis for predicting the fatigue strength of a structural detail in service.

To investigate the fatigue performance of different types of detail, tests on large-size structural components have been carried out [28] [29] and tests on the fatigue behaviour of welded stiffeners have been reported [30]. Tests on small machined specimens of ship steel to study the general low-cycle fatigue phenomenon and crack propagation have been conducted [31][32].

Some tests to study the effect of fatigue damage on brittle fracture properties of ship steel are reported [33] and others are in progress [25].

The tests on small size idealised laboratory specimens reported in this thesis are intended to throw light on the relative importance of various parameters (such as radius or length of a hatch) under fatigue loading in the low cycle as well as the high cycle range. The fatigue strength reduction factor is correlated with the elastic stress concentration factor taking account of the geometrical size-effect.

SECTION I

SUPERSTRUCTURES

EXPERIMENTS

It is necessary to keep the superstructure weight low for reasons of stability. A light superstructure has only a limited influence on the level of the neutral axis of the ship girder and it follows that the stresses at the top of the superstructure may be large. It is sometimes the practice to reduce the stresses in the top of the superstructure by providing "expansion joints".

The structural discontinuity so introduced inevitably gives rise to a stress concentration and cracking is commonly initiated from the root of the joint. Some relief of the concentration can be obtained by introducing a cut-out, but nevertheless stresses up to seventeen times the nominal stress have been observed in a ship at sea.[9] Improvements can be made by modifying the design of the cut-out and the purpose of this investigation was to determine the form of cut-out which gives the greatest reduction in stress concentration.

Photoelastic Experiments

The superstructure stress does not vary greatly over the depth of the expansion joint, and a qualitative appreciation of the problem can be obtained by considering the applied stress to be uniform. The problem can be further simplified by the use of a single plate model; such a model does not represent exactly the conditions found in a ship, but it is reasonable to suppose that a device which relieves the concentration in the model will have a similar effect in a ship.

Photoelasticity provides a convenient means of estimating the variation of stress concentration with the shape of a cut-out, since the position, as well as the magnitude, of maximum stress is determined at once from the fringe pattern. If care is used in the machining the same model can be used for a number of different cut-outs.

The purpose of these tests was to study the variation of magnitude and position of maximum stress concentration with the length of a circular cut-out and the effect of providing a cut-out in the form of a curve with linearly varying curvature.

The stress concentration at the end of a U-shaped notch depends on the ratio of the depth of notch to the end radius, and if the stress concentration were to be limited to about 2.0 it would be necessary to make the radius of the same order as the depth.

Thus in the case of a ship's superstructure, a radius giving an acceptable stress concentration would result in an unduly wide slot. Attempts have sometimes been made to obtain the benefits of an increased radius without recourse to a wide slot by designing anchor shaped cut-outs.

In an anchor shaped cut-out the maximum stress concentration may occur at the centre or near the ends, depending upon the relative curvatures and the overall proportions of the anchor. Figure 1 shows results obtained at Imperial College on anchor cut-outs.[11] It is clear that any further substantial reduction would be dependent upon increasing the overall dimensions of the anchor rather than by modifying the shape of the small anchor.

The photoelastic specimens were cast in the form of 12" square plates using Araldite resin CT 200 with 28 per cent hardener HT 901. The cut-outs were made by using a high speed diamond cutter which copied the pattern from a template on a pantagraph machine. The plate was submerged in cooling water during the cutting operation.

Testing Procedure

Experiments were carried out with symmetrical cut-outs in Araldite sheets which were loaded in tension (Figure 2) The loads were applied hydraulically and measured by strain gauges on a calibrated link. The loading frame proper was contained within an outer frame relative to which it could be moved vertically or horizontally so that any part of the model could be situated within the field of the polariscope. (Figure 3)

The fringe pattern was projected on to a small screen and the emergence of successive fringes was noted as the load was gradually increased. The fringes were also recorded photographically, and typical patterns are shown in Figures 4 and 5 . Both cut-outs on opposite sides of the plate were observed as a check on the symmetry of loading.

The fringe order is proportional to the difference of the two principal stresses. The point of maximum stress concentration occurs at the free boundary where the normal stress is zero. Stress concentration factors can therefore be readily determined by knowing the fringe order and the average applied stress on the net section of the plate.

The first anchor shape considered was based on a slot in the form of a circular arc having its centre on the edge of the plate at the top of the slot. The arms of the anchor were gradually increased in length until they reached the edge of the plate and formed a U-notch of radius equal to its depth (Specimen 1, Figure 6). The plate thickness was 0.261 in.

Consideration was also given to the possibility of reducing the concentration factor by using a curve with linearly varying curvature (a highway transition curve) instead of a semicircle. Accordingly Specimen 2 was designed with a cut-out shape as shown in Figure 6 . The plate thickness was 0.128 in.

Test results

The position and magnitude of maximum stress concentration is shown in Figure 6 and Table 1 . The concentrations are shown as a multiple of the average applied stress σ_N.

As the length of the anchor arm is increased from zero, the point of maximum stress concentration shifts from the centre to near the ends and then back to the centre. The magnitude of the maximum concentration approaches a limiting value of 2.09 which may be compared with Peterson's theoretical value [37] of 1.88.

In the case of the transition curve cut-out a slight reduction in the stress concentration was noted and the stress along the bottom of the cut-out was almost uniform, but there was no marked improvement relative to the semicircular cut-out.

Experiments on a steel model

With the photoelastic equipment and materials available the size of specimen was limited, and since the smallest diamond milling cutter obtainable for cutting the slot was one eighth of an inch in diameter it was not possible to represent to scale an anchor with a very narrow slot such as might be used in practice, so consideration was given to designing the model in steel. Cutters down to one sixteenth of an inch were obtainable, and as the specimen size could be much increased the ratio of depth to width of slot could be made larger.

The photoelastic experiments were primarily intended to give a qualitative appreciation of the effect of differently shaped anchor cut-outs on the maximum stress concentration and for simplicity the experiments were limited to loading in direct tension. For the more realistic slot proportions of the steel specimen, the loading and dimensions were chosen to give a linear distribution of strain over the depth of the slot, such as would be present in an actual superstructure expansion joint. Thus in Specimen 3 (Figure 7) the cut-out was made in a flanged plate projection welded to the top flange of a heavy steel I-beam. The

dimensions of the projection were chosen so that the stress distribution over its depth was similar to that existing in a ship's superstructure. In actual ships the relative depth of expansion joint to superstructure height shows a very wide variation. The depth of slot chosen for the model relative to the superstructure height is approximately at the middle of the range noted.

In practice an expansion joint slot may be perhaps one inch wide and twenty feet long, so that the radius at the end of the anchor arms will be very small relative to the depth of the slot and it is likely therefore that the maximum stress concentration will be much higher than the values measured in the photoelastic experiments already described. It is also likely that the point of maximum stress concentration will remain at the ends of the anchor however long the arms may be made.

From a design point of view the stress concentration factor is of less importance than the actual maximum stress, and it follows that if a stress raiser such as a sharp radius can be situated in an area of low stress, the stress level due to the concentration may still be acceptable. The modified anchor shape used for Specimen 3 (Figure 8)

was based on these considerations. By making the anchor arm in the form of a spiral the sharp end radius was removed to a region where the stress was expected to be negligible.

Testing Procedure

Specimen 3 was loaded as shown in Figures 7 and 11 with the complete length of the superstructure subjected to pure bending. Strains were measured by electric resistance strain gauges using a high speed automatic strain recorder. Around the periphery of the slot the gauges were of 3mm. gauge length; elsewhere they were of 0.5 in. gauge length. Opening of the slot was measured at four positions by a two inch gauge length mechanical gauge spanning the slot.

The projection of Specimen 3 is unstiffened. Stiffeners would reduce the vertical movements and would alter the stress distribution. In order to obtain a qualitative assessment of the effect of stiffening, measurements were made with vertical restraining forces applied to the projection at the top of the slot as indicated in Figures 10 and 12 . The restraining forces applied were sufficient to reduce the movement at C to zero.

Test results

Distributions of longitudinal stress are shown in

Figure 9 for a section midway between the end of the projection and the expansion joint, and for the section in way of the joint. The fall-off in stress in the projection clear of the expansion joint and the increase at the joint are clearly shown.

The distribution of tangential stress around the cut-out is shown in Figure 10. With vertical movement unrestrained the maximum stress concentration defined relative to the simple bending stress on the net section at the base of the slot occurs towards the ends of the bottom part of the anchor, and has a value of 3.0, whilst the stress concentration at the bottom of the slot has been reduced to 1.4. The peak value could no doubt be further reduced by redistributing the curvature to make the stress along the length of the anchor more uniform. It appears that the length of spiral is greater than necessary. Vertical restraint tends to make the stresses along the base of the anchor more uniform, but the effect is small; towards the end of the anchor spiral the stress is reversed.

Movements across the slot are also shown in Figure 10. The movement of .017 in. at the top of the projection would correspond to about 0.4 in. full scale (at the same stress level); this movement is necessarily associated with the reduction in superstructure stress.

THEORY

The experiments described above indicate that a considerable reduction in stress concentration may be obtained by modifying the shape of the cut-out at the root of an expansion joint. There are, however, other factors such as the depth and number of cuts, the distance between the cuts and the length of the superstructure which not only affect the stress concentration at the root of the cut but also the general stress distribution in the superstructure. The general superstructure problem is thus closely connected to the problem of local concentrations at the roots of the expansion joints or at the ends of the superstructure.

The lower edge of a superstructure is loaded by shearing and vertical forces from the main deck. The resulting longitudinal and vertical displacements impose a longitudinal strain as well as a curvature on the superstructure base. The variation of the displacements of the lower edge of the superstructure depends upon the bending moment applied and the distortions of the hull. For the purpose of analysis, however, it has been assumed that the strain and curvature at the junction are each uniform along the length of the superstructure. These assumptions, though approximate,

can to some extent be justified by the fact that the plating in the superstructure is thinner than that in the main hull, so that the superstructure displacements do not greatly affect the longitudinal bending of the hull. On the basis of these assumptions, the sides of the superstructure have been idealised as a rectangular plate projection subjected to constant strain or constant curvature at the lower boundary.(8) A similar approach is made in this section to study the effect of the depth of a cut (representing an expansion joint) in a plate projection. A method of grading of nets is indicated for finding the local stress distribution near the ends of a superstructure or near the base of a cut. Displacement solutions have been obtained and a stress-function approach is indicated.

Effect of depth of cut in Plate Projections

Displacement solutions have been obtained for rectangular plates having partial cuts at the centre and with imposed displacements at the lower edge. The equations of equilibrium and compatability in terms of displacements in two directions are expressed in terms of finite differences and are solved by means of the computer.

The longitudinal, transverse and shear stresses in a plate may be expressed in terms of displacements by the equations

$$\sigma_x = \frac{E}{(1-\rho^2)}\left[\frac{\partial u}{\partial x} + \rho\frac{\partial v}{\partial y}\right]$$
$$\sigma_y = \frac{E}{(1-\rho^2)}\left[\frac{\partial v}{\partial y} + \rho\frac{\partial u}{\partial x}\right]$$
$$\tau_{xy} = \frac{E}{2(1+\rho)}\left[\frac{\partial u}{\partial y} + \frac{\partial v}{\partial x}\right] \qquad \text{.....(1.1)}$$

The equilibrium equations are

$$\frac{\partial \sigma_x}{\partial x} + \frac{\partial \tau_{xy}}{\partial y} = 0$$
$$\frac{\partial \sigma_y}{\partial y} + \frac{\partial \tau_{xy}}{\partial x} = 0 \qquad \text{.....(1.2)}$$

The following equations may be derived by substituting for σx etc. from (1.1)

$$2\frac{\partial^2 u}{\partial x^2} + (1-\rho)\frac{\partial^2 u}{\partial y^2} + (1+\rho)\frac{\partial^2 v}{\partial x \partial y} = 0$$
$$2\frac{\partial^2 v}{\partial y^2} + (1-\rho)\frac{\partial^2 v}{\partial x^2} + (1+\rho)\frac{\partial^2 u}{\partial x \partial y} = 0$$

.....(1.3)

These equations together with the boundary conditions expressed in terms of displacements enable the displacements to be obtained at all points of a grid.

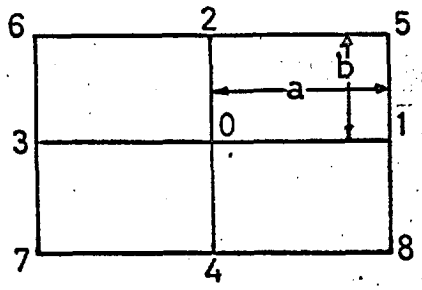

In a rectangular grid the following finite difference relations may be derived by using Taylor series

$$2a\frac{\partial u}{\partial x} = u_1 - u_3 \quad ; \quad 2b\frac{\partial u}{\partial y} = u_2 - u_4$$

$$a^2\frac{\partial^2 u}{\partial x^2} = u_1 + u_3 - 2u_0$$

$$b^2\frac{\partial^2 u}{\partial y^2} = u_2 + u_4 - 2u_0$$

$$4ab\frac{\partial^2 u}{\partial x\,\partial y} = u_5 - u_6 + u_7 - u_8 \qquad \text{.....(1.4)}$$

Putting $\frac{b}{a} = k$ the equations (1.3) can then be written as

$$2k^2(u_1+u_3-2u_0)+(1-\rho)(u_2+u_4-2u_0)+0{\cdot}25(1+\rho)k(v_5-v_6+v_7-v_8)=0$$

$$2(v_2+v_4-2v_0)+(1-\rho)k^2(v_1+v_3-2v_0)+0{\cdot}25(1+\rho)k(u_5-u_6+u_7-u_8)=0$$

.....(1.5)

Due to the symmetry of the plate, one half of the plate was divided into a 4 x 4 mesh as shown in Figure 13 . There are two equations to be solved at each mesh point. This particular mesh size was chosen to keep the size of the matrix small, since the program for solving the equations was to be written for the Mercury computer. A much finer mesh, however, can be dealt with by the Atlas computer. The computer program generated the coefficients of the matrix for any value of k to give solutions for any aside ratio of the plate, and solved the simultaneous equations to give displacements at each point. The values of the imposed displacements at grid points on the lower boundary of the plate were fed in to the program as data.

Boundary Conditions

At the free boundaries the fictitious external values of u and v were expressed in terms of the unknown displacements inside the plate, and the relations so obtained were fed into the equations at the boundary.

The relations can be obtained from equation (1.1)

At the top edge

$$\sigma_y = 0$$

$$\tau_{xy} = 0$$

At the ends

$$\sigma_x = 0$$

$$\tau_{xy} = 0$$

At the top edge

$$v_2' = v_4 - \rho k(u_1 - u_3)$$

$$u_2' = u_4 - k(v_1 - v_3)$$

At the ends

$$u_3' = u_1 + \frac{\rho}{k}(v_2 - v_4)$$

$$v_3' = v_1 + \frac{1}{k}(u_2 - u_4) \qquad \text{.....(1.6)}$$

At a corner the first and the third equation of (1.6) give

$$u_3' = u_1$$

$$v_2' = v_4$$

The second and the fourth relation of (1.6) give

$$(u_2' - u_4) + (v_1 - v_3')k = 0 \qquad \text{.....(1.7)}$$

Thus there are two fictitious values u_2' and v_3' to be determined from one equation.

An extrapolation was used to obtain the two values. u_2' was parabolically extrapolated in terms of unknown displacements at the edge of the plate and relation (1.7) was used to obtain a relation expressing v_3' in terms of unknown displacements. Similarly v_3' was parabolically extrapolated and equation (1.7) was used to derive a second relation expressing u_2' in terms of unknown displacements. Thus a pair of expressions were obtained for u_2' and v_3' . The mean of the two expressions obtained was fed into the equations.

The corner values u_6' and v_6' were parabolically extrapolated on a diagonal line.

The boundary conditions and extrapolations are indicated in Figure 13 . The stress condition assumed at the bottom of the cut was $\sigma_{y=0}$, $\tau_{xy=0}$.

To find the stresses at the lower boundary it is necessary to calculate the fictitious boundary values. These values were calculated by applying the equilibrium equations (1.5) after the displacements at all points have been calculated. It was assumed at the corner that

$$u_4' - u_0 = u_0 - u_2$$

$$v_4' - v_0 = v_0 - v_2$$

The assumption at the corner has little effect away from the corner.

Theoretical results, experimental confirmation and discussion

The effect of depth of cut on displacements for a 1:4 plate with constant strain or constant curvature imposed at the lower boundary is shown in Figure 14 . (Other results are tabulated in the appendix). Figure 15 shows the effect of depth of a central cut on the maximum longitudinal stress at the top of plate projections having different side ratios with constant strain or constant curvature imposed along the base. As the purpose of introducing cuts in superstructures is to reduce the stresses at top deck level, this level has been chosen for the purpose of comparing the stress-relieving effect of the cuts, even though higher stresses do occur in the region of the bottom of the cut. Means of relieving this stress concentration are considered separately. As the depth of cut increases, the maximum stress at the top decreases. For a depth approaching the depth of the projection, the stresses approach the value corresponding to a plate projection with a length/height ratio half that of the original projection.

An experiment was done to verify some of the theoretical results obtained. A perspex plate 18 x 7 $\frac{1}{2}$ in. and 3/16 in. thick was cemented and tightly clamped between two steel bars 1 $\frac{1}{2}$ x $\frac{1}{4}$ in. in cross-section (Figure 16). To prevent slip

over the test length the plate was extended within the steel bars beyond each end of the projection. The model simulated the boundary conditions of constant strain and zero curvature imposed along the base of a projection of side ratio 1:6. The extensional stiffness of the bars was about forty times that of the projecting perspex. Resistance strain gauges were fixed to the perspex plate at two cross-sections which corresponded to two grid lines of the mesh used in the theoretical analysis. Strain gauges were also fixed on the steel bars at these sections. The bars were stretched in a testing machine and strains were recorded. Control gauges were used to check the symmetry of the load. Cuts were made symmetrically in the middle of the projection. The depth of cut was increased in stages and strains measured. After the final stage of the cut, the projection was shortened to give a side ratio of 1:4. Figure 17 shows the theoretical and experimental strains for the 1:6 plate for different depths of cut. Figure 18 shows the results for the final stage of the cut for the 1:4 plate. In both cases the correlation is good in spite of the coarse mesh used.

Example

The use of the curves in Figure 15 is illustrated with the help of an example below. The Figure below shows a plate projection (A) of side ratio 1:6 attached at its lower edge to a plate (B) which is twice as deep as the projection and has a flexural stiffness very large compared to that of (A). It may be assumed that the plate (B) is subjected to a uniform bending moment. The neutral axis of the combination can be assumed to lie at the middle of the plate (B) as it is very stiff compared to (A). It is required to calculate the depth of a central cut (p) to reduce the maximum longitudinal stress at the top of the projection to a value 50 per cent. of that at its base. (i.e. 25 per cent. of the simple bending value at the top).

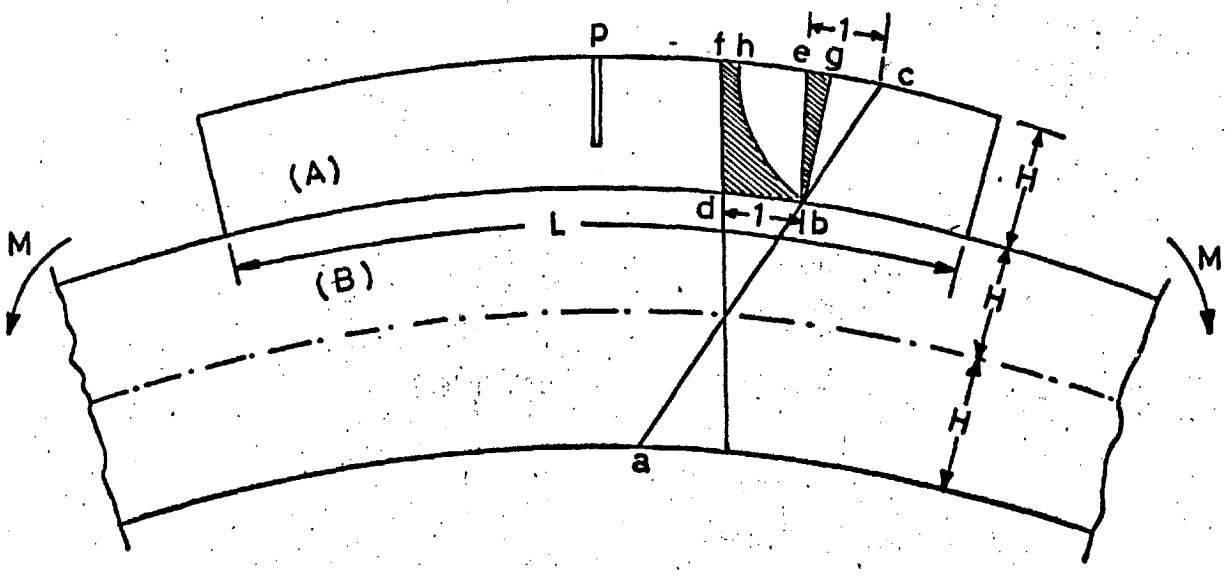

The linear stress distribution abc would result if the projection (A) was infinitely long compared to its height.

The plate projection can be assumed to be subjected to a unit longitudinal stress at its base (taking bd = 1) and a simple bending stress distribution represented by the triangle bfc (fc = 1 by geometry). The shaded areas indicate the resulting stress distribution.

Referring to Figure 15 (b) the ordinate for 1:6 plate with a cut of depth 3H/4 is 0.36 units.

$\therefore$ eg = 0.36 units

Similarly referring to Figure 15 (a) the ordinate for 1:6 plate with a cut of depth 3H/4 is 0.15 units.

$\therefore$ fh = 0.15 units.

By superimposition, the maximum stress at the top of the projection = eg + fh = 0.51 units.

Hence to reduce the maximum stress at the top of the projection to 51 per cent. of the stress at its base, the depth of a central cut should be about 3H/4.

The example only illustrates the method used. For an actual ship the plate (A) could idealize a given length of the sides of the superstructure and (B) the sides of the ship. If H = 30 ft., L = 180, depth of the ship = 60 ft., depth of a central cut required to reduce stress at the top of the superstructure to 50 per cent. of the stress at the base = $\frac{3 \times 30}{4}$ = 22.5 ft.

Idealised plate projections representing the sides of a superstructure only have been the subject of the above study. To get some idea of the effect of a deck, solutions can be obtained for flanges attached to the unloaded longitudinal edges of the plate. The flange can be considered to be sufficiently compact for the distribution of stress to be uniform across the section[8]. This is not the condition in practice, but the practical case where the stress varies across the width of the superstructure may to some extent be simulated by taking a flange of variable cross-section. A better solution may be obtained without much difficulty by continuing the finite-difference grid into an abutting superstructure deck in which the stress is allowed to vary. This would only amount to solving a larger number of simultaneous equations which can be fairly simply done using the digital computer.

The effect of a deck would be to reduce the growth of longitudinal stress (σx) in a plate projection and the curves in Figure 15 would be lower than their present position. There would be an increase of shear stress especially towards the end of the projection.

"Point-forces"

The introduction of a cut introduces a stress concentration at its root, and also affects the stress concentration at the ends of the projection. The values of all the stresses at the ends of the projection and at the root of cut are indeterminate; but, on a finite difference grid, the total "point-force" spread over one grid-length can be estimated from the equilibrium condition that the total shearing force on a horizontal line must be equal to the longitudinal force on a cross-section which meets the line. The point-forces (P_1 and P_2 in the figure below) give rise to the concentrations of stress.

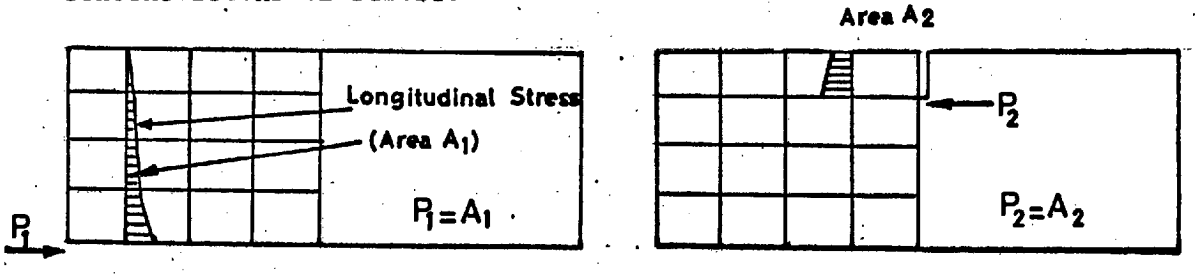

Figure 19 (a) shows the variation of "point-forces" P_1 and P_2 with depth of cut for a 1:4 plate projection subjected to constant strain and zero curvature along the base. As the depth of cut increases, the "point-force" at the end of the projection decreases. The "point-force" at the root of the cut is zero for no cut and increases as the

depth of cut increases, while still remaining smaller in magnitude than that at the end of the projection. If the magnitude of the "point-force" is taken as a rough measure of the stress concentration, it may be noted that in this case the introduction of a cut reduces the stress concentration at the end of the projection and introduces a concentration at the root of the cut, which is smaller than that at the end.

Figure 19 (b) shows the variation of "point-forces" with the depth of cut for a 1:4 plate with uniform curvature and zero strain imposed along the base. The "point-forces"in this case are smaller than those in the case already discussed. As the depth of cut increases, the "point-force" at the end of the projection decreases. The "point-force" at the root of the cut is zero for no cut. It increases as the depth of cut increases - becoming larger than that at the end of the projection - and then decreases. This indicates that the stress concentration in this case has a maximum value for an intermediate depth of cut.

In the case of a plate projection subjected to a combination of uniform strain and uniform curvature, a rough indication of the relative stress concentrations due to different depths of cut can be obtained by adding "point-forces" due to uniform strain and uniform curvature in correct proportions.

The finite difference method could also be used for plate projection with a number of cuts.

Use of Interconnected graded nets

At singular points such as the corners of the loaded edges of a superstructure or the root of a straight cut in a superstructure, the stresses are indeterminate. In such regions it is however possible to reduce the mesh size progressively so that the stress distribution may be determined as close to the discontinuity as may be required although the discontinuity itself is never reached.

An interconnected graded net was used at the corner of an idealised plate projection. Figure 20(b) shows the first stage of the grading used at the corner. The values at points of interconnection (A, B) were parabolically interpolated and expressed in terms of displacements on the coarse net. The validity of parabolic interpolation was supported by comparison with graphical interpolation. There are some points on the grid which have unequal mesh lengths in different directions (E, I, G in Figure 20(b)) Finite difference relations for grids of unequal mesh lengths can be derived by means of Taylor's expansion.

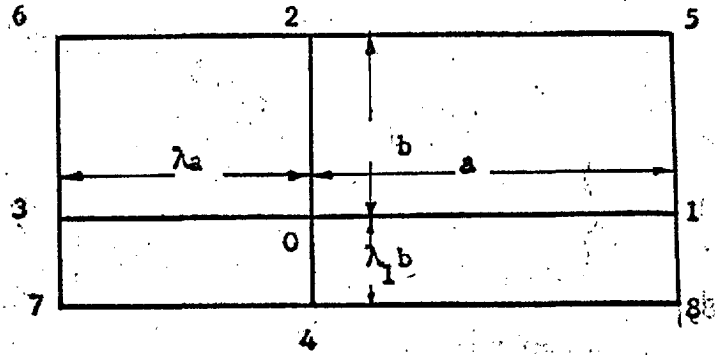

$$u_1 = u_o + a\left(\frac{\delta u}{\delta x}\right)_o + \frac{a^2}{2}\left(\frac{\delta^2 u}{\delta x^2}\right)_o + \frac{a^3}{6}\left(\frac{\delta^3 u}{\delta x^3}\right)_o + \frac{a^4}{24}\left(\frac{\delta^4 u}{\delta x^4}\right) + \quad \ldots\ldots(1.8)$$

$$u_3 = u_o - \lambda a\left(\frac{\delta u}{\delta x}\right)_o + \frac{\lambda^2 a^2}{2}\left(\frac{\delta u}{\delta x^2}\right)_o - \frac{\lambda^3 a^3}{6}\left(\frac{\delta^3 u}{\delta x^3}\right)_o + \frac{\lambda^4 a^4}{24}\left(\frac{\delta^4 u}{\delta x^4}\right) - \quad \ldots\ldots(1.9)$$

Multiplying equation (1.8) by λ^2 and subtracting equation (1.9) gives

$$\left(\frac{\delta u}{\delta x}\right)_o = \frac{\lambda^2 u_1 - u_3 + u_o(1 - \lambda^2)}{a(\lambda^2 + \lambda)} \quad \ldots\ldots(1.10)$$

(after neglecting terms of higher order)

Similarly $$\left(\frac{\delta u}{\delta y}\right)_o = \frac{\lambda_1^2 u_2 - u_4 + u_o(1 - \lambda_1^2)}{a(\lambda_1^2 + \lambda_1)} \quad \ldots\ldots(1.11)$$

Multiplying equation (1.8) by λ and adding to equation (1.9 gives

$$\left(\frac{\delta^2 u}{\delta x^2}\right)_o = \frac{\lambda u_1 + u_3 - u_o (1 + \lambda)}{\frac{a}{2}(\lambda^2 + \lambda)}$$

(after neglecting terms of higher order)

Similarly

$$\left(\frac{\delta^2 u}{\delta y^2}\right)_o = \frac{\lambda_1 u_2 + u_4 - u_o (1 + \lambda_1)}{\frac{b^2}{2}(\lambda_1^2 + \lambda_1)}$$

Let $s_o = \left(\frac{\delta u}{\delta x}\right)_o$

$$s_2 = \left(\frac{\delta u}{\delta x}\right)_2$$

$$s_4 = \left(\frac{\delta u}{\delta x}\right)_4$$

$$\left(\frac{\delta s}{\delta y}\right)_o = \frac{\lambda_1^2 s_2 - s_4 + s_o (1 - \lambda_1^2)}{b (\lambda_1^2 + \lambda_1)} \qquad \text{.....(1.12)}$$

(Using equation (1.11))

Using relation (1.10)gives

$$s_o = \frac{\lambda^2 u_1 - u_3 + u_o (1 - \lambda^2)}{a (\lambda^2 + \lambda)}$$

$$s_2 = \frac{\lambda^2 u_5 - u_6 + u_2 (1 - \lambda^2)}{a (\lambda^2 + \lambda)}$$

$$s_4 = \frac{\lambda^2 u_8 - u_7 + u_4 (1 - \lambda^2)}{a (\lambda^2 + \lambda)}$$

Substituting the values of s_o, s_2, s_4 in (1.12)gives

$$\frac{\partial s}{\partial y} = \frac{\partial^2 u}{\partial x \partial y} =$$

$$\frac{\lambda_1^2\{\lambda^2 u_5 - u_6 + u_2(1-\lambda^2)\} - \{\lambda^2 u_8 - u_7 + u_4(1-\lambda^2)\} + (1-\lambda_1^2)\{\lambda^2 u_1 - u_3 + u_o(1-\lambda^2)\}}{(\lambda^2+\lambda)(\lambda_1^2+\lambda_1)}$$

Similarly other derivatives can be expressed in finite difference forms and substituted in equations (1.3), giving the following generalized displacement equations for a point which has unequal mesh sizes in different directions.

$$\frac{4k^2}{(\lambda^2+\lambda)}\left\{\lambda u_1 + u_3 - (1+\lambda)u_o\right\} + \frac{2(1-\rho)}{(\lambda_1^2+\lambda_1)}\left\{\lambda_1 u_2 + u_4 - (1+\lambda_1)u_o\right\}$$

$$+ \frac{(1+\rho)k}{(\lambda^2+\lambda)(\lambda_1^2+\lambda_1)}\Big[\lambda_1^2\left\{\lambda^2 v_5 - v_6 + (1-\lambda^2)v_2\right\} - \left\{\lambda^2 v_8 - v_7 + v_4(1-\lambda^2)\right\}$$

$$+ (1-\lambda_1^2)\left\{\lambda^2 v_1 - v_3 + v_o(1-\lambda^2)\right\}\Big] = 0$$

$$\frac{4}{(\lambda_1^2+\lambda_1)}\left\{\lambda_1 v_2 + v_4 - (1+\lambda_1)v_o\right\} + \frac{2(1-\rho)k^2}{(\lambda^2+\lambda)}\left\{\lambda v_1 + v_3 - (1+\lambda)v_o\right\}$$

$$+ \frac{(1+\rho)k}{(\lambda^2+\lambda)(\lambda_1^2+\lambda_1)}\Big[\lambda_1^2\left\{\lambda^2 u_5 - u_6 + (1-\lambda^2)u_2\right\} - \left\{\lambda^2 u_8 - u_7 + (1-\lambda^2)u_4\right\}$$

$$+ (1-\lambda_1^2)\left\{\lambda^2 u_1 - u_3 + u_o(1-\lambda^2)\right\}\Big] = 0$$

.....(1.13)

(where $k = \frac{b}{a}$)

If $\lambda = \lambda_1 = 1$ the equations (1.5) for rectangular grid are obtained.

Figure 20 shows the different stages of grading. The number of simultaneous equations was 36 for the coarse net, 44 for the first grading, and 52 for the second grading.

Figure 21 shows the effect of grading of nets on displacements in a plate of side ratio 1:2 with constant strain and zero curvature imposed on the lower boundary. It may be noted that the displacements obtained from the first and second gradings do not differ much along and to the right of the section pt; these displacements may therefore be regarded as known and the plate may be cut along pt for purposes of solution. The plate to be solved then is PT tp. The number of equations reduce by 20. Further grading of the net may be continued as the corner is approached. After further gradings, another part of the plate can be separated and gradings continued.

Figure 22 shows the effect of net-grading on u, v and $\frac{\delta v}{\delta y}$ at the edge of the plate. The v-displacement equation at point S when it is on the coarse net is written in terms of displacements which include those of T where $v = 0$. But when the equation at S is written for the first grading, it involves the non-zero value of v-displacement at J. This accounts for the difference in the v-displacement values obtained at point S from the coarse net and from the first grading. A similar explanation holds for the difference in the v-displacements of point J obtained from the first and second gradings. These differences in the values of v-displacements affect the values of $\frac{\delta v}{\delta y}$ at adjacent points. Thus the value of $\frac{\delta v}{\delta y}$ at the point R obtained from the coarse-net differs from that obtained from the first grading. Similarly the value of $\frac{\delta v}{\delta y}$ obtained at point S from the first grading differs from that obtained from the second grading.

Figures 23,24 and 25 show the effect of net grading on σx, σy and τxy. It may be noted that the stresses to the right of the section pt calculated from the first grading are equal to those calculated from the second grading. This indicates again that the plate may be cut at this section for further grading. The transverse stress σy at R and S (Figure 24) is affected in the same way as $\frac{\delta v}{\delta y}$ at these points.

The increase in stresses σx and σy as the corner is approached, may be noted. All the stresses are indeterminate at the corner. But the magnitude of the "point-forces" acting over a grid length can be estimated by equating the total shearing force on a horizontal line to the longitudinal force on a cross-section that meets the line. The values of point forces calculated for different gradings of net are tabulated below.

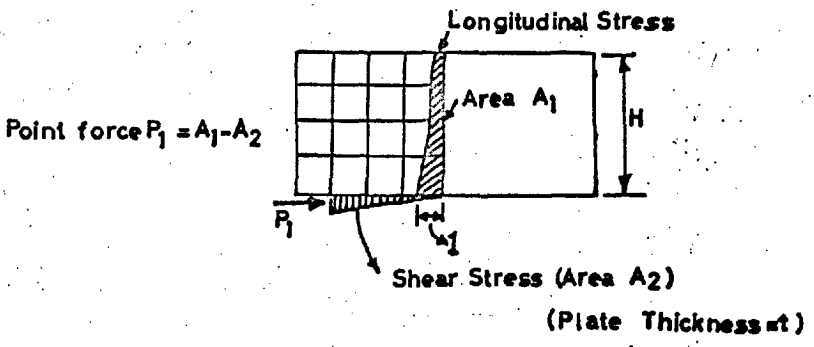

Type of Net	Point-force over grid length of H/4 (in units of applied longitudinal stress)
Coarse Mesh	0.233 Ht
First Grading	0.180 Ht
Second Grading	0.141 Ht

It may be noted that the calculated point-force over a grid length of H/4 is different for the different net gradings. If the magnitude of the point-force is used as an approximate measure of stress concentration forstudying the trends in the variation of stress concentration with a geometrical parameter, it is necessary to keep the net grading the same in each case.

Figure 26 shows a possible method of net grading near the end of a straight cut in a plate.

Stress Function Approach

The method of solution presented so far was in terms of displacements with constant strain or constant curvature imposed at lower boundary of an isolated plate-projection. Stresses due to any imposed circular curvature together with any imposed constant strain can be synthesized by the superposition of these two solutions. The solution was based on the approximating assumption that the superstructure displacements do not affect the longitudinal bending of the main hull (as the plating of the superstructure is thinner than that of the hull); thus ignoring the effect of the distortions of the hull. It is, however, possible to treat the problem as a whole without isolating the superstructure sides. The problem reduces to a thin plate attached to a thick plate subjected to bending and the distortions of the thick plate can be taken into account. A similar type of plate projection occurs between hatch openings in a ship's deck. The figure below shows how the thin plating between hatch openings may be treated as a plate projection from the thick plating outside the hatches.

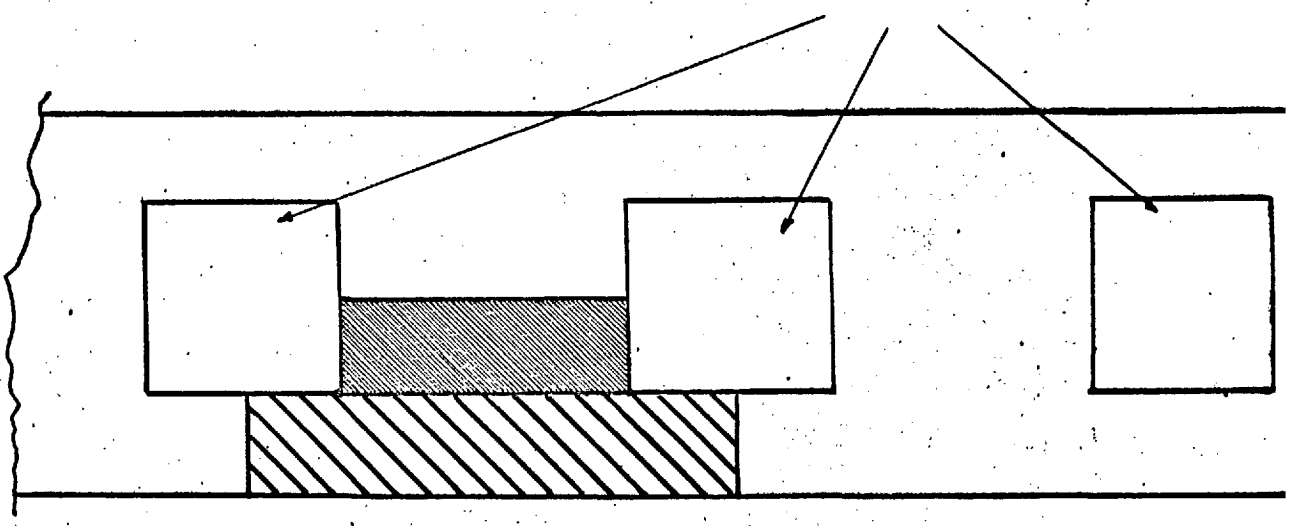
Hatch openings

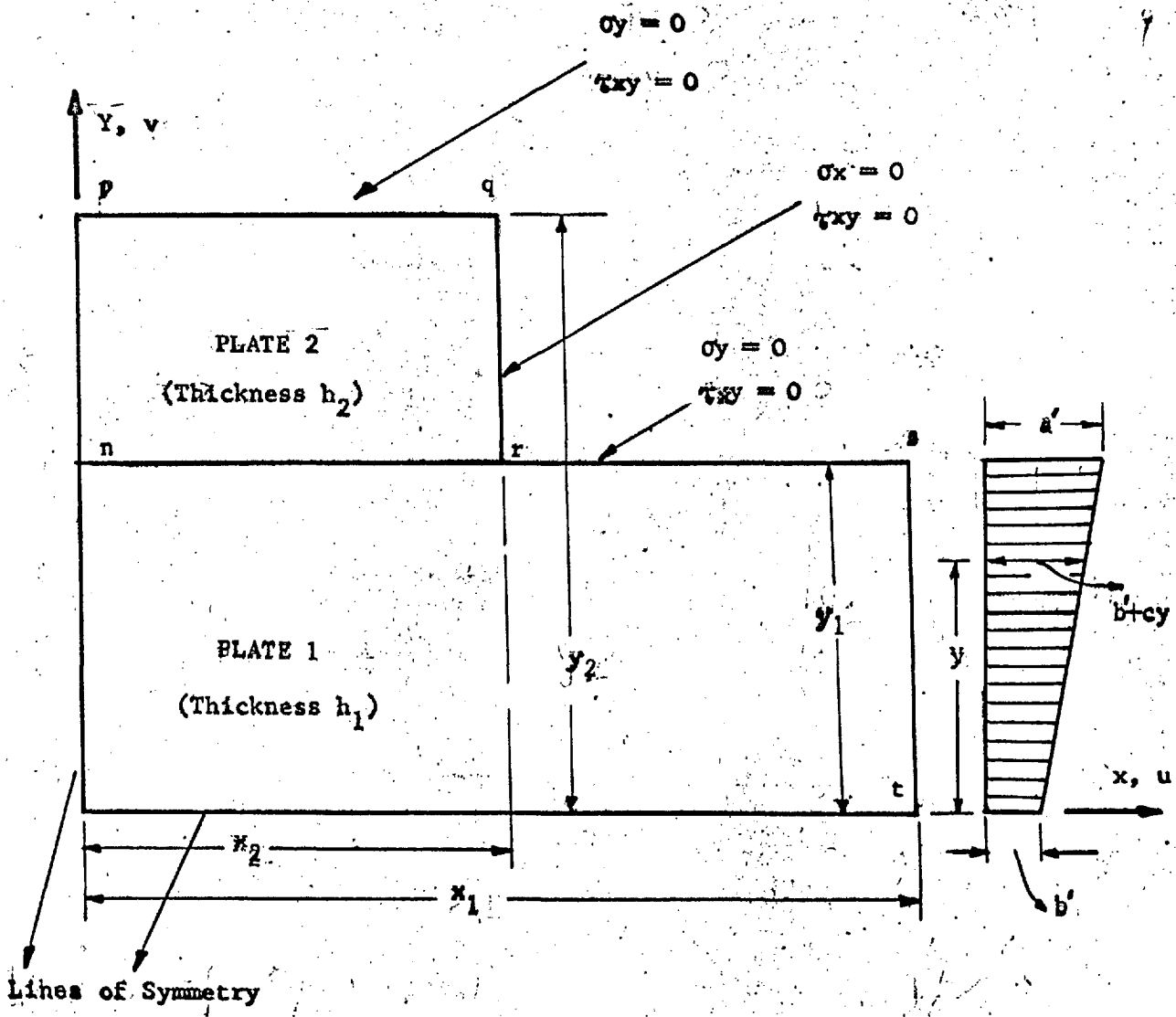
σy = 0
τxy = 0
Y, v
p
q
σx = 0
τxy = 0
PLATE 2
(Thickness h2)
σy = 0
τxy = 0
n
r
s
a'
PLATE 1
(Thickness h1)
y1
y2
y
b'+cy
t
x, u
x2
x1
b'
Lines of Symmetry

The Figure shows a quarter of a plate projection in which plate 2, which has different elastic constants and thickness from plate 1, is attached to it along the boundary nr.

The solution in this case is in terms of two force-functions F. At the junction of the two plates certain conditions of forces and displacements must be satisfied to obtain the correlation between the two force-functions and to arrive at relations necessary for the calculation of fictitious points on the force-function nets at the junction of the two plates.

The forces and displacements at the junction of the two plates are discussed below. Suffices 1 and 2 are used to denote the quantities for the two plates at the same point on the junction

(1) The u displacement is the same in both plates at the junction and hence $\frac{\partial u}{\partial x}$ is the same

$$\left(\frac{\partial u}{\partial x}\right)_1 = \left(\frac{\partial u}{\partial x}\right)_2$$

$$(\varepsilon_x)_1 = \left(\frac{\partial u}{\partial x}\right)_1 = \frac{1}{E_1}\left[\frac{(N_x)_1}{h_1} - \rho_1 \frac{(N_y)_1}{h_1}\right]$$

$$(\varepsilon_x)_2 = \left(\frac{\partial u}{\partial x}\right)_2 = \frac{1}{E_2}\left[\frac{(N_x)_2}{h_2} - \rho_2 \frac{(N_y)_2}{h_2}\right]$$

$$(N_x)_1 = \left(\frac{\partial^2 F}{\partial y^2}\right)_1 ; \quad (N_x)_2 = \left(\frac{\partial^2 F}{\partial y^2}\right)_2$$

$$(N_y)_1 = \left(\frac{\partial^2 F}{\partial x^2}\right)_1 ; \quad (N_y)_2 = \left(\frac{\partial^2 F}{\partial x^2}\right)_2$$

Substituting the values of $(N_x)_1$ $(N_x)_2$ etc. gives

$$\frac{1}{E_1 h_1}\left[\frac{\partial^2 F}{\partial y^2} - \rho_1 \frac{\partial^2 F}{\partial x^2}\right]_1 = \frac{1}{E_2 h_2}\left[\frac{\partial^2 F}{\partial y^2} - \rho_2 \frac{\partial^2 F}{\partial x^2}\right]_2 \qquad \ldots\ldots\ldots(1.14)$$

(2) The v displacement is the same in both plates at the junction and $\frac{\partial v}{\partial x}$ is the same

$$\gamma_{xy} = \frac{\partial u}{\partial y} + \frac{\partial v}{\partial x}$$

$\frac{\partial v}{\partial x}$ is same

or $\gamma_{xy} - \frac{\partial u}{\partial y}$ is same

differentiating with respect to x

$$\frac{\partial}{\partial x}\left(\gamma_{xy} - \frac{\partial u}{\partial y}\right) \text{ is same}$$

or $$\frac{\partial}{\partial x}\left(\gamma_{xy}\right) - \frac{\partial^2 u}{\partial x \partial y} \text{ is same}$$

or $$\frac{\partial}{\partial x}\left(\gamma_{xy}\right) - \frac{\partial}{\partial y}\left(\frac{\partial u}{\partial x}\right) \text{ is same}$$

$$\therefore \frac{\partial}{\partial x}\left\{\frac{(Nxy)_1}{h_1 G_1}\right\} - \frac{\partial}{\partial y}\left[\frac{1}{E_1 h_1}\left\{(Nx)_1 - \rho_1 (Ny)_1\right\}\right]$$

$$= \frac{\partial}{\partial x}\left\{\frac{(Nxy)_2}{h_2 G_2}\right\} - \frac{\partial}{\partial y}\left[\frac{1}{E_2 h_2}\left\{(Nx)_2 - \rho_2 (Ny)_2\right\}\right]$$

$$(Nxy)_1 = \left(\frac{\partial^2 F}{\partial x \partial y}\right)_1 ; \quad (Nxy)_2 = \left(\frac{\partial^2 F}{\partial x \partial y}\right)_2$$

Substituting the values of $(Nxy)_1$, $(Nxy)_2$ ... etc. gives

$$\frac{\partial}{\partial x}\left\{-\frac{1}{h_1 G_1}\frac{\partial^2 F}{\partial x \partial y}\right\}_1 - \frac{\partial}{\partial y}\left[\frac{1}{E_1 h_1}\left\{\frac{\partial^2 F}{\partial y^2} - \rho_1 \frac{\partial^2 F}{\partial x^2}\right\}\right]_1$$
$$= \frac{\partial}{\partial x}\left\{-\frac{1}{h_2 G_2}\frac{\partial^2 F}{\partial x \partial y}\right\}_2 - \frac{\partial}{\partial y}\left[\frac{1}{E_2 h_2}\left\{\frac{\partial^2 F}{\partial y^2} - \rho_2 \frac{\partial^2 F}{\partial x^2}\right\}\right]_2 \quad \text{.....(1.15)}$$

(3) Shear force $(Nxy)_1$ in plate 1 is equal to shear force $(Nxy)_2$ in plate 2 at any point on the junction.

$$\therefore \left(\frac{\partial^2 F}{\partial x \partial y}\right)_1 = \left(\frac{\partial^2 F}{\partial x \partial y}\right)_2$$

Integrating with respect to x

$$\left(\frac{\partial F}{\partial y}\right)_1 - \left(\frac{\partial F}{\partial y}\right)_2 = A$$

(where A is a function of y or a constant)

If the slope of the two force functions in y-direction is made the same at the junction, $A = 0$

$$\left(\frac{\partial F}{\partial y}\right)_1 = \left(\frac{\partial F}{\partial y}\right)_2 \quad \text{.....(1.16)}$$

(4) $(\nabla^4 F)_1 = 0$ ..... (1.17) plate 1

(5) $(\nabla^4 F)_2 = 0$ ..... (1.18) plate 2

(6) Vertical forces $(Ny)_1$, $(Ny)_2$ in the two plates will be equal at any point on the junction

$$(Ny)_1 = (Ny)_2$$
$$\left(\frac{\partial^2 F}{\partial x^2}\right)_1 = \left(\frac{\partial^2 F}{\partial x^2}\right)_2$$

Integrating with respect to x gives

$$\left(\frac{\partial F}{\partial x}\right)_1 - \left(\frac{\partial F}{\partial x}\right)_2 = A \quad \text{(where A is a function of y or a constant)}$$

At $x = 0$, the slope of the two stress functions in the x-direction can be made zero

$$\therefore \left(\frac{\partial F}{\partial x}\right)_1 = 0, \quad \left(\frac{\partial F}{\partial x}\right)_2 = 0$$

$$\therefore A = 0$$

$$\therefore \left(\frac{\partial F}{\partial x}\right)_1 - \left(\frac{\partial F}{\partial x}\right)_2 = 0$$

Integrating with respect to x gives

$$(F)_1 - (F)_2 = B \quad \text{(where B is a function of y or a constant)}$$

If the level of the two force functions is made the same at the junction, $B = 0$

$$\therefore (F)_1 = (F)_2 \qquad \ldots\ldots\ldots(1.19)$$

Finite difference relations at the junction

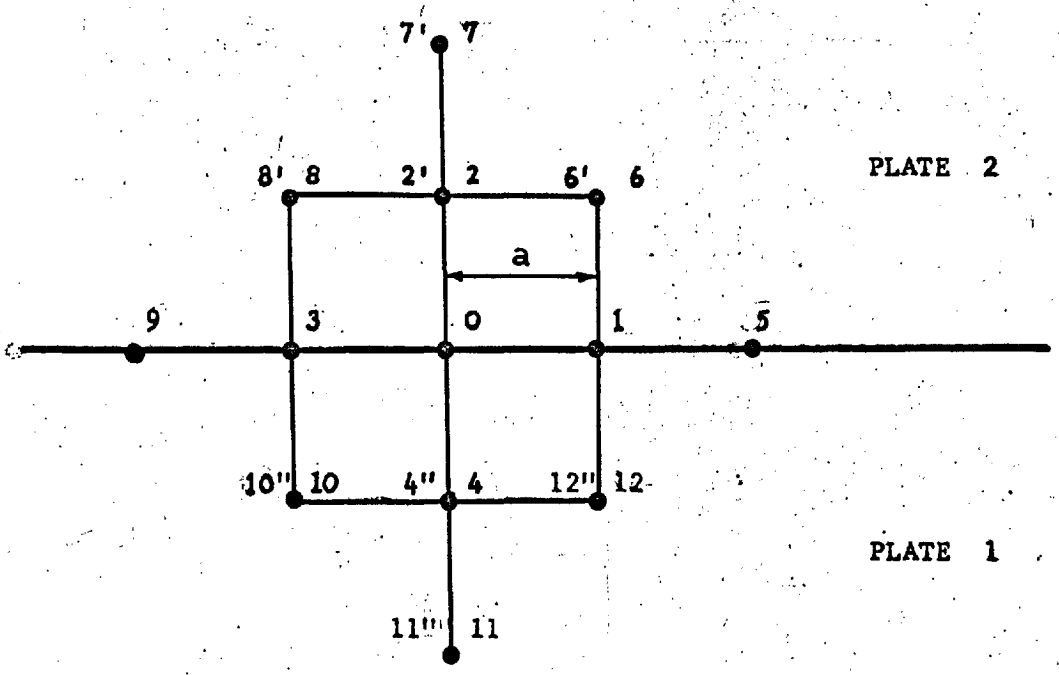

The Figure shows a grid point O at the junction of the two plates. Points 2', 6', 8' and 7' are the fictitious points for plate 1 and points 4", 10", 12" and 11" are the fictitious points for the plate 2.

There are six relations derived for the junction between the plates (Equations 1.14 to 1.19). One of these relations is already utilized by making the force function in the two plates equal at the junction (Equation 1.19). The remaining five relations at each point 0 can then be used for expressing the four fictitious points 7', 2', 4" and 11" in terms of force function at real points; and for solving for the real point 0. The finite difference expressions for these five relations are given below. ($(\frac{\delta F}{\delta y})_1$ means $\frac{\delta F}{\delta y}$ at the point 0 considering it in plate 1).

From equation (1.14)

$$\frac{1}{E_1 h_1}\left(\frac{\delta^2 F}{\delta y^2} - \rho_1 \frac{\delta^2 F}{\delta x^2}\right)_1 = \frac{1}{E_2 h_2}\left(\frac{\delta^2 F}{\delta y^2} - \rho_2 \frac{\delta^2 F}{\delta x^2}\right)_2$$

Also $$\left(\frac{\delta^2 F}{\delta y^2}\right)_1 = \frac{F'_2 + F_4 - 2Fo}{a^2}, \quad \left(\frac{\delta^2 F}{\delta x^2}\right)_1 = \frac{F_1 + F_3 - 2Fo}{a^2}$$

$$\left(\frac{\delta^2 F}{\delta y^2}\right)_2 = \frac{F_2 + F_4'' - 2Fo}{a^2}, \quad \left(\frac{\delta^2 F}{\delta x^2}\right)_2 = \frac{F_1 + F_3 - 2Fo}{a^2}$$

Substituting these relations in the equation above gives

$$\left(\frac{F_2'}{E_1 h_1} - \frac{F_4''}{E_2 h_2}\right) = \frac{1}{E_2 h_2}\left[F_2 + 2(\rho_2 - 1)Fo - \rho_2 (F_1 + F_3)\right] - \frac{1}{E_1 h_1}\left[F_4 + 2(\rho_1 - 1)Fo - \rho_1 (F_1 + F_3)\right] \quad \ldots\ldots\ldots (1.20)$$

Now $$\left(\frac{\delta^3 F}{\delta^2 x \delta y}\right)_1 = \frac{1}{2a^3}\left(F_6' + F_8' - 2F_2' - F_{12} - F_{10} + 2F_4\right)$$

$$\left(\frac{\delta^3 F}{\delta^2 x \delta y}\right)_2 = \frac{1}{2a^3}\left(F_6 + F_8 - 2F_2 - F_{12}'' - F_{10}'' + 2F_4''\right)$$

$$\left(\frac{\partial^3 F}{\partial y^3}\right)_1 = \frac{1}{2a^3}\left(F_7' - 2F_2' + 2F_4 - F_{11}\right)$$

$$\left(\frac{\partial^3 F}{\partial y^3}\right)_2 = \frac{1}{2a^3}\left(F_7 - 2F_2 + 2F_4'' - F_{11}''\right)$$

Substituting these relations in equation (1.15) gives

$$\left(-\frac{1}{h_1 G_1} + \frac{\rho_1}{E_1 h_1}\right)\left(F_6' + F_8' - 2F_2'\right) + \left(-\frac{1}{h_2 G_2} + \frac{\rho_2}{E_2 h_2}\right)\left(F_{12}'' + F_{10}'' - 2F_4''\right) - \frac{1}{E_1 h_1}\left(F_7' - 2F_2'\right) + \frac{\rho_1}{E_2 h_2}\left(2F_4'' - F_{11}''\right)$$

$$= \left(-\frac{1}{h_2 G_2} + \frac{\rho_2}{E_2 h_2}\right)\left(F_6 + F_8 - 2F_2\right) + \left(-\frac{1}{h_1 G_1} + \frac{\rho_1}{E_1 h_1}\right)\left(F_{12} + F_{10} - 2F_4\right) - \frac{1}{E_2 h_2}\left(F_7 - 2F_2\right) + \frac{1}{E_1 h_1}\left(2F_4 - F_{11}\right) \qquad \ldots\ldots(1.21)$$

From Equation (1.16) we have

$$\left(\frac{\partial F}{\partial y}\right)_1 = \left(\frac{\partial F}{\partial y}\right)_2$$

$$\left(\frac{\partial F}{\partial y}\right)_1 = \frac{F_2' - F_4}{2a}; \qquad \left(\frac{\partial F}{\partial y}\right)_2 = \frac{F_2 - F_4''}{2a}$$

Substituting these relations

$$F_2' + F_4'' = F_2 + F_4 \qquad \ldots\ldots\ldots(1.22)$$

Expressing the biharmonic relations (1.17) and (1.18) in finite difference form the following relations may be obtained.

$$20\,F_o - 8\,(F_1 + F_2' + F_3 + F_4) + 2\,(F_6' + F_8' + F_{10} + F_{12}) + F_5 + F_7' + F_9 + F_{11} = 0 \quad \ldots\ldots\ldots(1.23)$$

$$20\,F_o - 8\,(F_1 + F_2 + F_3 + F_4'') + 2\,(F_6 + F_8 + F_{10}'' + F_{12}'') + F_5 + F_7 + F_9 + F_{11}'' = 0 \quad \ldots\ldots\ldots(1.24)$$

Boundary Conditions

To determine the value of the force functions at the boundaries, point p is considered first. The value of $\frac{\delta F}{\delta x}$ is equated to zero at this point, since the surface representing the force function must by symmetrical about the y-axis.

Boundary pq

$\sigma y = 0 \quad \tau xy = 0 \quad \therefore \quad \frac{\delta^2 F}{\delta x^2} = 0, \quad \frac{\delta^2 F}{\delta x \delta y} = 0$

$\frac{\delta^2 F}{\delta x \delta y} = 0$

Integrating with respect to x gives

$\frac{\delta F}{\delta y} = \eta$ (where η is a function of y or a constant since y is constant along pq, η is a constant)

$\frac{\delta^2 F}{\delta x^2} = 0$

Integrating $\frac{\delta F}{\delta x} = C$ (where C is a function of y or a constant)

But $\frac{\delta F}{\delta x} = 0$ at $x = 0$

$\therefore C = 0$

$\frac{\delta F}{\delta x} = 0$

Integrating

$F = \lambda'$ (where λ' is a constant or a funtion of y but as y is constant λ' is constant)

Hence, along pq

$F = \lambda'$

$\frac{\delta F}{\delta y} = \eta$

$\frac{\delta F}{\delta x} = 0$

It may be pointed out here that it will be possible to obtain the values of λ and η in terms of the dimensions of plates after going round the boundaries of the plates

Boundary qr

$\tau xy = 0$

$\therefore \frac{\delta^2 F}{\delta x \delta y} = 0$

Integrating with respect to y

$\frac{\delta F}{\delta x} = D$ (where D is a function of x or a constant)

At $y = y_2$ $\frac{\delta F}{\delta x} = 0$ $\therefore D = 0$

$\therefore \frac{\delta F}{\delta x} = 0$

$\sigma x = 0$ $\therefore \frac{\delta^2 F}{\delta y^2} = 0$

Integrating with respect to y gives

$\frac{\delta F}{\delta y} = E$ (where E is a function of x or a constant)

At $y = y_2$ $\frac{\delta F}{\delta y} = \eta$

$\therefore E = \eta$

$\therefore \frac{\delta F}{\delta y} = \eta$

Integrating $F = \eta y + G$

But $F = \lambda'$ at $y = y_2$

$\therefore G = \lambda' - \eta y_2$

$F = \eta y + (\lambda' - \eta y_2)$

Hence, along qr

$$F = \eta y + (\lambda' - \eta y_2)$$

$$\frac{\delta F}{\delta y} = \eta$$

$$\frac{\delta F}{\delta x} = 0$$

Boundary rs

$\tau xy = 0$

$$\therefore \frac{\delta^2 F}{\delta x \delta y} = 0$$

Integrating $\frac{\delta F}{\delta y} = H$ (where H is a function of y or a constant) But $\frac{\delta F}{\delta y} = \eta$ at $x = x_2$

$$\therefore H = \eta$$

$$\therefore \frac{\delta F}{\delta y} = \eta$$

$\sigma y = 0$

$$\therefore \frac{\delta^2 F}{\delta x^2} = 0$$

Integrating $\frac{\delta F}{\delta x} = J$ (where J is a function of y or a constant)

But $\frac{\delta F}{\delta x} = 0$ at $x = x_2$ $\therefore J = 0$ $\therefore \frac{\delta F}{\delta x} = 0$

Integrating $F = K$ (where K is a constant)

But $F = \eta y_1 + (\lambda' - \eta y_2)$ at $x = x_2$ $y = y_1$

$$\therefore K = \eta y_1 + (\lambda' - \eta y_2)$$

$$\therefore F = \eta y_1 + (\lambda' - \eta y_2)$$

Hence, along rs

$$F = \eta y_1 + (\lambda' - \eta y_2)$$

$$\frac{\delta F}{\delta y} = \eta$$

$$\frac{\delta F}{\delta x} = 0$$

Boundary st

$\tau_{xy} = 0 \qquad \therefore \frac{\delta^2 F}{\delta x \delta y} = 0$

Integrating $\frac{\delta F}{\delta x} = L$ (where L is a constant)

But $\frac{\delta F}{\delta x} = 0$ at s

$\therefore L = 0$

$\therefore \frac{\delta F}{\delta x} = 0$

$\frac{\delta^2 F}{\delta y^2} = b' + cy$ (a trapezoidal stress distribution is taken at the edge st so that a uniform or bending stress may be applied)

$\frac{\delta F}{\delta y} = b'y + \frac{cy^2}{2} + M$

$F = \frac{b'y^2}{2} + \frac{cy^3}{6} + My + N$

But $\frac{\delta F}{\delta y} = \eta$ at $y = y_1$

and $F = \eta y_1 + \lambda' - \eta$

$\therefore M = \eta - b'y_1 - \frac{cy_1^2}{2}$

$N = \lambda' - \eta y_2 + \frac{b'y_1^2}{2} + \frac{cy_1^3}{3}$

$F = \frac{b'y^2}{2} + \frac{cy^3}{6} + (\eta - b'y_1 - \frac{cy_1^2}{2})\ y + \lambda' - \eta y_2 + \frac{b'y_1^2}{2} + \frac{cy_1^3}{3}$

Let $F = \lambda_1'$ and $\frac{\delta F}{\delta y} = \eta_1$ at $y = 0$.

This gives

$\lambda_1' = \lambda' - \eta y_2 + \frac{b'y_1^2}{2} + \frac{cy_1^3}{3}$

$\eta_1 = \eta - b'y_1 - \frac{cy_1^2}{2}$

If λ_1' and η_1 are equated to zero it follows that

$$\eta = b'y_1 + \frac{cy_1^2}{2}$$

$$\lambda' = \left(b'y_1 + \frac{cy_1^2}{2} \right) y_2 - \frac{b'y_1^2}{2} - \frac{cy_1^3}{3}$$

Thus λ' and η are known in terms of the size of the plates and the loading applied, and the force function all along the boundary is known.

The plates can now be sub-divided into a finite-difference grid. The biharmonic equation $\nabla^4 F = 0$ expressed in finite difference form can be written for all points on the grid. The slopes of the force function at the boundaries may be used for expressing the fictitious points outside the boundary in terms of the real points inside the plates. A computer program can be written for solving the finite difference equations.

It is found that if there is a cut in the plate 2 representing an expansion joint, it is not difficult to decide the force function round the cut. The figure below shows the co-ordinates of the cut in the plate 2, and the values of the force function round the cut are also given below.

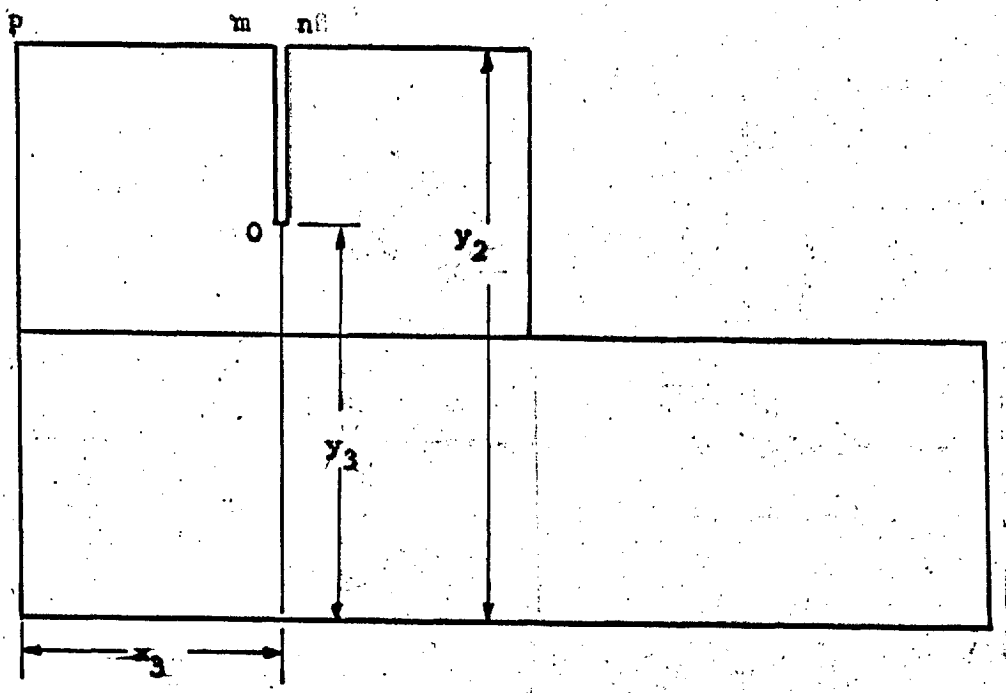

along mo

$$F = \eta y_3 + (\lambda' - \eta y_2)$$

$$\frac{\delta F}{\delta y} = \eta$$

$$\frac{\delta F}{\delta x} = 0$$

along on

$$F = \eta y + (\lambda' - \eta y_2)$$

$$\frac{\delta F}{\delta y} = \eta$$

$$\frac{\delta F}{\delta x} = 0$$

SECTION II

HATCH OPENINGS

The structural discontinuity introduced at the corners of hatch openings gives rise to stress concentration and cracking is sometimes initiated at these points. This section deals with the study of the effect of certain geometrical parameters (such as radius or length of an opening) on the geometrical stress concentration factor as well as on the fatigue strength reduction factor. Whereas the geometrical stress concentration factor depends wholly on the geometry of the opening and is valid for stresses below the elastic limit, the reduction in fatigue strength depends upon a variety of factors such as the size of the specimen and the cycles to failure. Small-size machined specimens of ship steel with rectangular openings were tested under repeated loading in the high cycle as well as the low cycle range. The fatigue strength reduction factor was correlated to the elastic stress concentration factor taking into account the geometrical size-effect. Using the existing theories the probable fatigue behaviour of a large plate with a square opening (of dimensions comparable to those of hatch openings) has been studied. The effect of a mean stress is also included.

EXPERIMENTS

Experiments to find Geometrical Stress Concentration Factors

Photoelasticity was used to find the geometrical stress concentration factors for the proportions of hatch openings for which plate specimens of ship steel were tested under repeated loading. A steel plate specimen was also tested.

Photoelastic Experiments

The specimens consisted of quarter inch thick cast sheets of Araldite Resin CT 200 clamped between steel end plates to which tension was applied. The openings were made by using high speed diamond cutters which copied the pattern from a template on a pantograph machine, the plate being submerged in cooling water during the operation. After machining, the radii at the corners of the opening were checked by projection to a 50:1 magnification. The projected radii were indistinguishable from the correct configuration. By exercising care in the machining process it was possible to use each specimen for successive modifications of the shape of the opening.

The loads were applied hydraulically and measured by strain gauges on a calibrated aluminium alloy link. The loading frame was contained within an outer frame relative to which it could be moved vertically or horizontally so that any part of the model could be placed within the field of the polariscope. (Figure 27).

Fringe patterns were projected on a screen and the emergence of successive fringes was noted as the load was applied. The point of maximum stress concentration occurs at the free boundary where the normal stress is zero, so that the observation of fringe order is sufficient to determine the stress concentration. Fringe orders were also determined at some points on the straight boundaries of the opening and the longitudinal edges of the plate.

The effect of the length and width of the opening on stress concentration was studied for a corner radius of 1/24 of the width of the opening. This is the smallest ratio recommended by Lloyds Register. The effect of varying the radius was studied for a square opening.

Table 2. and Figures 28 to 30 show the variation of the stress concentration factor $K_{t\,max}$ for different proportions of opening. The stress concentration decreases with increasing length or width of opening. Direct comparison with the results obtained by other investigators is difficult because the hole shapes are not identical. In general, however, the values obtained are somewhat lower than those interpolated from results reported elsewhere [15][16], and surprisingly low compared to the infinite plate solution.

The low values of stress concentration factors for very small radii may be due to the effect of the thickness of the plate in relation to the corner radius. To study this effect, further photoelastic tests were conducted on small circular holes in a 12 in. wide 1/4 in. thick Araldite plate. The smallest hole was 3/32 in. in diameter giving a thickness to radius ratio of 5:4. The diameter of the hole was increased in stages and stress concentration factors determined.

Figure 31 shows the effect of varying thickness to radius ratio on the stress concentration and the theoretical curve due to Howland [37] is also shown. At very small values of the radius, (giving a large thickness to radius ratio) the departure from the theoretical curve is considerable. As the thickness to radius ratio decreases, the experimental points get closer to the theoretical curve. The lower curve shows the relation between the thickness/radius ratio and the radius/width ratio for the plate tested.

The observed departures from the accepted values of stress concentration factors are clearly very significant, and cast doubt on the validity of the photoelastic experiments. Further investigations were carried out at Imperial College [40] to explain the discrepancies observed. Although these investigations [40] did not explain the low values of stress concentration factors obtained by photoelasticity, they indicated that tests on a steel specimen having a thickness/radius ratio not greater than about ten would give reliable values. Tests were therefore conducted on a steel specimen in which the greatest thickness/radius ratio was equal to one.

Experiments on a Steel Specimen

The specimen consisted of a steel plate 2 ft. 9 in. x 8 ft. overall x $\frac{1}{4}$ in. thick clamped at its ends between pairs of plates 2 ft. 9 in. x 2 ft. x $\frac{5}{8}$ in. thick by high tensile bolts. It contained a 1 ft. 4 $\frac{1}{2}$ in. square opening with radiused corners (Figure 32). The corner radii at the opposite ends of the opening were different to obtain stress concentration factors for two radii from a single test. Electrical resistance strain gauges of $\frac{1}{8}$ in. gauge length were fixed along the radiused edges of the opening and at points at the centre of the sides. The position of maximum stress concentration for square openings in infinite plates [36] was used in deciding the distribution of strain gauges around the corner. In some cases, the backing

of the strain gauges was cut to reduce their overall size. This enabled two rows of gauges to be fixed on the thickness of the plate at close intervals. It was checked that the gauge-factor was unaffected due to the cutting of the backing of the gauges.

The specimen was loaded in tension, the load being applied hydraulically and measured by a load cell. Figure 33 shows the testing arrangement. The test was conducted in two stages. The radii at the two opposite ends of the opening were made to give radius/width ratios of 1/6 and 1/24 in the first stage; and in the second stage they were machined down to give ratios of 1/12 and 1/66 respectively. The proportions corresponded to those of the steel specimens tested under repeated loading. The load on the specimen was increased in steps and a linear load-strain diagram was obtained for every strain gauge. The maximum load was limited to give a maximum recorded local strain of about 900 microstrain. Strains were recorded by an automatic strain recorder and the accuracy of measurement was about $\pm$ 5 microstrain. The gauge factor should not vary more than $\pm$ 1.5 per cent. from the nominal value.

Results and Discussion

Table 3 shows the configurations tested and the corresponding stress concentration factors Kt (max.). Figure 34 shows the variation of stress concentration factor with radius/width ratio, the photoelastic results also being plotted on the same diagram. The low values obtained by photoelasticity especially at small radii may be noted. Figure 34 also shows the values from the infinite plate solution.(36) As an approximation, these values may be modified for a finite plate by multiplying them by a reduction factor, the value of this factor being decided on the basis of existing theoretical results for a circular opening in a finite plate. (37) The reduction factor in the case of the openings tested was taken as 2.16/3, where 2.16 is the stress concentration factor for a finite plate with a 50 per cent. circular opening, and 3 is the stress concentration factor for a circular opening in an infinite plate. It may be noted that the modified values plotted in Figure 34 have a maximum deviation of about 13 per cent. from the steel plate results.

Figure 35 shows the variation of stress concentration along the corner radii. The position of maximum stress concentration for the infinite plate is shown for comparison.(36) Due to the extrapolation of very high strain gradients into the thickness of the strain gauges at points of stress concentration, the

strains recorded may be slightly high. A second error, in the opposite direction, arises due to the strain gauge recording the average strain over the gauge length. Both errors increase as the radius decreases. For a radius of $\frac{1}{4}$ in. (r/b = 1/66) the observed value of Kt (max.) may be about 6 per cent. low, the error due to gradient being calculated on the basis of a circular hole of this radius in an infinite plate, and that due to gauge length being calculated on the basis of the tangential stress distribution shown in Figure 35 . For each of the remaining three radii the net error calculated on the above basis is less than 1 per cent.

Figure 36 shows the stress distribution across the middle of the plate in way of the opening. The total force inferred from the strain readings across the centre of the plate agreed with the applied load within less than 1 per cent. Stress distributions obtained experimentally are compared with results obtained by finite difference displacement solutions in the theoretical part of this section.

Fatigue Tests

The results of the tests described so far, on specimens loaded statically, merely gave the value of the geometrical or elastic stress concentration factors. In order to find the reduction in fatigue strength, plate specimens with rectangular openings of different proportions were tested under alternating loads. The specimens were of ship steel and were tested in the low cycle as well as the high cycle range.

Some amount of exploratory experimental work was done before embarking on the actual test programme.

Operating Frequency for high-cycle Tests

The higher the frequency and the stress amplitude, the greater is the heating of the specimen. For temperatures between 0-100°C the fatigue strength of steel is unaffected [41]. In order to decide the operating frequency for the high cycle testing, tests were conducted on a specimen of plain steel at different stress levels and frequencies. Figure 37 shows the effect of stress level on temperature at two frequencies. It may be noted that the effect of frequency on temperature is bigger at higher stress levels. Figure 38 shows the effect of frequency on temperature at a given high stress level. From the graph it can be seen that the frequencies below 140 cps will keep the temperature below about 100°C. Hence it was decided to keep the frequency below 140 cps especially at high stress levels. The temperature in these tests was measured by a thermocouple attached to the specimen and an automatic temperature recorder.

Effect of Surface Finish

Surface roughness as a result of machining reduces the fatigue strength in comparison with polished specimens. Internal stresses are always caused at the surface by machining as a result of plastic deformation of the grain on the outermost layer and to some extent as a result of high local overheating. The direction of machining in relation to the direction of dynamic stress also affects the fatigue life. It is difficult to separate the effect of roughness from these other factors and therefore the reduction in fatigue strength should be referred to different methods of machining instead of to roughness alone.

The specimens to be tested under repeated loading were to have rectangular openings with radiused corners. It is extremely difficult to obtain a smooth transition between the radiused part and the straight part by ordinary machining methods without producing undercuts (at the point of transition), due to the deflection of the tool. This introduces additional stress concentrations. The spark erosion method was therefore used to obtain the final shape of the openings. A uniform surface finish inside the opening was also obtained by this method. Therefore the surface finish investigations were done on specimens finished by this method. Details of the method will be given on Page 73 .

Figure 39 shows the effect of surface finish at test section of plain specimens of annealed steel on their fatigue life [38]. The effect of surface finish at geometrical discontinuities (e.g. that of finish inside a hole in a specimen) on fatigue life has not been fully investigated. A few tests were conducted to study this effect and to decide the surface finish to be adopted for the inside of the openings. Identical specimens with circular holes of different surface finish inside were tested under alternating loads. Figure 40 shows the effect of surface finish on the fatigue life of specimens which had the same geometrical stress concentration. It may be noted that in this case the effect is more pronounced than in plain specimens. The results shown in Figure 40 are for specimens spark-eroded by a machine which was not to be used for the specimens required for the actual fatigue tests. The time of spark-eroding a hole on a given machine increases with the fineness of the finish required, and is different for different machines. The new machine which was to be used subsequently was used for spark-eroding specimens for more tests on surface finish. The specimens tested had 3/4" square openings with 1/16" radius at the corners. This particular shape was chosen because the actual specimens were also to have similar openings. The table below shows the time of spark-erosion versus the surface finish obtained.

Speed No. on Eroding Machine	Surface Finish	Time of Erosion
2	40- 50 Microinches	16-21 hours
4	100- 150 "	$1\frac{1}{2}$ hours
5	about160 "	1 hour
6	about235 "	1 hour

It may be observed from the table that the time of erosion increases drastically for a very fine finish. It was decided to use a speed of 4 which gave a reasonable finish in a short time. Tests on two specimens spark-eroded at a speed of 4 indicated that the same speed gave the same surface finish and the same fatigue life.

The surface finish mentioned above is defined as the average undulation of the surface from the mean surface. The measurements were taken on a Talysurf surface finish instrument. The range of magnification in this instrument in the vertical direction is from 1000 to 50,000 and in the horizontal direction from 20 to 100. Figure 41 shows a typical surface finish record. A gauge length of 3" on this record (corresponding to .03" on the actual surface) is chosen and a mean line is decided such that the area under the curve, above this line, is equal to the area under the curve below it. This was obtained after a few trials using

the planimeter. The surface finish for a 3" gauge length is given by the following formula

$$\text{Surface finish } \mu \text{ in microinches} = \frac{2\ (\text{Area above mean line in sq.in.})}{3} \times \frac{10^6}{M}$$

where M is the vertical magnification.

Shape of specimen for finding the fatigue properties of the material

In order to find the fatigue properties of the material, the aim should be to make the shape of the specimen such that there are no geometrical stress concentrations and such that the material at the test section is not restrained by the adjacent material. A specimen with a parallel test length followed by a gradual transition to the gripped part satisfies both these requirements. But certain practical difficulties are encountered with a specimen of this shape. Firstly, using ordinary machining methods it is very difficult to avoid undercuts at the points of transition. These undercuts give rise to stress concentrations and initiate premature failure. Secondly it is difficult to keep such a specimen stiff enough not to buckle under the very high stresses applied in the low-cycle range.

Several trial specimens of different shapes were tested to arrive at the best possible shape which could be tested in the low-cycle as well as the high cycle range with the available testing equipment. Figure 42 shows the dimensions of the various trial specimens. Trial Specimen 1 broke at the point of transition where there was an undercut of about .002" showing signs of buckling when tested at a high stress level. Specimen 2 was provided with a more gradual transition and was ground to avoid undercuts. Measurements taken by a sensitive device showed the absence of any undercuts. The specimen when tested at a high stress level buckled as a fixed ended column in the low-cycle test rig. Small cylindrical specimens with threaded ends were designed and made out of the thickness of the material (which was available in the form of 3/8" plates). Specimen 3 broke at the thread due to stress concentration. Specimen 4 broke at the point of transition due perhaps to an undercut. Specimen 5 was made with no straight part in the test length but a very slight neck in the middle which introduced a very small value of known stress concentration but eliminated the possibility of breaking of the specimen at the point of transition due to unknown concentrations. This specimen did break in the

middle when tested at a low stress level in the high cycle range. A similar specimen (No. 6) was then tested at a high stress level in the low cycle range. This specimen buckled due to the top part swaying relative to the bottom. As the plate specimen (Trial 2) failed in a more favourable mode than the cylindrical one (Trial 6), specimen 7 was designed as a plate specimen. This specimen had no straight part and had about 5 per cent geometrical stress concentration present at the mid-section. This specimen was tested at a high stress and was found not to buckle and the fracture took place at the mid-section. This was the shape adopted for finding the fatigue behaviour of the material.

Design and Fabrication of Hatch Specimens

Figure 43 shows the intended programme of tests. The sketches show specimens with one and with two openings, but the test series for the second case was not carried out for this thesis. The proportions of the openings were chosen to lie within the limits of the proportions of hatch openings in ships, and also corresponded to those adopted for the photoelastic tests. The specimens were designed against buckling and their size was close to the largest that could be tested with the available testing equipment.

The steel used was ship steel grade A and was available in the form of black hot rolled plates 20' x 3" x 3/8". The yield stress of the material was 19 tons/sq.in. The fabrication of the specimens was done with extreme care to reduce the scatter inherent in all fatigue testing. The various stages of machining are indicated below.

(1) Bandsawing and shaping roughly to size.

(2) Rough machining two faces by vertical fly-cutting

(3) Bandsawing the curved sides and accurate machining ends and edges by vertical milling.

(4) Rough machining the hole leaving .020" for spark erosion.

(5) Spark-eroding the hole in two stages.

(6) Grinding the faces to fine finish.

Care was taken to avoid any scratches on the finished specimen.

Spark-Erosion Technique

Figure 44 shows part of a spark-eroding machine. The process consists of passing an electrode through the hole and striking an arc between the electrode and the specimen. The spark loosens particles of metal from the specimen, giving a hole of correct shape and uniform finish. The specimen is immersed in a tank of paraffin. The electrode vibrates at a high frequency (300 cps) to disperse the debris and sometimes withdraws a small amount to allow the agitated paraffin to clear the debris. The spark gap (hence the size of the electrode) depends upon the surface finish required. By ordinary machining methods it is fairly easy to make an accurate electrode with an outside radius at the corners. The electrodes may be of brass or Elkonite (an alloy of copper specially compounded for spark-erosion). The wear of an Elkonite electrode is very much smaller than that of brass.

Figure 44 shows the electrodes that were used. The electrode passes through the hole in two stages. In the first stage the electrode passes at a higher speed giving a rough finish, whilst the second (slower) pass gives the final shape and finish. The first stage of the electrode was .012" smaller than the size of the hole required and speed 6 was used for this stage. The second stage was .004" smaller and the speed setting was 4. The same electrode could be used for a batch of 8 or 10 similar specimens. A rotating electrode was used for obtaining the circular edges of the specimens required for finding the material fatigue behaviour.

Testing

The usual procedure for determining fatigue behaviour is to test a number of similar specimens subjecting each to a particular range of alternating load until it breaks, so that a relation between the alternating stress S and the number of cycles to failure N (known as the S-N curve) is obtained. The purpose of the present series of tests was to obtain complete S-N curves starting at the semi-range of stress equal to the ultimate strength of the material and extending it to low values of stress at which the life is measured in

millions of cycles. Low-cycle fatigue is generally considered to cover the range of life from 1/4 cycle to 100,000 cycles, and high-cycle fatigue covers life above 100,000 cycles.

Batches of specimens with openings of different proportions were tested.

High Cycle Tests

Specimens in the high cycle range were tested in a Vibrophore high frequency fatigue testing machine.(Figure 45) The machine operates electromagnetically at the resonant frequency of the vibrating parts. The range of test frequency is from 60 to 300 cycles/sec. The load is measured by a dynamometer using an optical system, the load range being controlled automatically by a photoelectric device. The machine is capable of applying alternating or fluctuating loads.

Specimens were tested under alternating stresses at different levels at a frequency of about 130 cps. The machine switches off automatically when the crack is initiated. The test was then continued to fracture by controlling the machine manually.

Low Cycle Tests

The low cycle fatigue tests could not be conducted on the Vibrophore due to heating of the specimen. A hydraulic rig was therefore designed for these tests.

The specimen was pretensioned by four lapped rams acting through serrated and hardened grips which were clamped by high tensile bolts (Figure 46). The rams were connected to a hydraulic loading cabinet C (Figure 47) and a nitrogen accumulator A. The rig was put in the compression-test part of the universal testing machine R. A pulsating compressive load with an amplitude equal to the desired alternating amplitude is applied by the testing machine to the test rig. The test rig applies a pretension to the specimen equal in magnitude to half the desired alternating amplitude. The superimposition of these two loadings give a resultant alternating load to the specimen as shown in Figure 48 .

The function of the nitrogen accumulator connected to the rams is to keep the pretension constant. It consists of a cylinder with a piston floating between oil and nitrogen gas at equal pressure. Due to the elongation or compression of the specimen, the change in volume of the gas due to oil being pumped into or out of the accumulator does not

change its pressure significantly and keeps the oil pressure constant. Figure 49 also shows the low cycle test assembly.

Lapped rams were used because the amount of friction is very small and constant, whereas packed rams suffer from the disadvantage that the packing deteriorates and the friction varies at different pressures. The calibration of the rams used, showed remarkably small amount of friction (0.3 per cent). The cylinders were designed to increase in diameter by not more than .0001 in. under pressure. Figure 50 shows the working drawing of a ram. The ram and the cylinder were lapped to give a radial clearance of .0001". The amount of leakage during normal working amplitudes was very small, and the quantity of oil lost due to this reason was compensated by the load-maintaining device of the loading cabinet.

Material Defects

Some of the specimens were found to have laminations and inclusions. These defects in some cases were undetected until the final stages of the preparation of the specimens. Figures 51 and 52 show some of these specimens. The life of such specimens was affected by the flaws thus introducing scatter in the results.

Fractures

High Cycle Fatigue

The fractured surfaces of specimens broken under high cycle fatigue were characteristic of fatigue fractures. In the region of the origin of crack the surface shows small dark markings. There is a second zone where the crack spreads more rapidly showing a less smooth appearance.

Low Cycle Fatigue

Figure 53 shows a fractured surface of a specimen tested in the low cycle range. Cracks started at the transition point between the corner radius and the straight sides of the openings. The presence of small dark markings in the area of origin of the cracks may be noted. The crack then spreads into a somewhat rough surface perpendicular to the direction of the load towards the middle of the plate thickness and inclined to this direction towards the ends. The dark zone shows that part of the specimen where fracture occurred when the section reduced so much that the metal could not withstand the last application of the load.

In a number of cases, cracking was initiated at 3 or 4 corners. This indicates that the specimens were accurately made and concentrically loaded.

Results and Discussion

Figure 54 shows the S-N curves for specimens with square openings with varying corner-radii together with S-N curve for the material. The fatigue strength reduction factor is generally defined for a given number of cycles to failure as

$$K_f = \frac{\text{(Alternating stress in plain specimen)}}{\text{(Nominal alternating stress in specimen with stress concentration)}}$$

For example, in Figure 54 for square openings with corner radius of 1/8 in. the value of K_f is given for 10^6 cycles by $\frac{S_1}{S_2}$. It may be noted that along the S-N curve the value of K_f depends upon the number of cycles to failure and has two limiting values. One value (usually denoted by K_s) occurs when $N = \frac{1}{4}$, that is when the specimens are broken in a single pull. The second limiting value (usually denoted by K_A) occurs at the other end of the S-N curves where the curves become horizontal (Fatigue Limit). For materials which do not possess a fatigue limit, no great error arises if representative values are obtained at 10^7 cycles.

Figure 55 shows the variation of observed values of strength reduction factor K_f with corner radius for different lives. One batch of specimens was made with openings having sharp corners, but measurements of the corner radii with a magnifier, using a magnification of 100 showed that the nominally sharp corners had a radius of about 0.008 in. It may be noted that as the corner

radius increases, the value of K_f initially increases and then decreases. In other words, the specimens with sharp cornered openings have a higher fatigue strength than those having a radius of 1/32 in., although the elastic stress concentration factor for the former will be much higher than that of the latter. This peculiar behaviour is associated with high gradients of stress which occur at very sharp discontinuities containing high stress concentrations. The stress gradient, which is not a dimensionless quantity, depends on the size of the specimen. The "size-effect" noted in fatigue testing is therefore associated with the stress gradient. The size-effect phenomenon and its relation to stress gradients is illustrated in Figure 56 . In the absence of stress gradient, no size-effect is observed in axially loaded plain specimens (Figure 56 Case 1). On the other hand, in specimens subjected to bending and in notched specimens, a definite size-effect is observed (Figure 56,Cases 2,3).

Since extremely small notches giving infinite theoretical stress produce very little or no reduction in fatigue strength, the curves in Figure 55 are produced to pass through the origin ($K_f = 1$ no reduction in fatigue strength when $r = 0$).

Various theories have been put forward to explain the size-effect phenomenon.

Neuber's Theory

Neuber's elementary block concept is that fatigue failure is governed not by the maximum stress but the average stress over an elementary block of finite size. This means that a higher maximum stress can be withstood when the gradient is high, than when it is low. Neuber points out that the classical theory of elasticity which is based on the assumption of a homogenous material is inapplicable to materials with sharp notches. For a bar containing an extremely small notch, the classical theory predicts high values of elastic, or theoretical, stress concentration factor K_t, whereas experience shows that small notches give no reduction in fatigue strength. Neuber reconsidered the theory of elasticity on the basis of materials composed of numerous small and finite particles, and by taking account of the stress distribution near the point of maximum stress, he arrived at the empirical relation

$$K_A = 1 + \frac{K_t - 1}{1 + \sqrt{A/r}} \qquad \text{.....(2.1)}$$

where

K_A = fatigue strength reduction factor

K_t = geometrical stress concentration factor

r = radius of the notch

A = a material constant having dimensions of length and representing half the width of a Neuber block.

This formula takes into account size-effect by including a dimension of the notch (root radius) and shows trends of size-effect which agree with those found experimentally. It can be shown that when r tends to zero, K_A tends to unity.

The Inherent Flaw Concept

The inherent flaw concept regards the material as containing a number of internal stress concentrations. Irregularities are produced in the micro-stress distribution due to discontinuities introduced by inclusions, cavities or surface irregularities. The resulting stress concentrations can be regarded as originating from "equivalent flaws" of a given size. The influence of internal flaws depends on their size in relation to the region of high stress. This can be illustrated by considering the effect of an external notch on a material containing many internal flaws. If the notch is large compared with the flaws, there will be a number of flaws wholly within the region of high stress at the root of the notch, and reduction in fatigue strength will be considerable. If on the other hand the size of the notch is comparable to the size of the flaw, it amounts to adding to a material, full of stress raisers, one more stress raiser of the same size; and consequently the reduction in fatigue strength, due to the notch, is very small.

An analysis of the interacting effect of equivalent flaws

with geometric stress concentrations leads to an empirical material notch formula suggested by Heywood [27]

$$K_A = \frac{K_t}{1 + 2\left(\frac{K_t - 1}{K_t}\right)\sqrt{\frac{e}{r}}} \qquad \ldots\ldots(2.2)$$

where K_A, K_t and r have the usual meanings and e = the material notch alleviation factor corresponding to the length of equivalent inherent flaws or the flaw parameter.

Heywood has attempted to correlate $\sqrt{e}$ empirically to the tensile strength or fatigue limit of the material, and the type of discontinuity. He has plotted the observed values of notched fatigue limits from results of various experimenters against calculated values using an empirical value of $\sqrt{e}$ based on the type of discontinuity, (hole, groove or shoulder) and either tensile strength or the fatigue limit of the material. The agreement was considered to be satisfactory considering the wide range of specimen shapes and sizes included and the difference in techniques used by different investigators.

Using Heywood's equation, knowing the values of K_A from fatigue tests (S-N curves, Figure 54) and K_t from the steel test (Figure 34), a mean value of $\sqrt{e}$ has been obtained for discontinuities in the form of rectangular openings with radiused corners in ship steel. Using this value of $\sqrt{e}$ in Heywood's equation, the variation of K_A for geometrically similar specimens has been calculated. This mean value of $\sqrt{e}$ obtained from experimental results agrees well with values suggested by Heywood for grooves (Figure 57).

Figure 57 shows plots of K_A versus corner-radius for geometrically similar specimens with square openings with different radius/width ratios. As the radius decreases a point is reached where K_A becomes less than unity signifying that the discontinuity under consideration produces less weakening effect than that due to inherent flaws; the material beyond this point should be considered to have $K_A = 1$. The cross-plots on the curves in Figure 57 correspond to a constant value of the size of the opening, b. Knowing the size of the opening, b, and the $\frac{r}{b}$ ratio, these curves can be used for finding K_A for specimens having square openings with $\frac{b}{B} = 0.5$, thus providing an approximate method of estimating the probable long-life fatigue behaviour of large specimens. For example, for a 24 ft. wide opening in a 48 ft. wide plate, the values of K_A for different $\frac{r}{b}$ ratios would be the ordinates of points 1, m, n, o in Figure 57 . Dividing the fatigue limit of the material by K_A, the average alternating stress over the net section (σ_{an} in the Figure below) which can be applied to such a plate for fatigue failure to take place in 10^7 or more cycles, can be obtained. Values of σ_{an} are tabulated below. The value of the fatigue limit used is that obtained from the S-N curve for ship steel (Figure 54).

(Fatigue limit = 12.8 tons/sq.in.)

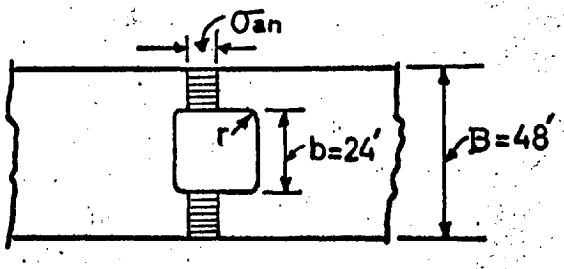

r/b	K_A	$\sigma_{an} = \frac{12.8}{K_A}$ tons/sq.in.
1/93.4	4.06	3.15
1/24	2.75	4.66
1/12	2.40	5.33
1/6	1.98	6.47

(σ_{an} = alternating stress for 10^7 cycles to failure)

The dimensions used in the above example are of the same order of magnitude as those in hatch openings in ships. This very example would be used at a later stage for calculating the alternating stress(σ_{an})for different cycles to failure (from 1/4 to 10^7 cycles).

Effect of Cycles to Failure on Fatigue Strength Reduction Factor

The knowledge of K_A for a given specimen or component gives only the limiting value of fatigue strength reduction factor, but, as was pointed out before, the reduction factor K_f depends upon the cycles to failure and has two limiting values K_s (single pull) and K_A (near the fatigue limit). For a structure subjected to a spectrum of stresses, it is necessary to have a knowledge of K_f over the whole range. In some cases it so happens that some parts are subjected to comparatively few cycles during the service life and parts designed for fatigue limit will be unnecessarily strong.

Heywood suggests an empirical relation for calculating K_f at any life.

$$K_f = K_s + \frac{n^4}{n^4 + d} (K_A - K_s) \qquad \text{.....(2.3)}$$

K_f = fatigue strength reduction factor at a given life.

K_s = strength reduction factor under static loading

K_A = limiting fatigue strength reduction factor

n = log of number of cycles to failure

d = a constant which depends upon the material and, for simple geometric notches, is independent of the type of the notch.

For steels Heywood suggests a value of $d = \left(\frac{1750}{\sigma t}\right)^2$ where σt is the tensile strength in KSI. As very few experimental results are available in the literature giving complete S-N diagrams

for reversed loading of plain and notched specimens, the relation has not been verified to a great extent and may be considered to be very approximate.

Heywood's equation may be rewritten as

$$K_f = K_s + \psi (K_A - K_s)$$

where $$\psi = \frac{n^4}{n^4 + d}$$

Figure 58 shows a plot of ψ versus life using

$d = \left(\frac{1750}{70.5} \right)^2 = 615$ (σt was found to be 70.5 KSI for the steel used)

The experimental values of ψ obtained from the relation

$$\psi = \frac{K_f - K_s}{K_A - K_s}$$ (where K_f, K_s, K_A are obtained from the S-N diagrams)

are also marked. There appears to be some scatter, but it can be easily seen that the empirical curve represents the mean of the experimental observations fairly well. The reason for the deviation at $\psi = 1$ is readily apparent. For 10^7 cycles when the experimental S-N curves become horizontal $K_f = K_A$ and $\psi = 1$, whereas the empirical curve for this life gives

$$\psi = \frac{(7)^4}{(7)^4 + 615} = 0.8$$

With the limited amount of test results available for steels with large value of d (that is, with low tensile strengths), no attempt is made to suggest a new empirical expression for d; and the value of 615 is used in the calculations that follow.

Example

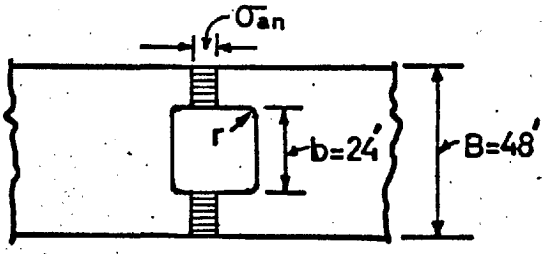

The values of fatigue strength reduction factor K_f for different lives have been calculated for the example treated before (Page 85). The values of limiting fatigue strength reduction factor K_A have been taken from the table on Page 85. K_f has been calculated for different $\frac{r}{b}$ ratios using Heywood's equation

$$K_f = K_s + \frac{n^4}{n^4 + d} (K_A - K_s)$$

(d = 615, K_s is taken as unity)

σ_{an}, the average stress on net section for a given life, is calculated from the relation

$$\sigma_{an} = \frac{\sigma_a}{K_f}$$

where σ_a = fatigue strength of the material for the same life.

The calculations are shown in a tabular form below.

Cycles to Failure	10^7		10^6		10^5		10^4		10^3		10^2	
Material Fatigue Strength σ_a from S-N Diagram in Tons/sq. in.	12·80		13·75		15·75		19·30		24·30		28·90	
	K_A	σ_{an} Tons/sq. in.	K_f	σ_{an} Tons/sq. in.	K_f	σ_{an} Tons/sq. in.	K_f	σ_{an} Tons/sq. in.	K_f	σ_{an} Tons/sq. in.	K_f	σ_{an} Tons/sq. in.
$\frac{r}{b}=\frac{1}{93·4}$	4·06	3·15	3·08	4·47	2·54	6·20 ★	1·90	10·16	1·36	17·91	1·08	26·82
$\frac{r}{b}=\frac{1}{24}$	2·75	4·66	2·19	6·29	1·88	8·37	1·51	12·74	1·20	20·25	1·04	27·80
$\frac{r}{b}=\frac{1}{12}$	2·40	5·33	1·95	7·05	1·71	9·23	1·41	13·67	1·16	20·95	1·03	28·06
$\frac{r}{b}=\frac{1}{6}$	1·98	6·47	1·65	8·35	1·49	10·54	1·29	14·98	1·11	21·88	1·02	28·29

Figure 59 shows plots of σ_{an} versus life for different $\frac{r}{b}$ ratios for the plate considered. The damage to the plate due to a spectrum of alternating stresses can be calculated by plotting the curve representing the spectrum on this figure and applying the cumulative damage rule. Before considering the damage due to a spectrum, the effect of the presence of a mean stress is considered below.

★ This value is referred to on Page 95.

Effect of mean stress

The calculations so far have been done for alternating stresses only. In practice, however, a mean stress is usually present and cycles of stress of different magnitudes are superimposed over the mean value. For example, in ships, the stress reversals are superimposed on the still water bending stress.

In order to take account of the mean stress in a specimen or a component with a geometrical discontinuity, it is essential to know the relation between alternating stress, mean stress and cycles to failure for a plain specimen of the same material. Heywood suggests the following approximate formula for plain specimens of steel [27].

$$\frac{\sigma a}{\sigma t} = \left\{ 1 - \frac{\sigma m}{\sigma t} \right\} \left\{ A_o + \gamma (1 - A_o) \right\} \qquad \ldots\ldots\ldots (2.4)$$

where σa = alternating stress

σm = mean stress

σt = ultimate tensile strength

$A_o = \dfrac{1 + c_1 n^4}{1 + c_2 n^4}$ = value of $\dfrac{\sigma a}{\sigma t}$ at zero mean stress

$\gamma = \dfrac{\sigma m \left(2 + \frac{\sigma m}{\sigma t}\right)}{3\sigma t}$

n = log of cycles to failure

A mean value of each of the constants c_1 and c_2 has been arrived at, by using the experimentally observed values of $\frac{\sigma a}{\sigma t}$ for zero mean stress. Using these values ($c_1 = .0024$, $c_2 = .0063$) the relation between alternating stress, mean stress and cycles to failure, known as "Master Diagram" has been plotted in Figure 60. Tensile mean stresses are of much greater importance than compressive mean stresses in affecting fatigue behaviour. In practice, failures in compression are extremely rare due to increased fatigue strengths. The master diagram is mainly for tensile mean stresses; extrapolation into the compressive zone has been done but limiting conditions (such as the condition of failure to take place in one cycle when $\sigma m + \sigma a = \sigma t$) may not be satisfied in this region. The tensile zone of the master diagram on Figure 60 will be used in the subsequent calculations; these predict the fatigue performance of a large plate specimen with a square opening, subjected to stress reversals superimposed on a given tensile mean stress.

Fatigue strength reduction in the presence of a mean stress

Under repeated loading, mean stress, like alternating stress, is also sensitive to stress concentrations. In fact, for a specimen with stress concentration, there are two fatigue strength reduction factors - one for alternating stress and one for the mean stress. The definition of the strength reduction factor for mean stress can be elucidated with reference to the diagram below.

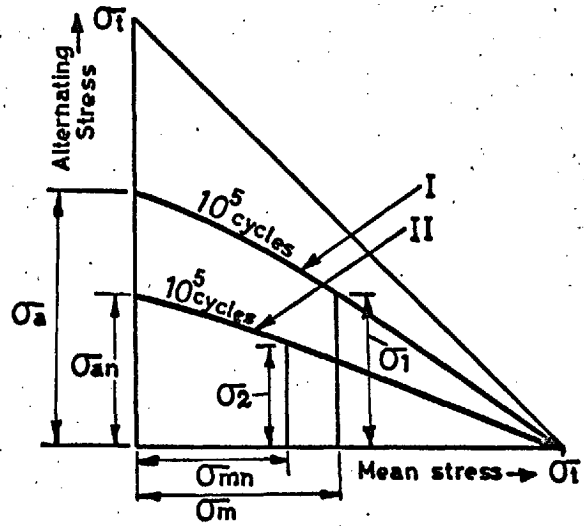

Curve I gives the relation between the alternating stress and the mean stress for a given life (say 10^5 cycles) for the plain material. Curve II gives the relation between the nominal alternating stress and the nominal mean stress for a specimen with stress concentration for the same life.

The alternating strength reduction factor $K_f = \frac{\sigma a}{\sigma an}$.

If two ordinates $\sigma 1$ and $\sigma 2$ are taken on the curves I and II respectively, such that

$$\frac{\sigma 1}{\sigma 2} = \frac{\sigma a}{\sigma an} = K_f$$

then the "mean" strength reduction factor is defined as the ratio of the corresponding abscissae

$$K_m = \frac{\sigma m}{\sigma mn}$$

This definition assumes that the alternating strength reduction factor (K_f) remains the same even in the presence of mean stresses.

An empirical formula for K_m has been suggested by Heywood:

$$K_m = \frac{\sigma m}{\sigma mn} = K_s + (K_A - K_s)\left(1 - \frac{\sigma mn + \sigma an}{\sigma tn}\right)^2 \qquad \ldots\ldots(2.5)$$

where σm, σmn, σan, σt, K_A, K_s are as defined before, and σtn = ultimate tensile strength of a specimen with stress concentration. ($\sigma tn = K_s \ \sigma t$)

The formula indicates that K_m depends upon the nearness of the sum ($\sigma mn + \sigma an$) to the static strength σtn. At static failure when $\sigma mn + \sigma an = \sigma tn$, $K_m = K_s$. Also the value of K_m can never exceed K_A.

Example:-

Heywood's formula (Equation 2.5) was used to calculate the fatigue performance of a large-size plate specimen. The dimensions of the plate were as in the previous example (Page 88). The magnitude of the tensile mean stress was chosen to be 4 tons/sq.in. The still water bending stress in a ship would be of this order.

The calculations were done for an $\frac{r}{b}$ ratio of $\frac{1}{93.4}$. A sample calculation is shown below.

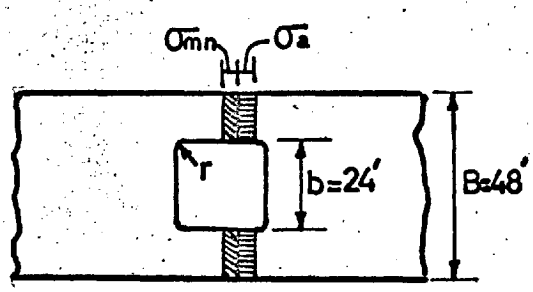

σ_{mn} = 4 tons/sq.in.

σ_t = 31.5 tons/sq.in.

From Page 85 for $\frac{r}{b} = \frac{1}{93.4}$ $K_A = 4.06$

It is required to calculate the nominal alternating stress σ_{an} that can be applied to this plate for failure to take place in 10^5 cycles. The master diagram on Figure 60 will be used in these calculations.

Now

$$\frac{\sigma_m}{\sigma_{mn}} = K_s + (K_A - K_s)\left(1 - \frac{\sigma_{mn} + \sigma_{an}}{\sigma_{tn}}\right)$$

.....(from Equation 2.5)

Putting $\sigma_t = \sigma_{tn}$, $K_s = 1$

the above equation can be rewritten as

$$\frac{\sigma_m}{\sigma_t} = \frac{\sigma_{mn}}{\sigma_t}\left[1 + (K_A - 1)\left(1 - \frac{\sigma_{mn} + \sigma_{an}}{\sigma_t}\right)^2\right] \quad .....(2.6)$$

From equation (2.3)

$$K_f = \frac{\sigma a}{\sigma an} = \left\{ K_s + \frac{n^4}{n^4 + d} (K_A - K_s) \right\}$$

Putting $K_s = 1$

$$\frac{\sigma a}{\sigma t} = \frac{\sigma an}{\sigma t} \left\{ 1 + \frac{n^4}{n^4 + d} (K_A - 1) \right\} \qquad .....(2.7)$$

Putting $\frac{\sigma mn}{\sigma t} = \frac{4}{31.5}$, $K_A = 4.06$ in Equation (2.6)

$$\frac{\sigma m}{\sigma t} = 0.127 + 0.389 \, (0.873 - \frac{\sigma an}{\sigma t})^2 \qquad .....(2.8)$$

Putting $n = 5$, $d = 615$, $K_A = 4.06$ in Equation (2.7)

$$\frac{\sigma a}{\sigma t} = 2.542 \, \frac{\sigma an}{\sigma t} \qquad .....(2.9)$$

By using several trial values of $\frac{\sigma an}{\sigma t}$ in equations (2.8) and (2.9) , such a value was obtained that the point representing the corresponding values of $\frac{\sigma a}{\sigma t}$ and $\frac{\sigma m}{\sigma t}$ lay on the curve for 10^5 cycles in the master diagram (Figure 60).

In this particular case

when $\frac{\sigma an}{\sigma t} = 0.17$,

$$\left.\begin{aligned} \frac{\sigma a}{\sigma t} &= 0.43 \\ \frac{\sigma m}{\sigma t} &= 0.32 \end{aligned}\right\}$$

The point represented by the coordinates $\frac{\sigma a}{\sigma t} = 0.43$, $\frac{\sigma m}{\sigma t} = 0.32$, is on the curve for 10^5 cycles in the master diagram (Figure 60).

Hence $\sigma an = 0.17 \times 31.5 = 5.35$ tons/sq.in. This stress may be compared to the value of 6.2 tons/sq.in. which can be applied when $\sigma mn = 0$. (Table on Page 89 , asterisk mark).

The discontinuous curve in Figure 59 represents the fatigue performance of the plate in the above example for an $\frac{r}{b}$ ratio of $\frac{1}{93.4}$ and with a mean stress of 4 tons/sq.in. This curve may be compared with the corresponding curve for zero mean stress on the same diagram. It may be noted that a mean stress of 4 tons/sq.in. does not change the fatigue behaviour of the plate considerably. Calculations taking account of the effect of mean stress were therefore not done for the other $\frac{r}{b}$ ratios.

Damage due to a stress-spectrum

The average stress histogram of a ship [42] has been superimposed on Figure 59. The histogram was obtained from measurements on several ships at sea reported by Johnson and Larkin [43]. The measurements were taken for a limited period; but for the sake of the example, a rough estimate is made of the number of reversals that a ship may get in an arbitrary period of 100 years. The number of sailing hours per year was assumed to be 6000. According to Miner's hypothesis the damage at a particular level of stress is given by the ratio $\frac{n'}{n}$

where n' = number of reversals at the given stress level

n = number of reversals required at the same stress level to cause failure.

The total damage is given by $\sum \frac{n'}{n}$. In the application of Miner's hypothesis n' and n were taken as values corresponding to the middle of the stress range considered. n was referred to the curve corresponding to $\frac{r}{b} = \frac{1}{93.4}$ and an assumed mean stress of 4 tons/sq.in.

The table below shows two sets of calculation of damage at different stress levels. One of the sets refers to the average histogram mentioned above. The second set refers to the histogram of one of the several ships from which the average was obtained.

1	2		3	4		5	
Stress Amplitude (Semi range) tons/sq. in.	n' in 100 years		n	$\frac{n'}{n}$		$\frac{n'/n}{\sum n'/n} \times 100$	
	Average Histogram	Histogram of one ship		Average Histogram	Histogram of one ship	Average Histogram	Histogram of one ship
0·5 to 1	18516300	2510800	∞	0	0	0	0
1 to 1·5	1724900	393300	∞	0	0	0	0
1·5 to 2	198200	285900	∞	0	0	0	0
2 to 2·5	30000	115300	∞	0	0	0	0
2·5 to 3	6300	46800	10×10^6	·0006	·0047	13%	11%
3 to 3·5	1130	8500	2×10^6	·0006	·0043	13%	10%
3·5 to 4	232	1460	1×10^6	·0002	·0015	$4\frac{1}{2}$%	4%
4 to 4·5	93	729	450,000	·0002	·0016	$4\frac{1}{2}$%	4%
5	45	438	15,000	·0030	·0290	65%	71%

$\sum \frac{n'}{n}$ = 0·0046 0·0411

The total damage $\sum \frac{n'}{n}$ when referred to the average histogram is 0.0046 and the corresponding value for the histogram of one of the ships is 0.0411. Failure takes place when $\sum \frac{n'}{n} = 1$. In both cases the total damage is very small. Column 5 in the table gives the damage as a percentage of the total damage. It may be noted that the rate of damage for the two cases considered is nearly the same, although the total damage differs considerably. The nature and severity of stress spectrum (and hence the damage) may differ considerably for different ships. (Nibbering [23] points out that the stress spectrum of "Canada" in one month was nearly as severe as that of "Ocean Vulcan" in thirty years). Secondly, the effect of welding and corrosion has not been taken into account in the above calculations and these factors will adversely affect the fatigue behaviour of the plate.

Effect of the length of a rectangular opening

Figure 61 shows the S-N diagrams for two batches of specimens with different lengths of openings but equal corner radii. The S-N diagrams for the two opening sizes ($\frac{3}{4}$" x $\frac{3}{4}$", $\frac{3}{4}$" x $\frac{3}{8}$") were found to be very close and further fatigue tests on a third batch of specimens with a different length of opening ($\frac{3}{4}$" x 1 $\frac{1}{2}$") were discontinued. The photoelastic tests also indicated small variation of stress concentration with length of opening, thus lending further support to the discontinuation of the tests.

THEORY

The general stress distribution in plates with rectangular openings was found using the finite difference approach - the computation being carried out by the Atlas computer. Relaxation solutions for a plate with a fixed length to breadth ratio, stiffened in two directions and containing a square hole have been obtained before. (44)

Governing Equations

The stress-strain relations for a sheet are

$$\sigma_x = \frac{E}{1-\rho^2}\left[\frac{\partial u}{\partial x} + \rho\frac{\partial v}{\partial y}\right]$$

$$\sigma_y = \frac{E}{1-\rho^2}\left[\frac{\partial v}{\partial y} + \rho\frac{\partial u}{\partial x}\right] \qquad \text{.....(2.10)}$$

$$\tau_{xy} = \frac{E}{2(1+\rho)}\left[\frac{\partial u}{\partial y} + \frac{\partial v}{\partial x}\right]$$

For a plate stiffened in longitudinal and transverse directions it may be assumed that the stiffeners are spread out to form equivalent sheets having no shear resistance.

Defining $\bar{\sigma}_x$, $\bar{\sigma}_y$, $\bar{\tau}_{xy}$ as the mean applied stresses such that $h\bar{\sigma}_x$, $h\bar{\sigma}_y$, $h\bar{\tau}_{xy}$ are the forces per unit length of the plate stiffener combination (equivalent sheet), the equations of equilibrium are

$$\frac{\partial \bar{\sigma}_x}{\partial x} + \frac{\partial \bar{\tau}_{xy}}{\partial y} = 0$$

$$\frac{\partial \bar{\sigma}_y}{\partial y} + \frac{\partial \bar{\tau}_{xy}}{\partial x} = 0 \qquad \text{.....(2.11)}$$

(h = plate thickness)

If α_x and α_y are the stiffener areas expressed as a fraction of the plate area, and σ_{xs}, σ_{ys} are the stresses in the stiffening members

$$\bar{\sigma}_x = \sigma_x + \alpha_x \sigma_{xs}$$
$$\bar{\sigma}_y = \sigma_y + \alpha_y \sigma_{ys}$$
$$\bar{\tau}_{xy} = \tau_{xy} \qquad \text{.....(2.12)}$$

(assuming the stiffeners do not contribute to the shearing resistance of the equivalent sheet)

The stresses in the stiffening members are given by

$$\sigma_{xs} = E\frac{\partial u}{\partial x}$$
$$\sigma_{ys} = E\frac{\partial v}{\partial y} \qquad \text{.....(2.13)}$$

Substituting for $\bar{\sigma}_x$, $\bar{\sigma}_y$, $\bar{\tau}_{xy}$ from (2.12) in (2.11)

$$\frac{\partial \sigma_x}{\partial x} + \alpha_x \frac{\partial \sigma_{xs}}{\partial x} + \frac{\partial \tau_{xy}}{\partial y} = 0$$
$$\frac{\partial \sigma_y}{\partial y} + \alpha_y \frac{\partial \sigma_{ys}}{\partial y} + \frac{\partial \tau_{xy}}{\partial x} = 0 \qquad \text{.....(2.14)}$$

Using expressions (2.11) and (2.13) the equations (2.14) can be expressed in terms of derivatives of displacements

$$2\left[1+\alpha_x(1-\hat{\rho})\right]\frac{\partial^2 u}{\partial x^2} + (1-\rho)\frac{\partial^2 u}{\partial y^2} + (1+\rho)\frac{\partial^2 v}{\partial x \partial y} = 0$$
$$2\left[1+\alpha_y(1-\rho^2)\right]\frac{\partial^2 v}{\partial y^2} + (1-\rho)\frac{\partial^2 v}{\partial x^2} + (1+\rho)\frac{\partial^2 u}{\partial x \partial y} = 0 \qquad \text{.....(2.15)}$$

Finite difference relations for derivatives at point 0 on a grid with unequal mesh size in different directions were derived in the section on superstructures.

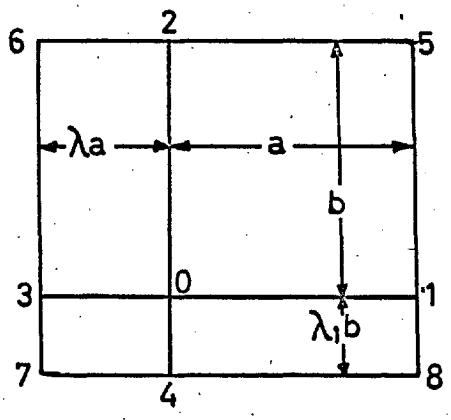

$$\left[\frac{\partial u}{\partial x}\right]_0 = \frac{\lambda^2 u_1 - u_3 + u_0(1-\lambda^2)}{a(\lambda^2+\lambda)}$$

$$\left[\frac{\partial u}{\partial y}\right]_0 = \frac{\lambda_1^2 u_2 - u_4 + u_0(1-\lambda_1^2)}{b(\lambda_1^2+\lambda_1)}$$

$$\left[\frac{\partial^2 u}{\partial x^2}\right]_0 = \frac{\lambda u_1 + u_3 - u_0(1+\lambda)}{\frac{a^2}{2}(\lambda^2+\lambda)}$$

$$\left[\frac{\partial^2 u}{\partial y^2}\right]_0 = \frac{\lambda_1 u_2 + u_4 - u_0(1+\lambda_1)}{\frac{b^2}{2}(\lambda_1^2+\lambda_1)}$$

.....(2.16)

$$\left[\frac{\partial^2 u}{\partial x \partial y}\right]_0 = \frac{\lambda_1^2\left[\lambda^2 u_5 - u_6 + u_2(1-\lambda^2)\right] - \left[\lambda^2 u_8 - u_7 + u_4(1-\lambda^2)\right] + (1-\lambda_1^2)\left[\lambda^2 u_1 - u_3 + u_0(1-\lambda^2)\right]}{ab(\lambda^2+\lambda)(\lambda_1^2+\lambda_1)}$$

Expressing the derivatives in Equations (2.15) in terms of their finite difference equivalents we obtain

$$F_1\left[\lambda u_1+u_3-(1+\lambda)u_0\right]+F_2\left[\lambda_1 u_2+u_4-(1+\lambda_1)u_0\right]$$
$$+F_3\left[\lambda_1^2\left\{\lambda^2 v_5-v_6+(1-\lambda^2)v_2\right\}-\left\{\lambda^2 v_8-v_7+(1-\lambda^2)v_4\right\}+(1-\lambda_1^2)\left\{\lambda^2 v_1-v_3+(1-\lambda^2)v_0\right\}\right]=0$$

$$G_1\left[\lambda_1 v_2+v_4-(1+\lambda_1)v_0\right]+G_2\left[\lambda v_1+v_3-(1+\lambda)v_0\right]$$
$$+F_3\left[\lambda_1^2\left\{\lambda^2 u_5-u_6+(1-\lambda^2)u_2\right\}-\left\{\lambda^2 u_8-u_7+(1-\lambda^2)u_4\right\}+(1-\lambda_1^2)\left\{\lambda^2 u_1-u_3+(1-\lambda^2)u_0\right\}\right]=0$$

.....(2.17)

Where

$$\frac{b}{a}=k$$

$$1+\alpha x(1-\rho^2)=1/r_x$$

$$1+\alpha y(1-\rho^2)=1/r_y$$

$$F_1=\frac{4k^2}{r_x(\lambda+\lambda^2)}$$

$$F_2=\frac{2(1-\rho)}{(\lambda_1+\lambda_1^2)}$$

$$F_3=\frac{(1+\rho)k}{(\lambda+\lambda^2)(\lambda+\lambda_1^2)}$$

$$G_1=\frac{4}{r_y(\lambda_1+\lambda_1^2)}$$

$$G_2=\frac{2k^2(1-\rho)}{(\lambda+\lambda^2)}$$

Solving equation (2.17) for each point on a finite difference grid together with the boundary conditions enables displacements and stresses to be computed at all points.

The figure(a) below shows the two cases of plates which were treated. Case 1 is a plate with a single rectangular opening and case 2 is a plate with two openings.

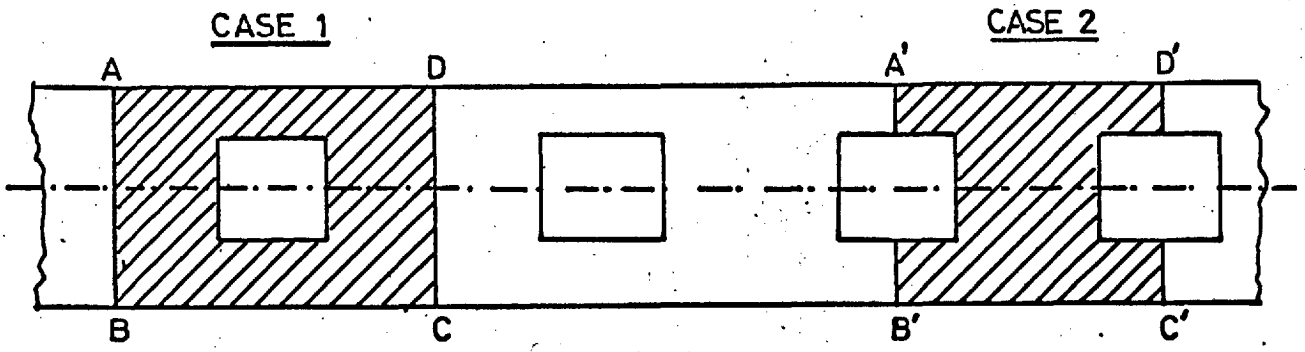

Figure (a)

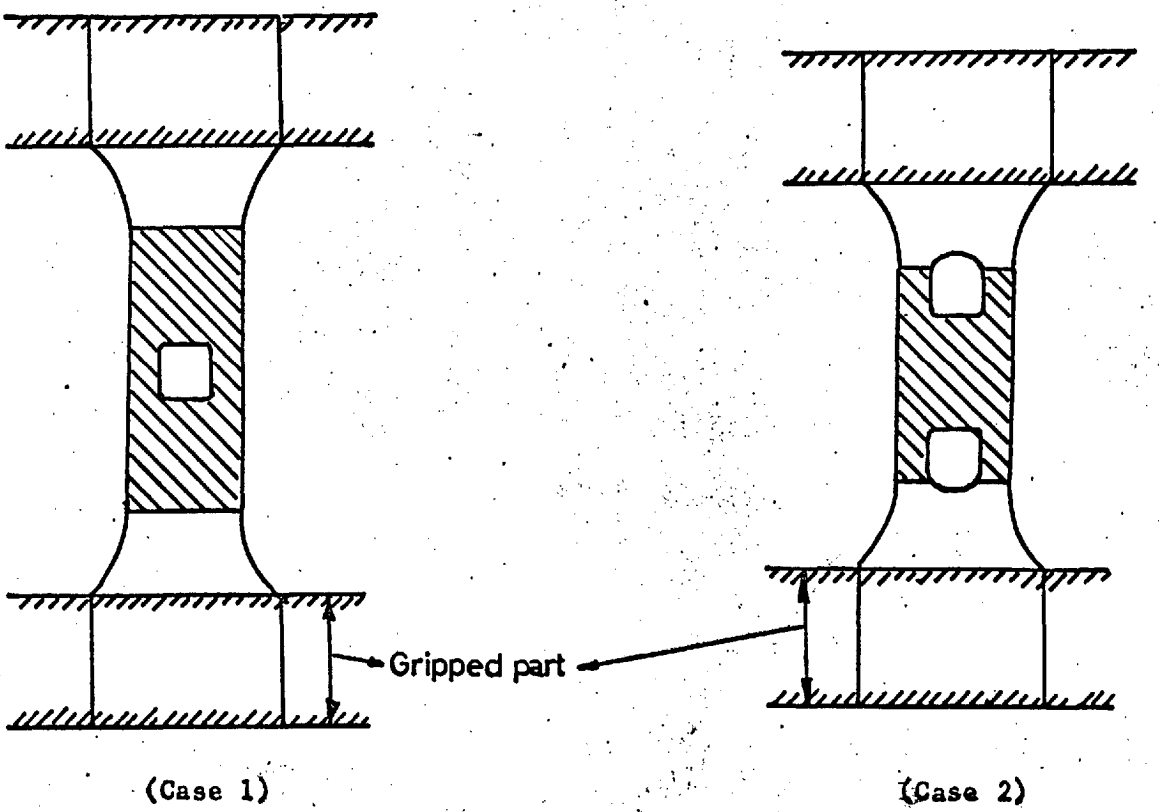

Figure (b)

The plates were assumed to have uniform longitudinal and zero transverse displacements imposed at the ends (AB, CD; A'B', C'D'). This particular boundary condition was chosen to simulate the gripping of the fatigue plate specimens as shown in the figure (in a ship the effect of transverse framing will also be to reduce transverse displacements generally). Due to symmetry, only a quarter of each plate (Figure 62) was analysed. It was divided into two rectangular grids interconnected at the edge of the opening (Figure 62). The division of the plates into the grid was kept such that the resulting matrix could be inverted by the Mercury computer using the matrix inversion routine without recourse to partitioning.

A program was written for the Mercury computer such that it could also be run on the Atlas computer at a later stage when it was installed. The program was capable of generating and solving the simultaneous equations arising out of applying Equations (2.17) to each point on the grid. The size of the matrix was 99 x 99. The pattern of coefficients on a point O on a general grid is shown below.

(i) Pattern of Coefficients for u-displacement equation

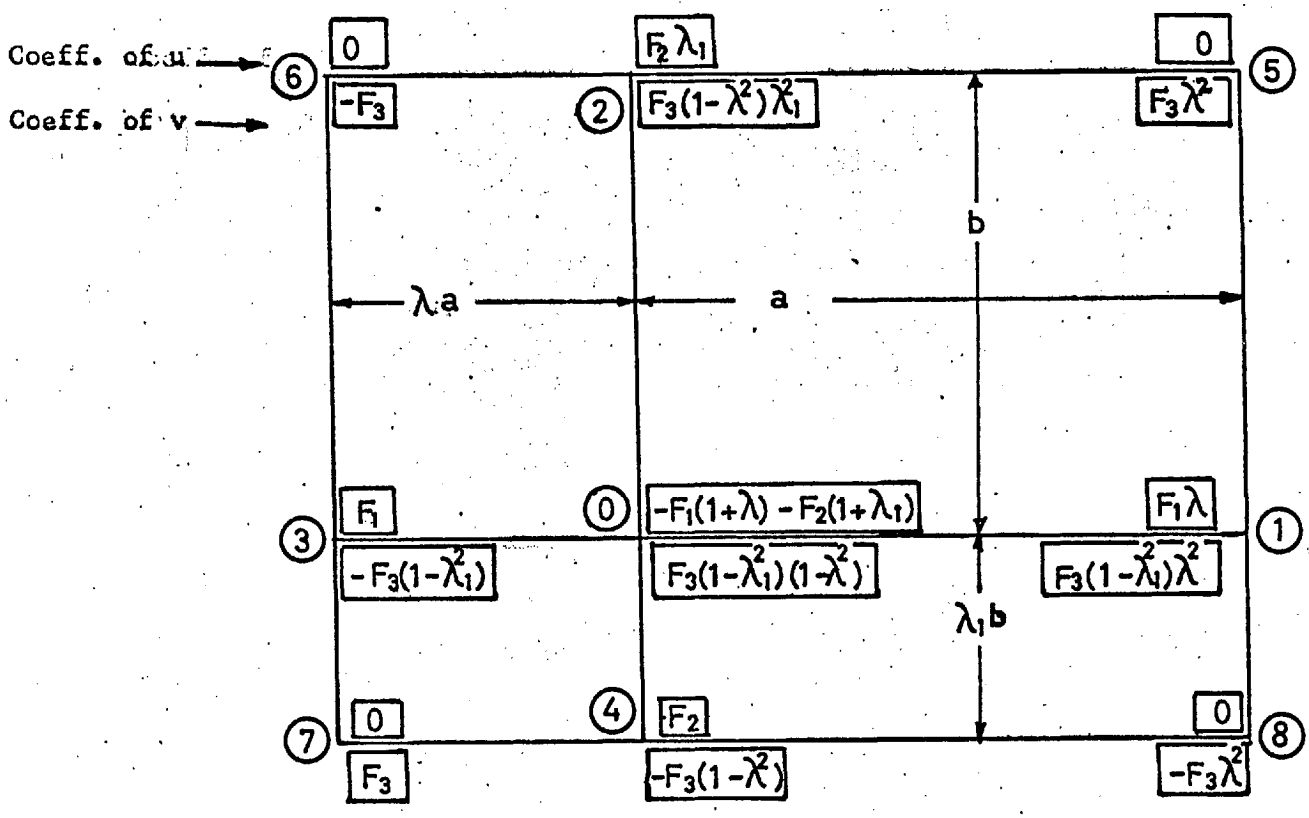

(ii) Pattern of Coefficients for v-displacement equation

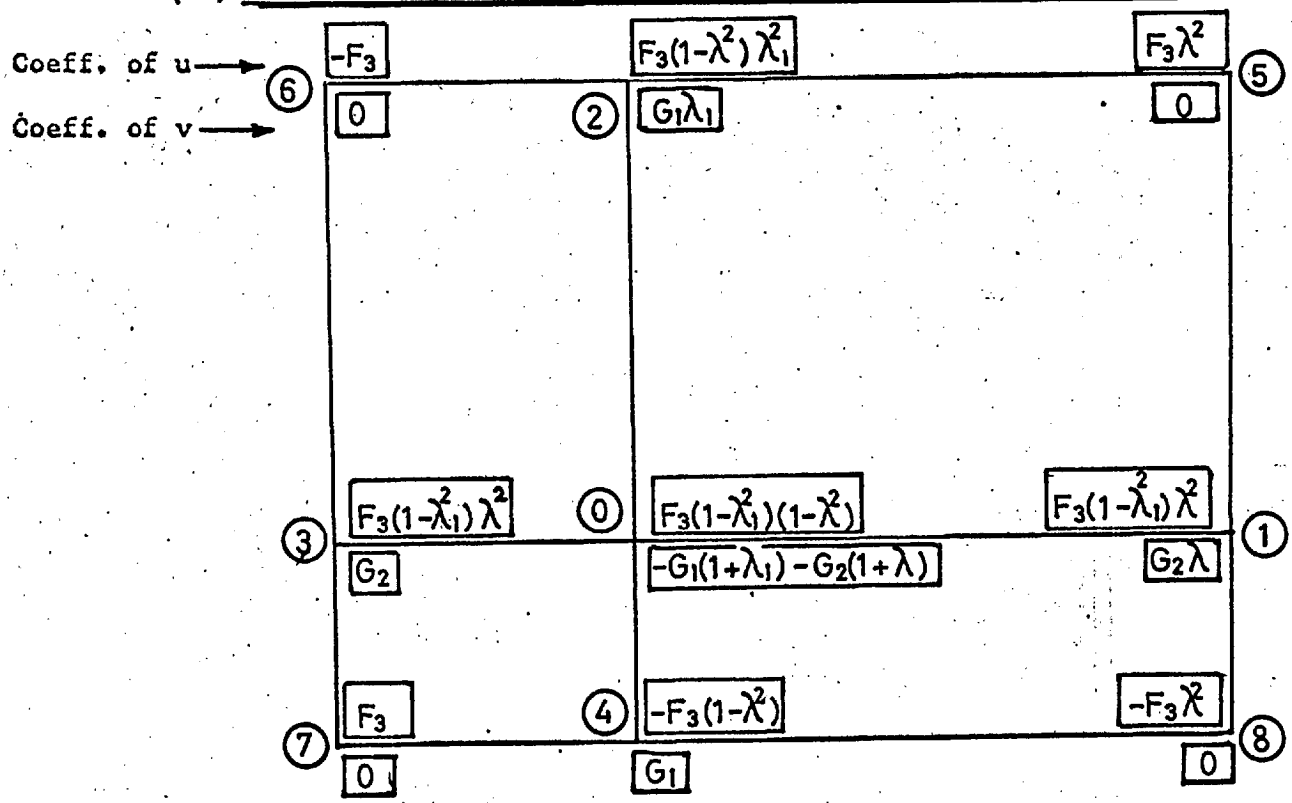

Patterns of coefficients for points which lie on simple rectangular grids were obtained by putting $\lambda_1 = \lambda = 1$ in the above patterns.

By varying the ratio $\frac{b_1}{a_1}$ the length of the opening could be changed and by varying $\frac{b_2}{a_2}$ the distance between them (Figure 62). The applied displacements, stiffener areas, the size and distance between openings and the Poisson's ratio were fed as data in the program. The computer results were in the form of displacements and stresses σ_x , σ_y , τ_{xy} at every point on the grid.

Boundary Conditions

The fictitious external values of displacements at the free boundaries were expressed in terms of the unknown internal displacements using relations (2.12) and (2.13).

(i) At free boundaries x = constant $\quad \bar{\sigma}_x = 0$

$$\left[1+\alpha_x(1-\rho^2)\right]\left[\frac{\lambda^2 u_1 - u_3 + u_0(1-\lambda^2)}{a(\lambda^2+\lambda)}\right] + \rho\left[\frac{\lambda_1^2 v_2 - v_4 + v_0(1-\lambda_1^2)}{b(\lambda_1^2+\lambda_1)}\right] = 0$$

(ii) At free boundaries y = constant $\quad \bar{\sigma}_y = 0$

$$\left[1+\alpha_y(1-\rho^2)\right]\left[\frac{\lambda_1^2 v_2 - v_4 + v_0(1-\lambda_1^2)}{b(\lambda_1^2+\lambda_1)}\right] + \rho\left[\frac{\lambda^2 u_1 - u_3 + u_0(1-\lambda^2)}{a(\lambda^2+\lambda)}\right] = 0$$

(iii) Along all free boundaries $\bar{\tau}_{xy} = 0$

$$\frac{\lambda_1^2 u_2 - u_4 + u_0(1-\lambda_1^2)}{b(\lambda_1^2+\lambda_1)} + \frac{\lambda^2 v_1 - v_3 + v_0(1-\lambda^2)}{a(\lambda^2+\lambda)} = 0$$

At the internal corner the fictitious values u_6 and v_6 were found by extrapolation. The method used was to average the fictitious values (Q', Q" in Figure 62) pertaining to two adjacent points, which had been found by satisfying conditions of zero normal stress and zero shear stress.

At the interconnection of the two grids, values were parabolically interpolated at two points (R,S).

In order to find stresses along the edge where displacements were specified, it was necessary to find fictitious external values of u and v . This was done by applying equations(2.17)at each mesh point along this edge and solving the resulting set of simultaneous equations. This procedure was carried out after having determined the displacements inside the plate, since these external values were not required for the determination of displacements. Parabolic extrapolation was used at the corners where necessary.

Results and Discussion

Tables 8 to 10 give the numerical values of relative longitudinal and transverse displacements u and v for several cases of plates with one or two rectangular openings. The grid-points and the edges on which displacements were imposed are indicated in Figure 62 . The longitudinal and transverse displacements imposed on the loaded edges in every case were 200 units and zero respectively.

Figure 63 shows the displacement diagrams for eight cases - the applied displacement in each case being the same. The four diagrams on the right indicate the effect of changing the length of the opening on displacements, keeping the distance between the ends of the opening and the loaded edge constant. The diagrams on the left indicate the effect of changing the distance between two openings, keeping the lengths of the openings constant.

Figure 64 shows the distribution of longitudinal stresses in the plates on several cross-sections. As the length of the opening decreases, the average rate of change of longitudinal stress across the width of the sides of the opening increases.

Transverse and shear stresses in the plates are, in general, small in magnitude. The maximum transverse stress occurs at the ends of the opening and increases as the length of the opening decreases.

The width of the openings in all the cases discussed above was 50 per cent. of the width of the plate. Figure 65 shows the displacement diagram and longitudinal stresses for a plate with a 60 per cent. opening. The applied displacements at the loaded edge in this case are of the same magnitude as those in the cases already considered. The average rate of change of longitudinal stress across the width of the sides of the opening is greater than the corresponding case in Figure 64.

To check equilibrium, the total force at the centre of the plate across the opening was compared with the applied force at the end. The maximum unbalanced force was found to be about 20 per cent. of the applied force (applied force being greater than the force at the centre of the sides of the opening). One of the reasons for the discrepancy may be the use of two rectangular grids interconnected at the ends of the opening. That this may not be the only reason can be deduced from the fact that a lack of equilibrium of about 10 per cent. was observed in a relaxation solution of a similar problem using a square grid for a plate of fixed geometry with a square opening. Another reason may be the disturbing effect of the assumptions made in obtaining the fictitious point outside the boundary at the internal corner . This assumption presumably has a greater effect if the ratio of the two longitudinal grid-lengths ($\frac{a2}{a1}$) is large, since the lack of equilibrium also increases as this ratio increases.

Comparison with Experimental Results and Suggestions to improve solution

Figure 36 shows the distribution of longitudinal stress in way of a rectangular opening. The photoelastic results at the edges are compared with results obtained by finite difference displacement solutions. The results obtained from the test on the steel specimen are also shown in the figure. The discrepancies increase as the length of the opening decreases. This may be due to the relative proximity of the internal corner at which position the finite difference solutions are most in error due to the effect of the assumptions made in obtaining the fictitious points outside the boundary at this corner. Presumably, the effect of the assumption increases with the grid size ratio ($\frac{a2}{a1}$) (Figure 62).

An examination of the discrepancies observed in the finite difference solution leads to the following suggestions which may be considered for improving the solution.

A square mesh should be used instead of the two interconnected rectangular grids. The length of the opening, its width and the distance between two openings can be changed by keeping the number of mesh-points variable. The figure below shows a quarter of the subdivided plate.

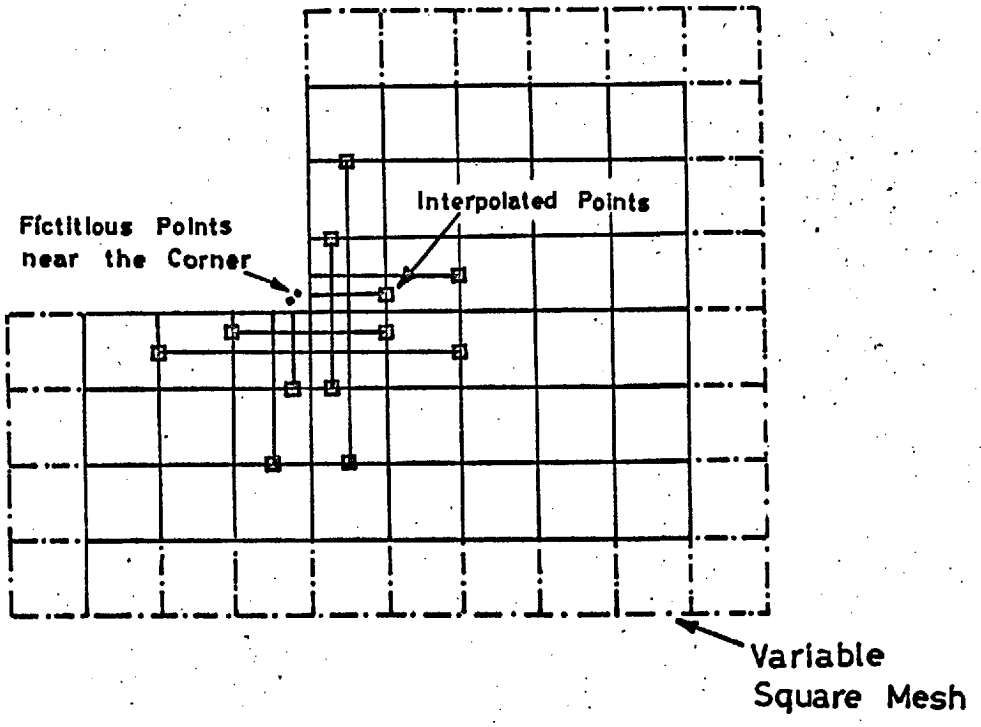

In order to minimize the error due to the effect of the assumptions made at the internal corner for calculating the fictitious boundary point, the mesh near the corner should be made finer and connected to the main grid. The above figure shows a possible grading at the corner. The number of equations resulting from the proposed subdivision would be large but with the available computer facilities, this does not present a big problem. For a very large matrix, partitioning of the matrix can be resorted to.

As the general distribution of stress in the plate will, in general, be unaffected by the corner-radius, the above subdivision with a sharp-cornered opening is adequate for finding this distribution. The variation of "point-forces" at the corner can also be studi d using this subdivision.

If the variation of the position and magnitude of stress concentration for a plate with openings having radiused corners is to be studied using a numerical technique, the finite element method may prove to be more useful. The subdivision of the plate near the radiused corner is simpler using the finite element method [39]. Using the finite difference technique, on the other hand, may entail the use of a polar coordinate system in the region of the radiused-corner and an interconnection of the polar and cartesian coordinate systems - at some distance away from the corner.

Variation of "Point-forces"

All the stresses at the corners of the openings are indeterminate but the "point-force" spread over a grid length can be estimated by applying conditions of equilibrium (figure below).

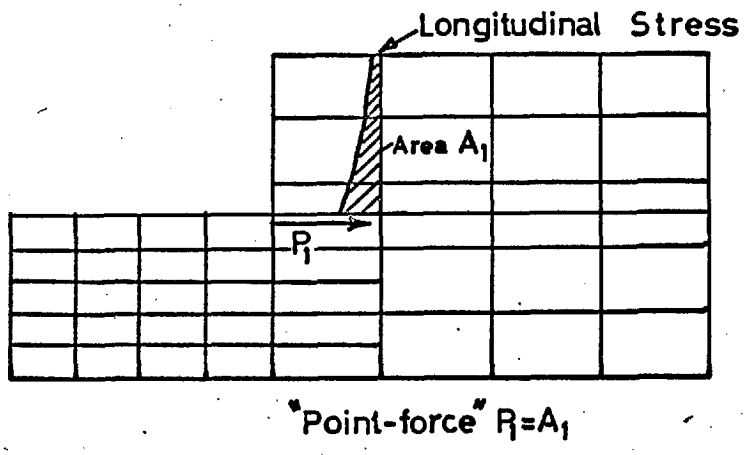

In the case of a single opening, it was found that the point-force increases as the length of the opening decreases. From the photoelastic results (Figure 29) it may be seen that for a given radius the concentration of stress also increases as the length of the opening decreases. The actual concentration of stress depends upon the manner in which the "point-force" is dispersed at the corner, but the magnitude of the "point-force" may be taken as a rough measure of the stress concentration in order to study the trends in its variation with geometrical parameters.

In the case of two openings, direct comparisons between the magnitudes of "point-forces" corresponding to different distances between the openings, can not be made because of the changing grid-lengths, but in general the point-force increases with the distance between the openings.

In discussing the concept of "point-forces" a comment may be made regarding the "energy absorption criterion" used by Degarmo (12) while comparing the various hatch corner details used in the Liberty ships. Degarmo demonstrated that hatch corners having greater absorption of energy during tensile breaking-tests showed

better performance in the Liberty ships. Although the relative performance of corner details as predicted by the energy asorption criterion, agreed with that of actual ships, the basis of comparison is open to criticism. A ship is subjected to a spectrum of stress reversals; therefore predictions based on results from tests in which the specimen is subjected to a single pull, may not be reliable.

The plate specimens tested in the present investigation, with square openings of different corner-radii, were found to break under static load at approximately the same nominal stress and overall elongation. This indicates that the energy absorbed was independent of the corner-radius. On the other hand, the fatigue behaviour was found to vary considerably with the corner-radii.

Although the energy absorption criterion has been successfully used to indicate, qualitatively, the relative performance of large-size structural details (possibly of brittle steel), it is unlikely to have general application as a measure of fatigue performance.

CONCLUSIONS

Superstructures

A new stress-relieving cut has been evolved which reduces the stress at the root of the expansion joint to a reasonable value. A value of 3 was observed for the shape considered (values as high as 17 have been recorded on actual ships [9]). Similar cuts might be used in analogous situations near other discontinuities.

The finite difference technique has been applied to calculate the effect of the depth of a cut (representing an expansion joint) on the general stress distribution in idealised plate-projections. The agreement between numerical and experimental results was found to be good. It was found, for example, that to reduce the stress at the top of a given 1:6 plate projection (see Page 29) to 25 per cent. of the simple bending stress (which would be present at the top of the uncut projection if there were no shear lag), the depth of a central cut should be 75 per cent. of the depth of the projection.

Hatch Openings

Tests on plates with rectangular openings showed that the geometrical stress concentration factor decreases with increasing length, width and corner-radius of the opening. The values of the stress concentration factor obtained from tests on a steel

plate specimen with a square opening were found to be 4, 2.8, 2.4 and 2 for radius/opening-width ratios of $\frac{1}{66}$, $\frac{1}{24}$, $\frac{1}{12}$ and $\frac{1}{6}$ respectively. The values obtained by photoelasticity for rectangular openings were found to be low compared to the infinite plate solutions and compared to the steel plate results, especially for small corner-radii. Photoelastic results for small circular openings (giving large thickness/radius ratios) were also found to be low compared to the plane stress solutions. The low values obtained photoelastically remain unexplained, but it is possible that the incident light was not exactly perpendicular to the plane of the specimen.

Fatigue

Tests on specimens with circular openings showed that the effect of surface finish on fatigue behaviour is more pronounced in specimens with discontinuities than in plain specimens (Figures 39 and 40).

The greater strength reduction factor for the small machined specimens with square openings occurred for the specimens having $\frac{r}{b} = \frac{1}{24}$ (Figure 55). The specimens with $\frac{r}{b} = \frac{1}{93}$ had a longer life, and this is explained in accordance with theories of fatigue failure which take account of the effect of stress gradients. The correlation between the test results and empirical relations

suggested by Heywood was found to be good. (Figures 57 and 58).

Using the existing theories, the effect of varying corner-radius on the probable fatigue behaviour for an opening of ships' dimensions was studied. The predicted fatigue performance for a $\frac{r}{b}$ ratio of $\frac{1}{93}$ in this case was found to be inferior to that corresponding to the ratio $\frac{1}{24}$.

The effect of corner-radius was found to be high at low stress levels. For $\frac{r}{b} = \frac{1}{93}$, the effect of the presence of a mean stress (4 tons/sq.in. tensile) was also included; no drastic change in fatigue behaviour was observed (Figure 59). The damage to the plate was found to be small; the damage would be much increased by welding or corrosion.

General

Finite difference technique has been used to find stress distribution in plates with discontinuities. The concept of "point-forces" (calculated from the general stress distribution) is shown to be useful to study trends in the variation of stress concentration with a geometrical parameter, such as the length or width of an opening.

REFERENCES

1. Timoshenko, S. Stress concentration in the history of strength of materials. Society for Experimental Stress Analysis, Vol. XII, No. 1, 1954.

2. Chapman, J. C. and Sparkes, S. R. Experiments on Box Girders: Some contributions to the theory of ships' structures. Trans. Instn. Engineers and Shipbuilders in Scotland, 1956.

3. Johnson, A. J. and Ayling, P. W. Measurements and Predictions of the influence of deckhouses on the strength of ships. Trans. North-East Coast Institution of Engineers and Shipbuilders, Vol. 77, p. 161, 1962.

4. Johnson, A. J. Stresses in deckhouses and superstructures. Trans. I.N.A., Oct. 1957, Vol. 99, No. 4.

5. Chapman, J. C. The Interaction between a ship's hull and a long superstructure. Trans. I.N.A., Oct. 1957, Vol. 99, No. 4.

6. 60th Anniversary Series. The Society of Naval Architects of Japan. Vol. 9, 1964.

7. Chapman, J. C. The behaviour of long deckhouses. Trans. I.N.A., 1961.

8. Chapman, J. C. Stresses in rectangular plate projections. The Engineer, December, 1954.

9. Bell, A. O. The stress distribution in the deckhouse of a Passenger Liner with one expansion joint. The Shipbuilder and Marine Engine-builder, Vol. 71, No. 676, Jan. 1964.

10. Wilson, J. L. The S.S. Leviathan Damage Repairs and Strength Analyses. Trans. American Society of Naval Architects and Marine Engineers, 1958.

11. Chapman, J. C., Sarna, S. P. and Taylor, P. F. A new stress-relieving Device for Superstructure Expansion Joints. B.S.R.A. report NS 74, 1964. International Shipbuilding Progress, 1966.

12. De Garmo, E. Paul. Tests of Various Designs of Welded Hatch Corners of Ships. Welding Journal, Vol. 27, Feb. 1948.

13. Heller, S. R. Jr., Brock, J. S. and Bart, R. Stresses around Rectangular Opening with rounded corners in uniformly loaded plate. Proc. 3rd U.S. Congress of Applied Mechanics, 1958.

14. Wittrick, W. H. Stress Concentrations for a Family of Uniformly Reinforced Square Holes with Rounded Corners. Aeronautical Quarterly, Vol. XIII Part 3, August, 1962.

15. Steneroth, E., Lindau, L. and Önnermark, B. Photoelastic Investigation of Stress Concentration at Hatch Corners. The Royal Institute of Technology. Division of Naval Architecture, Stockholm, Sweden, Dec. 1962.

16. Gibsztein, M. Stress Concentration at Rectangular Openings with rounded corners in plates of finite dimensions. European Shipbuilding, No. 4, 1964.

17. Richardson, W. S. and Ossowski, W. Stress Concentration in way of Hatch Corners, Part I. Effect of Insert Plates and Shape of Coamings. N.A. report 20. B.S.R.A. report N.S. 73, 1964.

18. Ossowski, W. Stress Concentration at Hatch Corners. Research Item SS 2 B.S.R.A. report NA 160/LS, April, 1964.

19. Williams, M. and Taylor, K. V. Full scale measurements of Stress Concentrations in way of Hatch Corners. N.A. report No. 14, B.S.R.A. report NS 59.

20. Fatigue of Engineering Structures. Report of the Committee appointed by the Department of Scientific and Industrial Research, 1960. Chairman: Sir A. Pugsley.

21. Besukladov, W. F. and others. Fatigue of Shipbuilding steels and strength of ship structures. Int. Conf. on Fatigue of Metals, Instn. of Mech. Engnrs, the A.S.M.E., 1956.

22. Vedeler, G. A naval architect's reflections on some research problems with ship steel. Ship Structure Committee report No. SSC 140, Aug., 1961.

23. Nibbering, J. J. W. Fatigue of Ship Structures. International Shipbuilding Progress, Vol. 10, Sept. 1963, No. 109.

24. Steneroth, E. Low Cycle Fatigue. International Ship Structures Congress, 1961.

25. Proc. International Ship Structures Congress, 1964. Report of Committee 7 on Low Cycle Fatigue.

26. Rules and Regulations for the Construction and Classification of Steel Ships, 1965. Lloyds Register of Shipping.

27. Heywood, R. B. Designing Against Fatigue. Chapman and Hall Ltd., 1962, London.

28. Vedeler, G. To what extent do brittle fracture and fatigue interest shipbuilders today. Houdremont Lecture, June, 1962.

29. Nibbering, J. J. W. The interconnection of Longitudinal Frames at Transverse bulkheads in tankers. Ship Structures Laboratory Technological University - Delft. Report 77, March, 1961.

30. Weck, R. Fatigue in Ship Structures. Trans. I.N.A., 1953.

31. Yao, J. T. P. and Munse, W. H. Low cycle fatigue behaviour of Axially Loaded Specimens of Mild Steel. SSC-151. Ship Structure Committee. U.S. Dept. of Commerce, Office of Technical Services.

32. Rolfe, S. T. and Munse, W. H. Crack propagation in low-cycle fatigue of Mild Steel. SSC 143. Ship Structure Committee. U.S. Dept. of Commerce, Office of Technical Services.

33. Harris, D. J. and Benham, P. P. The effect of High Strain Fatigue Cycles on the Brittle Ductile Transition of Two Mild Steels. B.S.R.A. report NA 166/Mat. Research Item SS 10, April, 1964.

34. Steneroth, E. Fatigue and Cumulative Damage of Ship's Hull. Numerical Methods Applied to Shipbuilding. Oslo - Bergen, 27 Sept.-3 Oct. 1963.

35. Haas, T. Loading Statistics as a Basis of Structural and Mechanical Design. Engineers' Digest, March, April, May, 1962.

36. Schooling, N. J. Stress Distribution in a rectangular opening in an infinite plate under uniform Axial Tension. B.S.R.A. report NA/279/SS

37. Peterson, R. E. Stress Concentration Design Factors John Wiley and Sons Inc., New York, 1953.

38. Siebel, E. and Gaier, M. The Influence of Surface Roughness on the Fatigue Strength of Steels and Non-Ferrous Alloys. The Engineers' Digest, March 1957, Vol. 18, No. 3.

39. Moe, J. Proceedings of the International Ship Structures Congress, Vol. VII. Miscellaneous Discussions, July, 1964. Delft, Netherlands.

40. Chapman, J. C. and Williams, D. G. Investigation on Hatch Openings. Second Progress Report: The effect of Thickness/Radius Ratio on Stress Concentration Factor. B.S.R.A. report NA/299/SS November, 1965

41. Forrest, P. G. Fatigue of Metals. Pergamon Press, London, 1962.

42. Chapman, J. C. Developments in Ship Structures. Structural Engineer, 1966.

43. Johnson, A. J. and Larkin, E. Stresses in Ships in Service. Trans. I.N.A., Vol. 106, 1964.

44. Chapman, J. C. The stresses in a stiffened Plate containing a square hole. (Research Item S2) B.S.R.A. report RB 962 SS (a) 119, 1953.

NOTATION

N_x, N_y	Normal components of forces per unit length, parallel to x and y axes.
σx, σy	Normal components of stresses parallel to x and y axes.
N_{xy}	Shear force per unit length in xy plane.
τxy	Shear stress component in xy plane.
h	Plate thickness.
u, v	Displacements in x and y direction.
εx, εy	Unit elongation in x and y direction.
γxy	Shear strain component in xy plane.
E	Modulus of elasticity.
G	Modulus of elasticity in shear.
ρ	Poisson's ratio.
F	Force function.
a	Size of mesh in x direction.
b	Size of mesh in y direction. (also width of a rectangular opening in the Section on Hatch Openings).
B	Width of a plate with a rectangular opening.
r	Radius of a circular opening or the corner radius of a rectangular opening.
σa	Alternating stress on a plain specimen.

σ_{an} — Nominal σ^{net} alternating stress on a specimen with a discontinuity.

σ_m — Mean stress on a plain specimen.

σ_{am} — Nominal σ^{net} mean stress on a specimen with a discontinuity.

σ_t — Tensile strength of a material.

σ_{tn} — Nominal σ^{net} tensile breaking stress of a specimen with a discontinuity.

K_s — Static strength reduction factor = $\frac{\sigma_t}{\sigma_{tn}}$.

K_f — Fatigue strength reduction factor at any cycles to failure.

K_A — Limiting fatigue strength reduction factor (for 10^7 cycles or more).

K_m — Mean fatigue strength reduction factor.

$\bar{\sigma}_x$, $\bar{\sigma}_y$, $\bar{\tau}_{xy}$ — "Mean applied stresses" in the plate-stiffener combination (such that h $\bar{\sigma}_x$, h $\bar{\sigma}_y$, h $\bar{\tau}_{xy}$ are forces per unit length in the plate-stiffener combination).

α_x, α_y — Areas of longitudinal and transverse stiffeners expressed as a fraction of plate area.

$$r_x = \frac{1}{1 + \alpha_x (1 - \rho^2)}$$

$$r_y = \frac{1}{1 + \alpha_y (1 - \rho^2)}$$

σ_{xs} — Direct stress in longitudinal stiffening member.

σ_{ys} — Direct stress in transverse stiffening member.

H	Height of a plate projection.
σe	Principal stress at a point of stress concentration.
$\sigma e(max)$	Principal stress at the point of maximum stress concentration.
σN	Nominal stress across the net section of a plate with a geometrical discontinuity.
K_t	Geometrical stress concentration factor $= \frac{\sigma e}{\sigma N}$
$K_{t\ (max)}$	Maximum geometrical or elastic stress concentration factor.
A	Material constant in Neuber's equation.
e	Notch alleviation factor or flaw parameter (Heywood's equation).

Cut-out shape	$\frac{\sigma e \text{ (max)}}{\sigma N}$	$\frac{\sigma e \text{ on centre of cut}}{\sigma N}$	Theoretical $\frac{\sigma e \text{ (max)}}{\sigma N}$
1(a)	2.51	2.22	
1(b)	2.09	1.98	
1(c)	2.09	2.09	
1(d)	2.09	2.09	1.88
2	1.92	1.92	

TABLE 1

Stress Concentration Factors

(Superstructure Expansion Joint)

Effect of Length of Opening

B	b	b/B	r	r/b	L	L/b	$K_{t_{max}}$
4"	2"	0.5	.083"	.042	.625"	.313	2.57
4"	2"	0.5	.083"	.042	1"	0.5	2.21
4"	2"	0.5	.083"	.042	2"	1.0	2.05
4"	2"	0.5	.083"	.042	3"	1.5	1.97
4"	2"	0.5	.083"	.042	4"	2	1.92

Effect of Radius at Corner of Opening

4"	2"	0.5	.333"	.167	2"	1	1.88
4"	2"	0.5	.167"	.083	2"	1	1.97
4"	2"	0.5	.083"	.042	2"	1	2.05
4"	2"	0.5	.047"	.024	2"	1	2.31

Effect of Width of opening

4"	2"	0.5	.083	.042	4"	2	1.92
4"	2.5"	0.625	.083	.033	4"	1.6	1.74
4"	3"	0.75	.083	.028	4"	1.33	1.63

TABLE 2

Effect of Hatch Dimensions on Stress Concentration

(Photoelastic results)

B	b	b/B	r	r/b	L	L/b	Kt_{max}
2'-9"	1'-4½"	0·5	2 ¾"	1/6	1'-4½"	1	2·0
2'-9"	1'-4½"	0·5	1 ⅜"	1/12	1'-4½"	1	2·4
2'-9"	1'-4½"	0·5	11/16"	1/24	1'-4½"	1	2·8
2'-9"	1'-4½"	0·5	¼"	1/66	1'-4½"	1	4·0

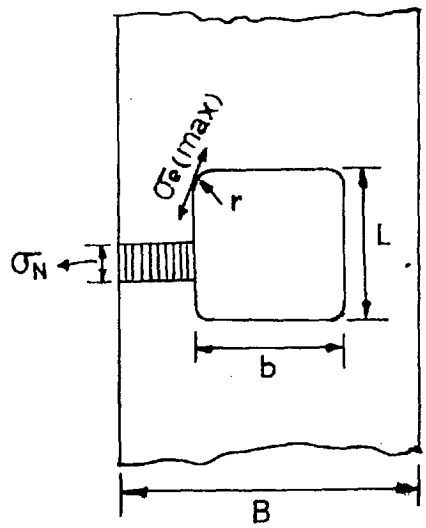

$$K_{t\,max} = \frac{\sigma_{e(max)}}{\sigma_N}$$

TABLE 3

Stress Concentration Factors
(Hatch Openings)
Steel Plate Experiment

Grid Point No.	Projection with No Cut		Cut H/4 deep		Cut H/2 deep		Cut 3H/4 deep	
	Displacement							
	u	v	u	v	u	v	u	v
1	-52	-114	-59	-118	-34	-108	144	-49
2	33	-119	28	-123	47	-113	196	-53
3	157	-145	154	-147	164	-139	269	-82
4	476	-124	474	-126	477	-121	520	-83
5	-52	11	-59	9	-34	13	145	40
6	41	14	36	11	55	16	203	42
7	174	23	171	21	180	25	282	49
8	425	33	424	31	426	33	466	48
9	-36	114	-44	110	-20	110	162	109
10	40	115	35	111	56	111	208	111
11	144	111	142	109	150	109	259	115
12	308	83	307	82	309	82	346	87
13	-16	170	-31	164	-7	157	178	130
14	24	169	21	163	46	158	211	133
15	80	153	78	149	89	145	217	134
16	160	103	159	101	160	98	188	96
17	0	187	-28	188	-8	183	178	132
18	0	186	0	180	34	173	217	122
19	0	165	0	162	0	143	184	100
20	0	108	0	107	0	98	0	70
4'	1000	0	1000	0	1000	0	1000	0
8'	750	0	750	0	750	0	750	0
12'	500	0	500	0	500	0	500	0

TABLE 4

Displacements in Plate Projections with Cuts (side ratio 1:2)

Constant strain and zero curvature imposed

(Ref. Figure 13)

Grid Point No.	Projection with No Cut Displacement		Cut H/4 deep		Cut H/2 deep		Cut 3H/4 deep	
	u	v	u	v	u	v	u	v
16'	250	0	250	0	250	0	250	0
20'	0	0	0	0	0	0	0	0
g	0	-158	0	-158	0	-154	0	-115
h	315	-159	315	-158	322	-154	326	-143
i	654	-129	655	-128	657	-127	638	-128
j	862	-147	862	-145	865	-146	857	-157
k	1524	124	1526	126	1523	121	1480	83

TABLE 4 (contd.)

Grid Point No.	Projection with No Cut		Cut H/4 deep		Cut H/2 deep		Cut 3H/4 deep	
	u	v	u	v	u	v	u	v
1	88	234	111	247	182	278	301	319
2	51	233	65	245	117	276	214	317
3	40	248	48	257	75	283	140	321
4	47	301	50	306	59	320	85	345
5	87	194	110	199	180	214	300	232
6	55	192	69	199	120	214	216	232
7	47	199	55	204	80	216	142	232
8	47	211	49	214	57	220	80	230
9	73	141	111	147	175	149	270	146
10	46	136	60	143	115	147	214	145
11	39	130	45	134	67	138	133	140
12	33	118	35	120	40	121	61	123
13	42	98	88	106	168	88	293	63
14	26	90	36	98	102	87	210	64
15	21	77	24	80	39	74	117	61
16	17	55	17	56	20	51	35	47
17	0	81	83	63	167	31	292	-15
18	0	72	0	66	90	29	212	-18
19	0	58	0	55	0	34	106	-12
20	0	33	0	32	0	21	0	6
4'	0	400	0	400	0	400	0	400
8'	0	225	0	225	0	225	0	225
12'	0	100	0	100	0	100	0	100

TABLE 5

Displacements in Plate Projections with Cuts (side ratio 1:2)

Constant curvature and zero strain imposed
(Ref. Figure 13)

Grid Point No.	Projection with No Cut		Cut H/4 deep		Cut H/2 deep		Cut 3H/4 deep	
	u	v	u	v	u	v	u	v
16'	0	25	0	25	0	25	0	25
20'	0	0	0	0	0	0	0	0
g	0	-34	0	-34	0	-24	0	- 5
h	-34	-6	-32	-7	-25	-2	-23	7
i	-66	86	-66	87	-62	87	-70	87
j	-153	221	-152	218	-147	215	-148	209
k	-47	499	-50	494	-59	480	-85	455

TABLE 5 (contd.)

Grid Point No.	Projection with No Cut		Cut H/4 deep		Cut H/2 deep		Cut 3H/4 deep	
	Displacement u	v	u	v	u	v	u	v
1	1150	-198	1157	-197	1205	-186	1322	-160
2	912	-240	921	-239	973	-227	1099	-199
3	1291	-290	1298	-288	1337	-276	1428	-247
4	2292	-192	2295	-191	2309	-183	2339	-164
5	1127	94	1134	95	1183	98	1305	104
6	1220	100	1228	101	1274	106	1383	112
7	1478	118	1485	119	1519	122	1599	128
8	1876	90	1881	91	1898	93	1937	97
9	956	245	964	251	1036	255	1210	243
10	1019	214	1032	222	1097	232	1251	229
11	1144	172	1155	179	1201	189	1314	194
12	1313	103	1320	106	1344	112	1401	119
13	539	276	606	307	784	301	1079	228
14	560	230	589	261	731	277	1033	228
15	607	168	621	190	686	210	905	204
16	673	94	679	104	705	112	787	121
17	0	281	349	220	752	132	1046	41
18	0	226	0	223	384	139	1086	12
19	0	164	0	161	0	149	549	28
20	0	90	0	88	0	79	0	72
4'	3000	0	3000	0	3000	0	3000	0
8'	2250	0	2250	0	2250	0	2250	0
12'	1500	0	1500	0	1500	0	1500	0

TABLE 6

Displacements in Plate Projections with Cuts (side ratio 1:6)

Constant strain and zero curvature imposed

(Ref, Figure 13)

Grid Point No.	Projection with No Cut		Cut H/4 deep		Cut H/2 deep		Cut 3H/4 deep	
	Displacement u	v	u	v	u	v	u	v
16'	750	0	750	0	750	0	750	0
20'	0	0	0	0	0	0	0	0
g	0	-107	0	-104	0	-90	0	-66
h	832	-114	828	-124	808	-129	733	-132
i	1691	-130	1682	-133	1656	-139	1599	-151
j	2529	-146	2523	-148	2506	-151	2470	-158
k	3708	192	3705	191	3691	183	3661	164

TABLE 6(contd.)

Grid Point No.	Projection with No Cut		Cut H/4 deep		Cut H/2 deep		Cut 3H/4 deep	
	u	v	u	v	u	v	u	v
1	1219	3398	1230	3399	1267	3407	1328	3421
2	703	3381	711	3382	752	3391	818	3406
3	498	3386	505	3388	536	3397	583	3412
4	394	3469	397	3470	407	3476	423	3486
5	1193	2070	1200	2070	1238	2073	1301	2076
6	826	2066	834	2067	869	2070	926	2074
7	545	2065	552	2066	578	2069	620	2072
8	295	2049	299	2049	313	2051	333	2053
9	928	1004	936	1010	991	1014	1083	1008
10	660	975	671	983	723	991	804	990
11	426	951	436	957	473	966	530	969
12	211	925	217	929	236	934	264	937
13	497	335	558	364	702	363	860	322
14	356	296	383	327	494	344	653	316
15	229	266	242	286	293	304	402	299
16	111	243	117	252	137	260	177	263
17	0	111	319	57	673	-14	828	-75
18	0	68	0	67	289	-2.4	671	-84
19	0	37	0	36	0	29	262	-56
20	0	15	0	14	0	8.4	0	6
4'	0	3600	0	3600	0	3600	0	3600
8'	0	2025	0	2025	0	2025	0	2025
12'	0	900	0	900	0	900	0	900

TABLE 7

Displacements in Plate Projections with Cuts (side ratio 1:6)

Constant curvature and zero strain imposed
(Ref. Figure 13)

Grid Point No.	Projection with No Cut		Cut H/4 deep		Cut H/2 deep		Cut 3H/4 deep	
	u	v	u	v	u	v	u	v
16'	0	225	0	225	0	225	0	225
20'	0	0	0	0	0	0	0	0
g	0	-9	0	-7	0	3	0	14
h	-108	212	-112	204	-128	198	-165	198
i	-209	880	-217	876	-238	871	-265	866
j	-338	2003	-347	2003	-361	2000	-379	1997
k	-394	3731	-397	3730	-407	3724	-423	3714

TABLE 7 (contd.)

Point No.	Half length of opening							
	3B/4		B/2		B/4		B/8	
	u	v	u	v	u	v	u	v
1	157.12	6.92	148.04	8.88	133.51	12.53	121.14	16.95
2	118.13	6.29	100.42	8.63	72.22	13.42	49.79	20.55
3	105.95	10.37	85.35	14.06	53.35	21.25	29.60	30.50
4	100.36	14.72	78.97	19.39	47.45	27.62	26.03	36.77
5	95.70	18.72	73.60	24.14	42.50	33.21	22.67	42.67
6	157.01	-1.91	148.02	-2.17	134.23	-2.33	123.99	-1.79
7	145.29	-0.98	133.68	-0.90	115.79	-0.24	102.49	1.52
8	137.20	2.35	123.70	3.28	103.05	5.52	87.86	8.87
9	131.94	5.98	117.22	7.77	95.05	11.43	79.04	15.97
10	128.73	9.56	113.16	12.11	89.92	16.86	73.12	22.11
11	167.57	-0.36	160.80	-0.42	150.55	-0.42	143.25	-0.22
12	164.18	0.38	152.61	0.50	145.14	0.87	136.89	1.51
13	160.70	2.31	153.31	2.85	139.57	3.97	130.31	5.29
14	157.92	4.93	148.82	6.05	135.02	8.08	124.88	10.13
15	156.37	7.91	146.83	9.68	132.28	12.67	121.35	15.39
16	183.26	0.41	179.75	0.48	174.47	0.62	170.75	0.74
17	182.36	1.20	178.63	1.43	173.01	1.83	169.00	2.16
18	181.21	2.55	177.20	3.07	171.13	3.91	166.74	4.58
19	180.01	4.46	175.71	5.39	169.15	6.86	164.32	8.00
20	178.74	6.88	174.13	8.34	167.06	10.60	161.74	12.34
21	0	33.13	0	31.48	0	29.63	0	33.04
22	0	35.23	0	34.01	0	32.77	0	36.50

TABLE 8

Displacements in Plates with Openings

Case 1 Single Opening

(Ref. Page 109)

Point No.	Half length of opening							
	3B/4		B/2		B/4		B/8	
	u	v	u	v	u	v	u	v
23	0	37.27	0	36.44	0	35.71	0	39.70
24	0	39.25	0	38.76	0	38.48	0	42.47
25	0	41.17	0	40.99	0	41.08	0	45.47
26	26.60	31.75	21.44	30.47	13.44	29.21	7.54	33.01
27	25.87	33.85	20.62	32.99	12.68	32.32	15.02	32.86
28	25.13	35.89	19.80	35.41	11.93	35.23	13.93	35.96
29	24.40	37.88	18.98	37.74	11.20	37.99	6.10	42.47
30	23.66	39.80	18.15	39.97	10.44	40.60	5.60	45.30
31	53.20	27.65	42.87	27.45	26.87	27.99	15.02	32.86
32	51.73	29.73	41.22	29.93	25.28	30.96	13.93	35.96
33	50.27	31.76	39.59	32.32	23.82	33.78	13.05	38.97
34	48.79	33.74	37.95	34.63	22.41	36.50	12.20	41.93
35	47.31	35.66	36.29	36.86	20.92	39.12	11.23	44.78
36	79.72	20.85	64.21	22.42	40.16	25.74	22.34	32.25
37	77.49	22.83	61.67	24.75	37.71	28.52	20.77	35.12
38	75.34	24.78	59.29	27.04	35.63	31.25	19.54	38.07
39	73.22	26.72	56.98	29.30	33.67	33.96	18.33	41.03
40	71.05	28.65	54.58	31.55	31.55	36.61	16.90	43.90
41	102.97	12.61	81.92	16.83	50.06	24.59	27.58	33.71
42	97.98	16.75	76.27	21.81	45.05	30.48	24.49	39.77
43	109.40	7.93	89.56	10.97	58.12	17.29	33.60	26.50
44	82.07	18.81	67.00	19.98	43.17	22.84	24.76	29.42

TABLE 8 (contd.)

Point No.	Half length of opening							
	3B/4		B/2		B/4		B/8	
	u	v	u	v	u	v	u	v
45	54.65	25.50	44.49	24.84	28.44	24.73	16.15	29.40
46	27.33	29.60	22.24	27.84	14.16	25.88	7.97	29.17
47	0	30.97	0	28.86	0	26.30	0	29.14
48	183.61	0	180.18	0	175.03	0	171.42	0
49	169.04	0	162.59	0	152.86	0	145.97	0
50	162.74	0	155.01	0	143.21	0	134.46	0
51	175.59	0	170.44	0	162.31	0	154.78	0
52	140.79	0.60	128.13	1.09	108.68	2.52	94.24	5.12
53	162.41	1.23	154.42	1.54	142.31	2.25	133.55	3.21
54	181.81	1.80	177.94	2.16	172.11	2.75	167.91	3.24
c	216.88	0	220.48	0	225.89	0	229.74	0
d	216.56	1.02	220.09	1.3	225.41	1.75	229.20	2.17
e	216.86	0.76	220.46	1.04	225.90	1.52	229.82	2.05
f	217.48	-.66	221.23	-.67	226.89	-.60	230.99	-.33
g	216.21	1.24	219.68	1.65	224.95	2.34	228.81	3.12
h	217.78	-2.32	221.61	-2.66	227.45	-3.08	231.78	-3.07
i	215.58	0.14	218.95	.31	224.14	0.69	228.07	1.28

TABLE 8(contd.)

Point No.	Half Length of opening=B/4 u	v	Point No.	Half Length of opening=B/4 u	v	Point No.	Half Length of opening=B/4 u	v
1	165.85	23.17	22	0	64.20	43	84.41	40.34
2	114.03	37.86	23	0	67.56	44	-	-
3	65.84	44.23	24	0	70.56	45	-	-
4	52.33	51.57	25	0	73.20	46	-	-
5	41.72	57.57	26	16.17	59.56	47	-	-
6	160.10	-.66	27	14.72	63.29	48	181.99	0
7	139.21	1.24	28	13.23	66.63	49	168.88	0
8	117.36	6.72	29	11.73	69.62	50	168.27	0
9	102.70	13.42	30	10.22	72.26	51	183.20	0
10	91.96	19.28	31	32.43	56.99	52	127.55	3.57
11	166.05	-1.71	32	29.42	60.63	53	154.33	-1.08
12	158.72	-1.85	33	26.41	63.83	54	177.69	0.18
13	149.93	.22	34	23.46	66.75	c	221.60	0
14	142.44	3.89	35	20.44	69.41	d	221.18	3.90
15	137.64	8.40	36	49.10	52.88	e	221.58	5.50
16	181.19	-.51	37	43.93	56.04	f	222.42	4.30
17	179.04	-.32	38	39.42	58.96	g	220.72	6.94
18	176.26	.99	39	35.21	61.77	h	222.94	1.83
19	173.58	3.45	40	30.82	64.47	i	220.56	4.27
20	171.54	6.88	41	58.17	48.22			
21	0	60.47	42	47.12	54.60			

TABLE 9

Displacements in Plates with Openings

Single Opening (60 °/o)

(Ref. Page 109)

Point No.	Half distance between openings							
	B		3B/4		B/2		B/4	
	u	v	u	v	u	v	u	v
1	- 58.51	7.39	- 44.14	8.42	- 23.08	9.64	- 1.88	6.58
2	-108.71	4.83	- 89.71	6.37	- 62.87	8.94	- 26.44	8.48
3	-119.41	9.08	-104.90	11.19	- 85.42	13.61	- 57.55	10.47
4	-121.06	13.68	-108.20	16.40	- 91.15	19.32	- 64.58	16.61
5	-121.61	18.04	-109.68	21.34	- 94.23	25.00	- 68.50	23.93
6	- 57.87	-2.42	- 43.34	-1.98	- 22.84	-1.09	- 2.18	-.13
7	- 71.94	-1.01	- 60.61	-.38	- 43.89	0.41	- 20.11	0.05
8	- 80.05	3.44	- 71.17	4.71	- 58.94	5.98	- 41.25	4.37
9	- 84.16	7.96	- 76.48	10.05	- 66.06	12.41	- 48.14	12.02
10	- 86.12	12.14	- 79.30	14.93	- 70.37	18.28	- 52.36	19.82
11	- 43.55	0.04	- 33.00	-0.68	- 17.69	-2.04	- 1.90	-3.16
12	- 47.23	1.44	- 39.26	0.57	- 28.06	-1.36	- 13.40	-4.00
13	- 50.56	4.17	- 44.72	3.81	- 37.03	2.52	- 26.52	0.28
14	- 52.80	7.52	- 48.35	7.90	- 42.62	7.82	- 31.85	7.87
15	- 53.63	11.10	- 50.11	12.24	- 46.07	13.40	- 35.42	15.79
16	- 22.95	1.59	- 17.60	0.67	- 9.55	-1.64	- 1.09	-4.44
17	- 23.85	3.59	- 19.66	2.21	- 13.81	-1.33	- 6.67	-5.86
18	- 24.84	6.12	- 21.80	4.87	- 17.93	1.47	- 12.96	-2.05
19	- 25.54	9.08	- 23.39	8.36	- 20.85	5.96	- 15.84	5.14
20	- 25.62	12.28	- 24.00	12.32	- 22.59	11.31	- 17.87	13.04
21	0	2.05	0	1.13	0	-1.42	0	-4.79
22	0	4.32	0	2.86	0	-1.18	0	-6.40

TABLE 10

Displacements in Plates with Openings

Case 2 Two Openings

(Ref. Page 109)

Point No.	Half distance between openings							
	B		3B/4		B/2		B/4	
	u	v	u	v	u	v	u	v
23	0	6.91	0	5.46	0	1.30	0	-2.80
24	0	9.81	0	8.81	0	5.54	0	4.21
25	0	12.9	0	12.64	0	10.81	0	12.10
26	-181.90	0.05	-178.89	0.59	-174.84	1.33	-168.10	.47
27	-181.41	2.11	-178.27	3.00	-174.06	4.23	-167.50	4.10
28	-180.77	4.13	-177.50	5.37	-173.14	7.06	-166.68	7.63
29	-179.75	6.23	-176.26	7.82	-171.63	9.96	-165.18	11.23
30	-177.89	8.55	-173.96	10.52	-168.76	13.17	-162.11	15.17
31	-161.93	4.12	-155.40	5.91	-146.58	8.30	-132.61	7.18
32	-161.16	6.57	-154.54	8.79	-145.66	11.76	-132.01	11.50
33	-160.40	9.01	-153.72	11.63	-144.83	15.13	-131.49	15.69
34	-159.38	11.43	-152.57	14.44	-143.57	18.45	-130.48	19.82
35	-157.88	13.82	-150.77	17.20	-141.44	21.69	-128.52	23.84
36	-140.93	8.39	-130.48	11.11	-116.35	14.64	- 95.03	13.18
37	-140.71	10.66	-130.55	13.74	-116.93	17.71	- 96.30	16.82
38	-140.46	12.92	-130.55	16.32	-117.38	20.69	- 97.29	20.43
39	-140.02	15.17	-130.29	18.89	-117.48	23.66	- 97.88	24.14
40	-139.33	17.40	-129.67	21.42	-117.10	26.60	- 98.06	27.86
41	-120.45	11.43	-106.92	13.85	- 88.91	16.49	- 62.19	13.35
42	-121.41	15.88	-109.04	18.89	- 92.79	22.16	- 66.51	20.19
43	-117.76	6.49	-101.73	8.22	- 79.94	10.46	- 49.73	7.85
44	-141.40	6.01	-130.76	8.28	-116.28	11.24	- 94.32	9.08

TABLE 10 (contd.)

Point No.	Half distance between openings							
	B		3B/4		B/2		B/4	
	u	v	u	v	u	v	u	v
45	-163.09	1.64	-156.81	2.97	-148.30	4.72	-134.12	2.69
46	-182.33	-2.10	-179.52	-1.94	-175.72	-1.71	-168.71	-3.38
47	0	0	0	0	0	0	0	0
48	- 22.57	0	- 16.73	0	- 7.79	0	0.63	0
49	- 41.89	0	- 30.22	0	- 13.42	0	1.41	0
50	- 50.68	0	- 35.26	0	- 14.59	0	2.21	0
51	- 33.98	0	- 25.96	0	- 11.50	0	2.23	0
52	- 76.69	1.14	- 66.83	2.03	- 52.94	2.90	-33.97	1.32
53	- 48.98	2.69	- 42.17	2.02	- 32.97	.28	-21.34	-2.69
54	- 24.36	4.69	- 20.76	3.26	- 15.97	-.50	-10.32	-5.46
55	0	5.57	0	4.05	0	-.22	0	-5.43
c	-214.44	2.81	-216.79	3.31	-219.97	3.89	-225.51	3.85
d	-215.42	2.88	-217.86	3.13	-221.14	3.38	-227.03	3.79
e	-216.04	0.42	-218.75	0.26	-222.36	-.07	-227.96	-.65
f	-216.47	0.69	-219.28	.57	-223.02	.29	-228.58	-.22
g	-218.54	-2.25	-221.85	-2.87	-226.25	-3.81	-232.03	-5.19
h	-217.03	0.89	-220.00	1.06	-223.94	1.19	-229.20	0.45

TABLE 10(contd.)

LIST OF FIGURES

18. Experimental and theoretical longitudinal strain for 1:4 plate with a cut (Constant strain and zero curvature imposed along the base)

19. Variation of "Point-Forces" at the end of the projection and at the root of a central cut, due to the depth of the cut (Side ratio of the projection = 1:4)

20. Stages of grading of net

21. Effect of grading of net on displacements (u and v) for 1:2 plate

22. Effect of grading of net on u, v and $\frac{\delta v}{\delta y}$ along the free edge of the plate

23. Effect of grading of net on longitudinal stress σx (1:2 plate)

24. Effect of grading of net on transverse stress σy (1:2 plate)

25. Effect of grading of net on shear stress τxy (1:2 plate)

26. Possible method of grading a net around a straight cut

27. The Loading Frame and Polariscope

28. Variation of stress concentration with corner radius (Photoelastic Tests)

29. Variation of stress concentration with length of opening (Photoelastic Tests)

30. Variation of stress concentration with width of opening (Photoelastic Tests)

31. Effect of thickness/radius ratio on stress concentration in circular holes

32. The Steel Specimen and the distribution of longitudinal stress at its centre

33. Test Arrangement (Steel Specimen (Hatch Openings))

34. Variation of Stress Concentration with radius/width ratio

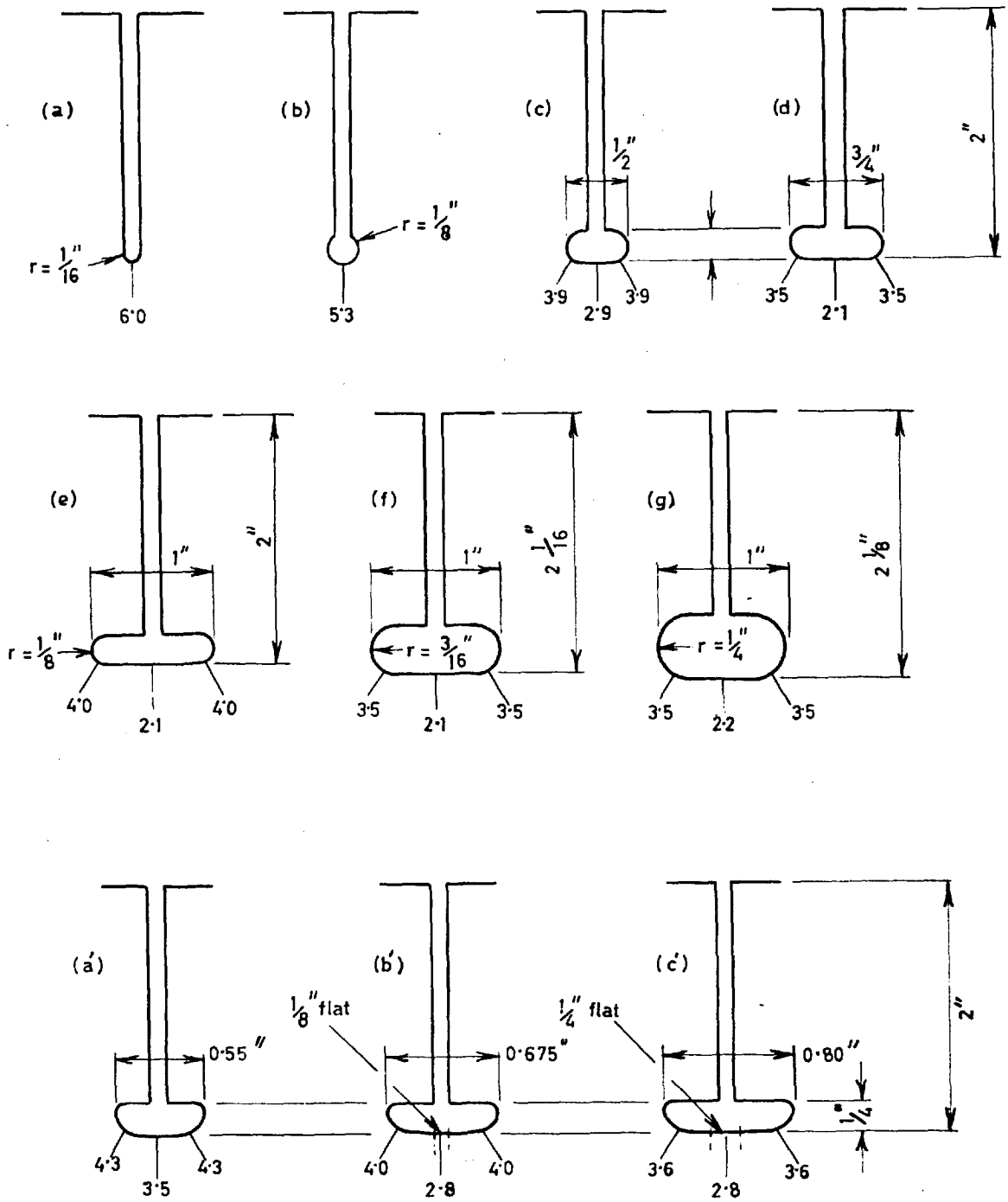

Figure.1. Stress Concentration factors for anchor-shaped Cut-outs.[11]

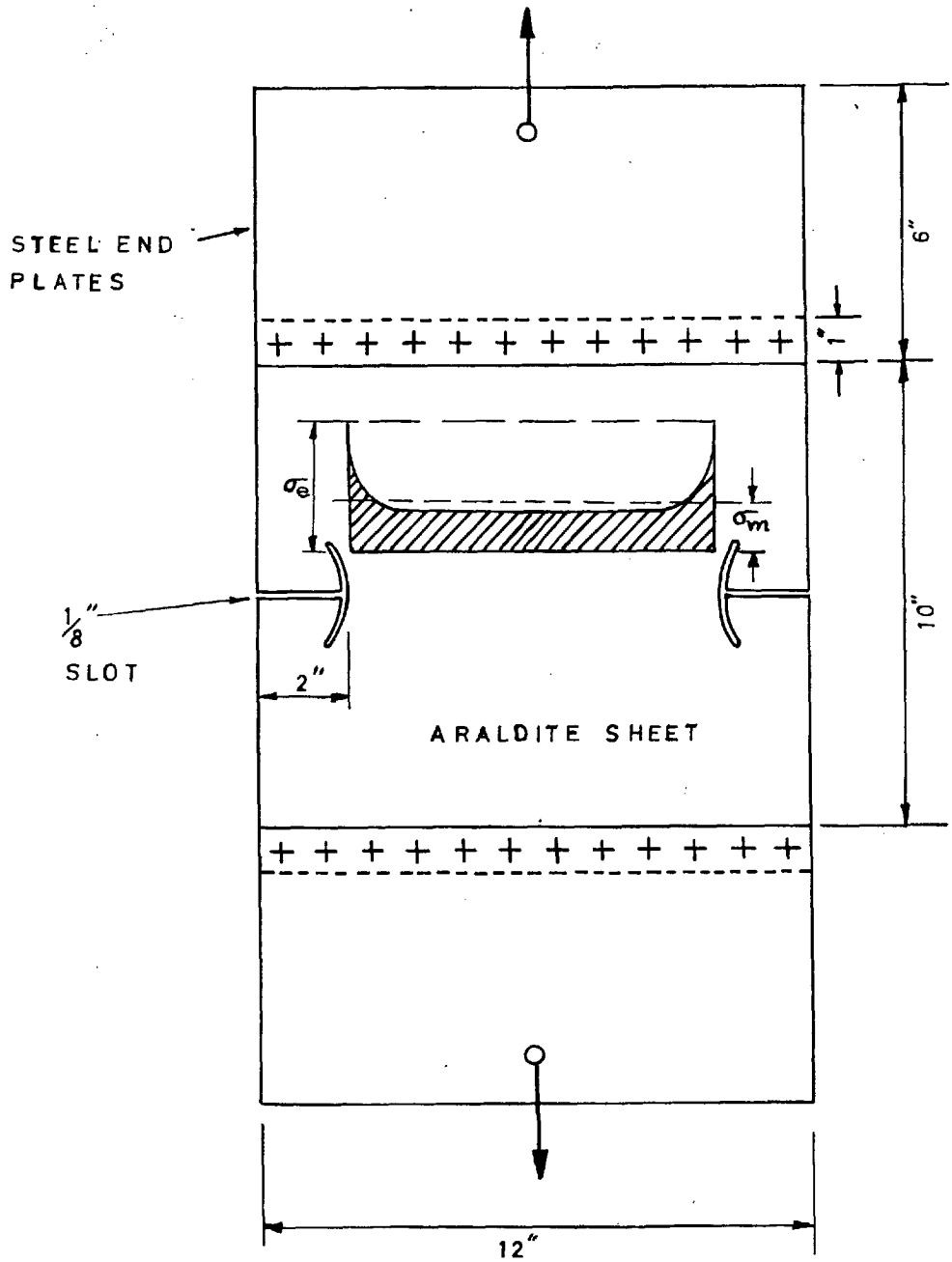

Figure.2. Photoelastic Test-Specimen
(Superstructure Expansion-joint Cut-out)

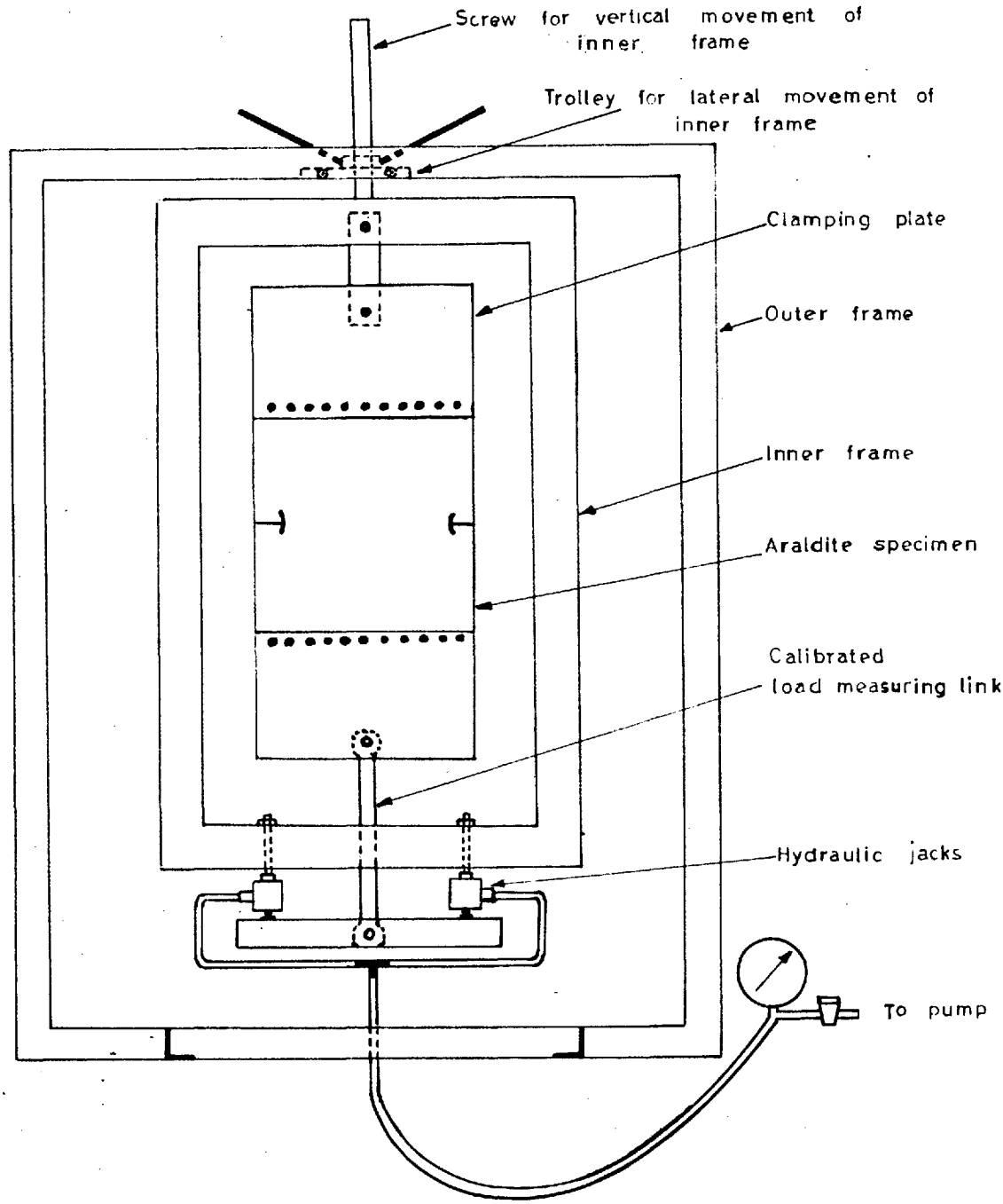

Figure. 3. Loading Frame for Photoelastic specimens

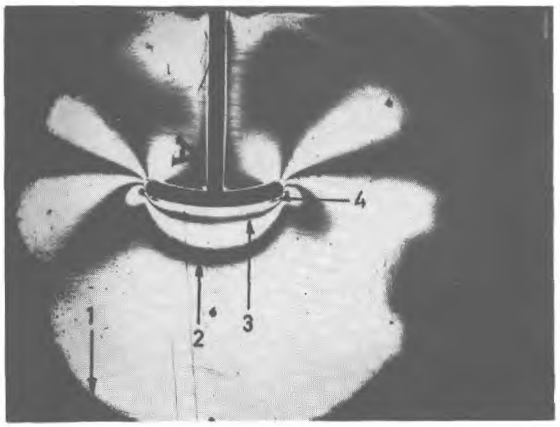

1(a) (σ_N = 389 p.s.i.)

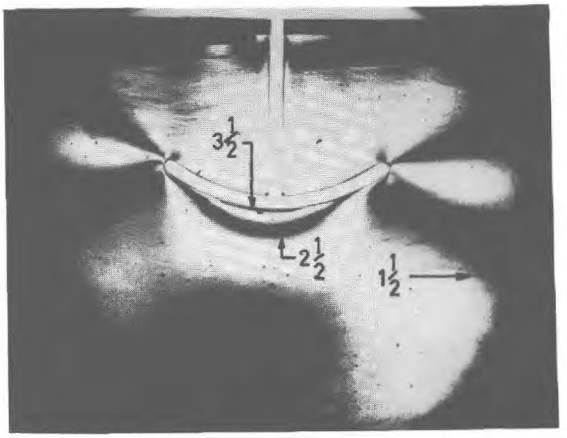

1(b) (σ_N = 412 p.s.i.)

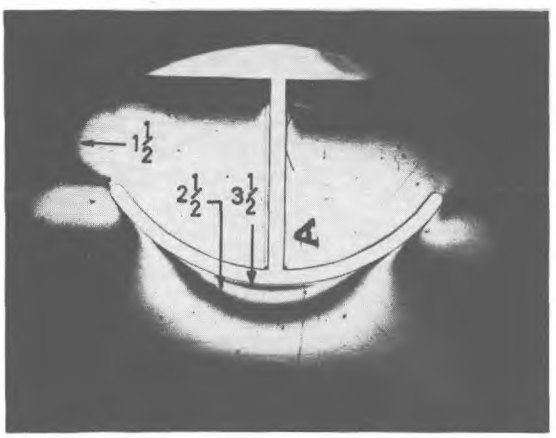

1(c) (σ_N = 412 p.s.i.)

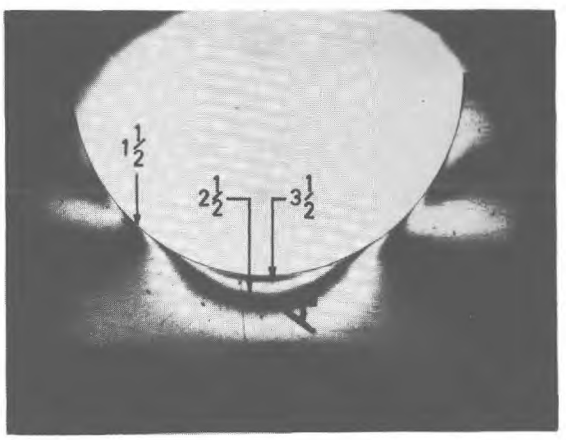

1(d) (σ_N = 412 p.s.i.)

Figure 4. Typical Fringe Patterns

(Specimen 1, Plate thickness 1/4")

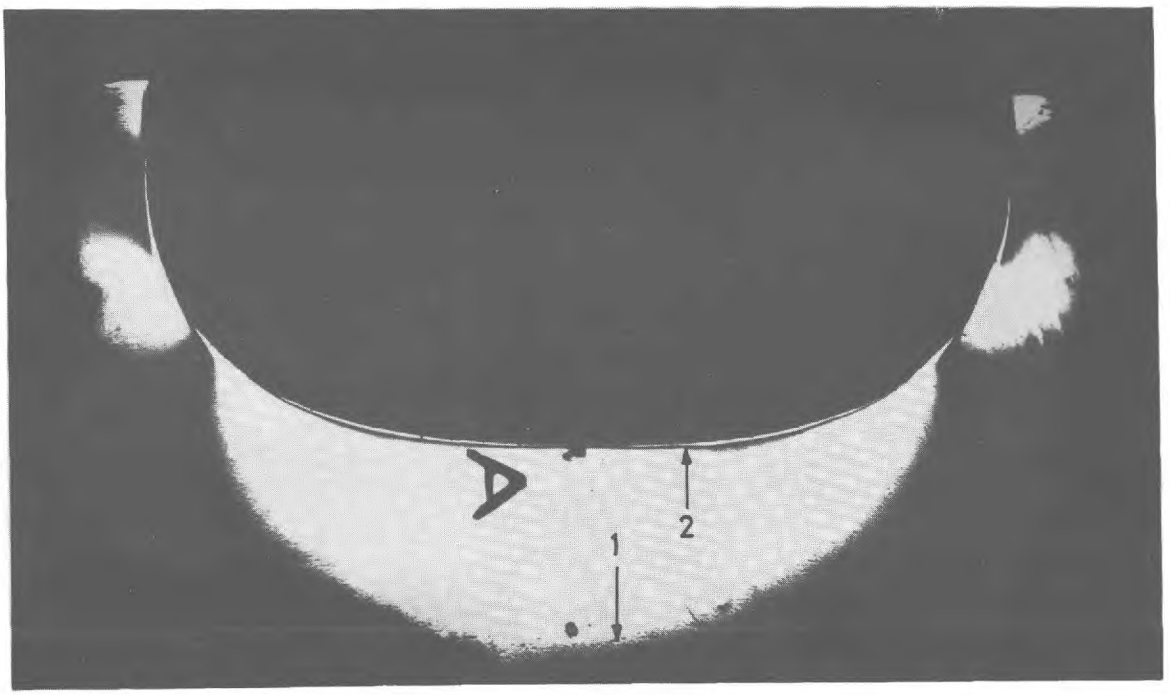

Figure 5. Fringe Pattern for Highway Transition Curve cut-out

(Specimen 2, σ_N = 520 p.s.i. Plate thickness 1/8")

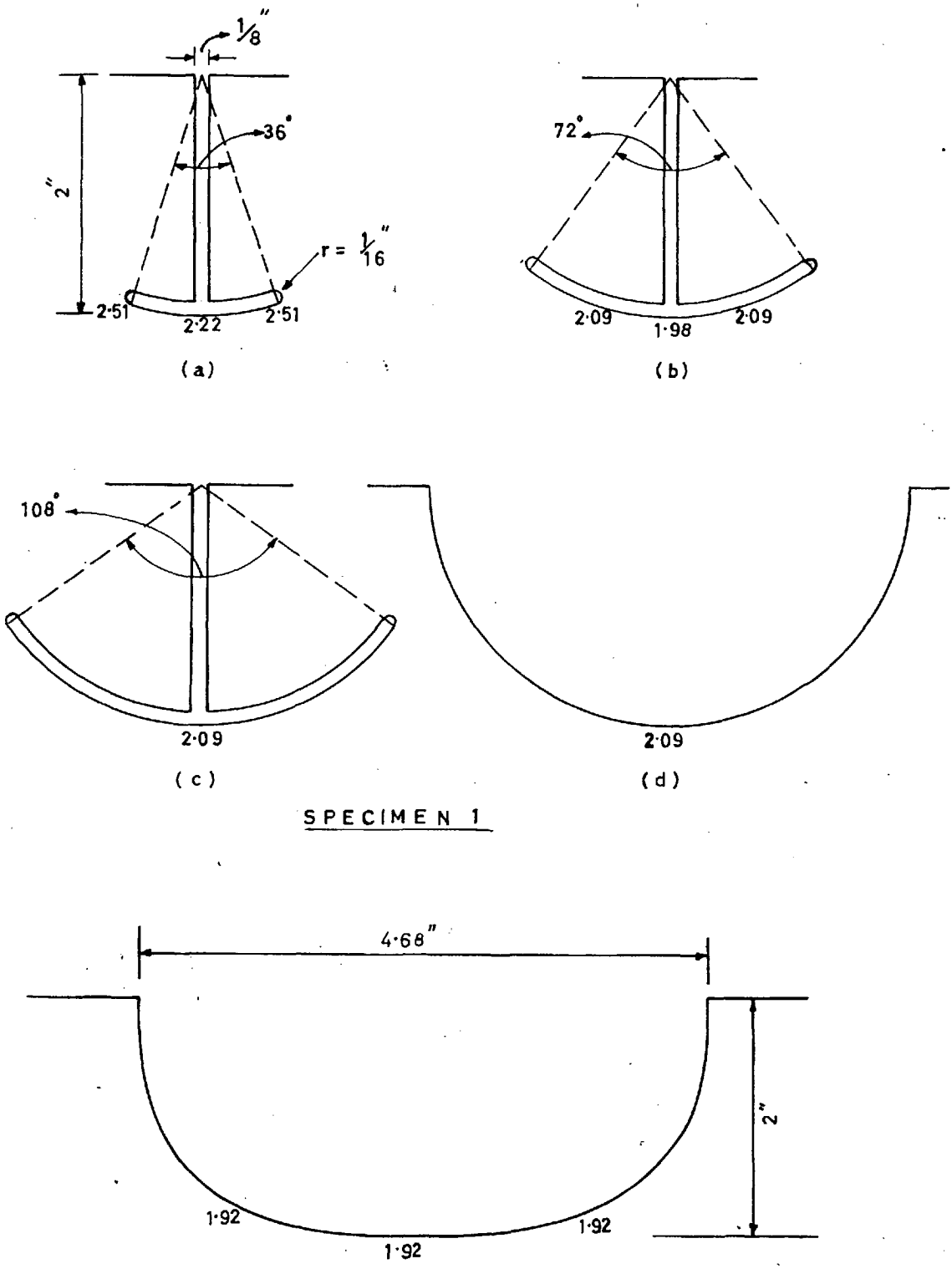

Figure. 6 . Successive shapes and stress concentration factors $\frac{\sigma e}{\sigma_N}$

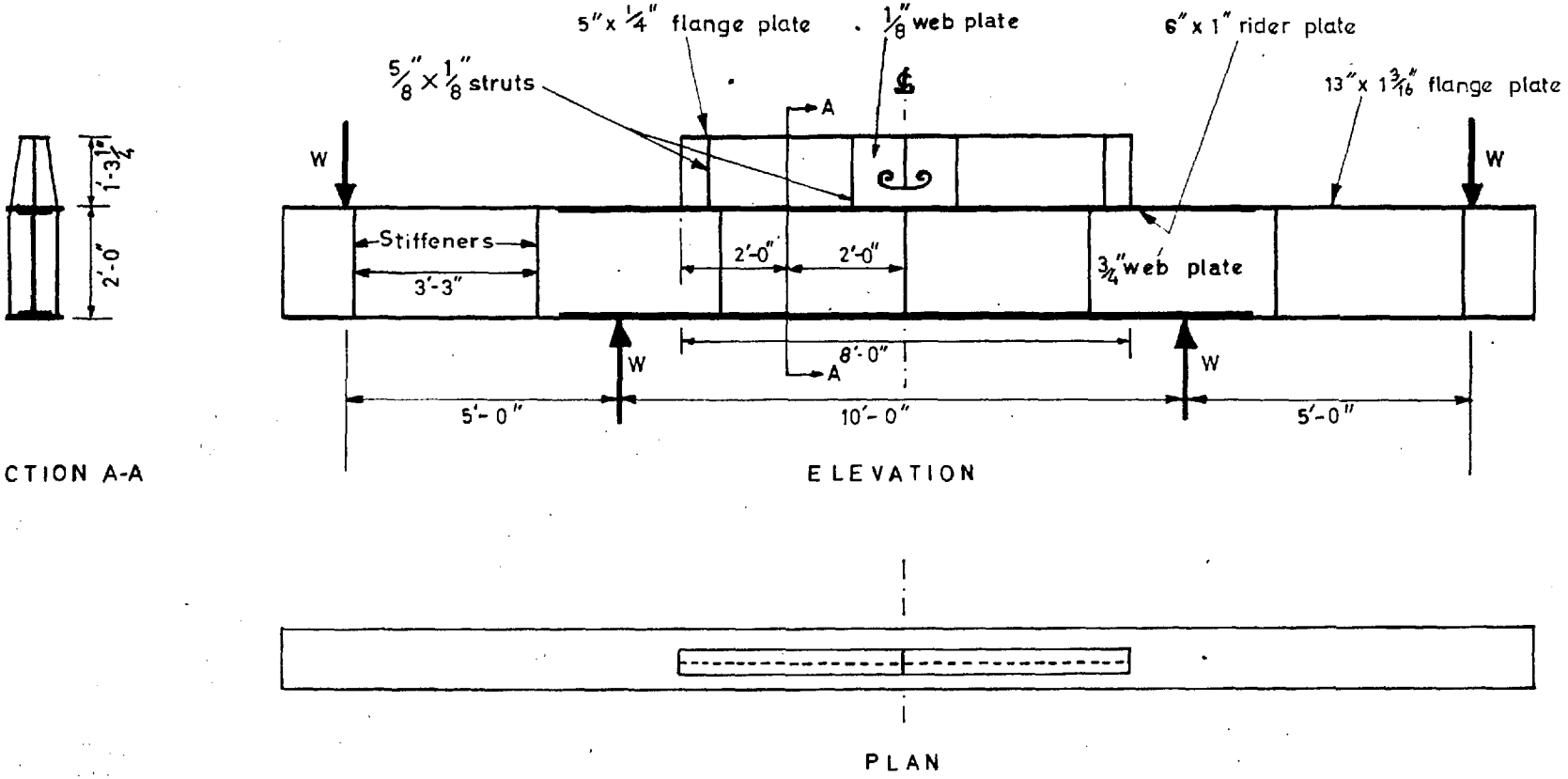

Figure.7. Specimen 3 (Mild steel).

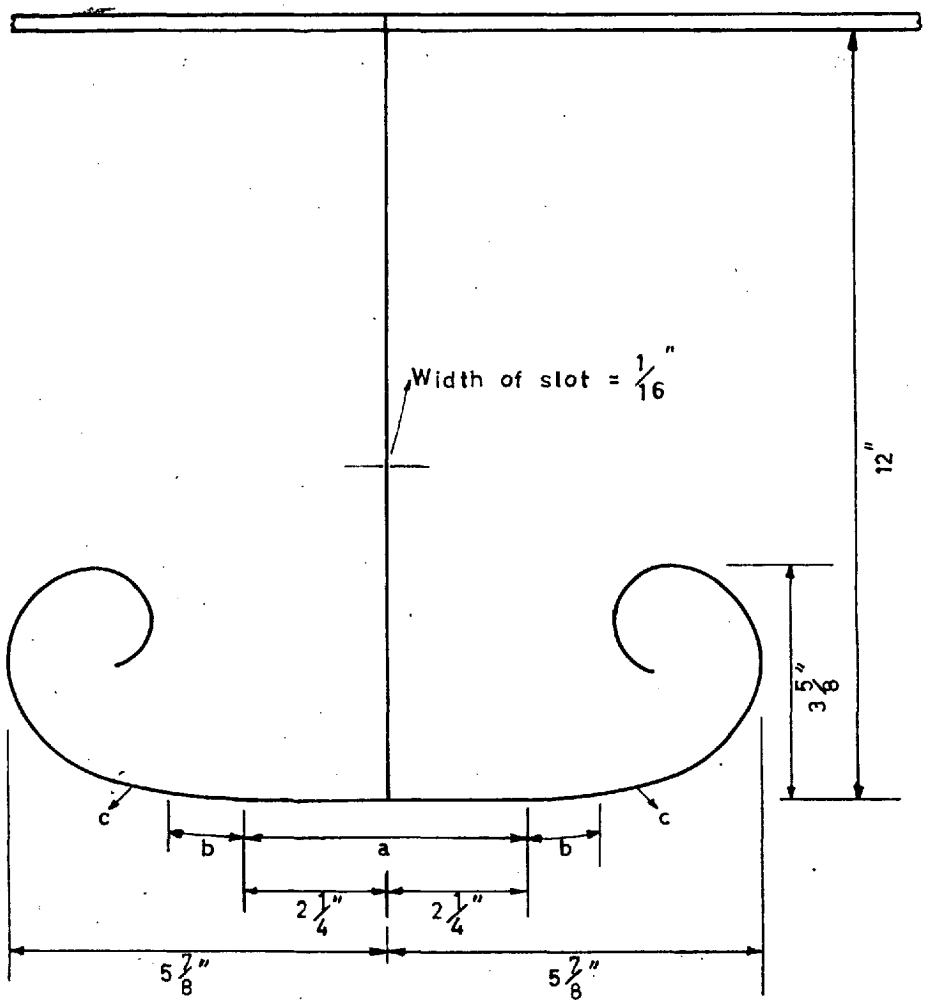

Symbol	Name of Curve	Property
a	Straight	Zero Curvature
b	Highway Transition Curve	Curvature Proportional to Length of Curve
c	Hyperbolic Spiral	Curvature = $a^3 / r(a^2+r^2)^{3/2}$ r = radius vector, a = constant

Figure.8. Shape of cut-out used for Specimen 3

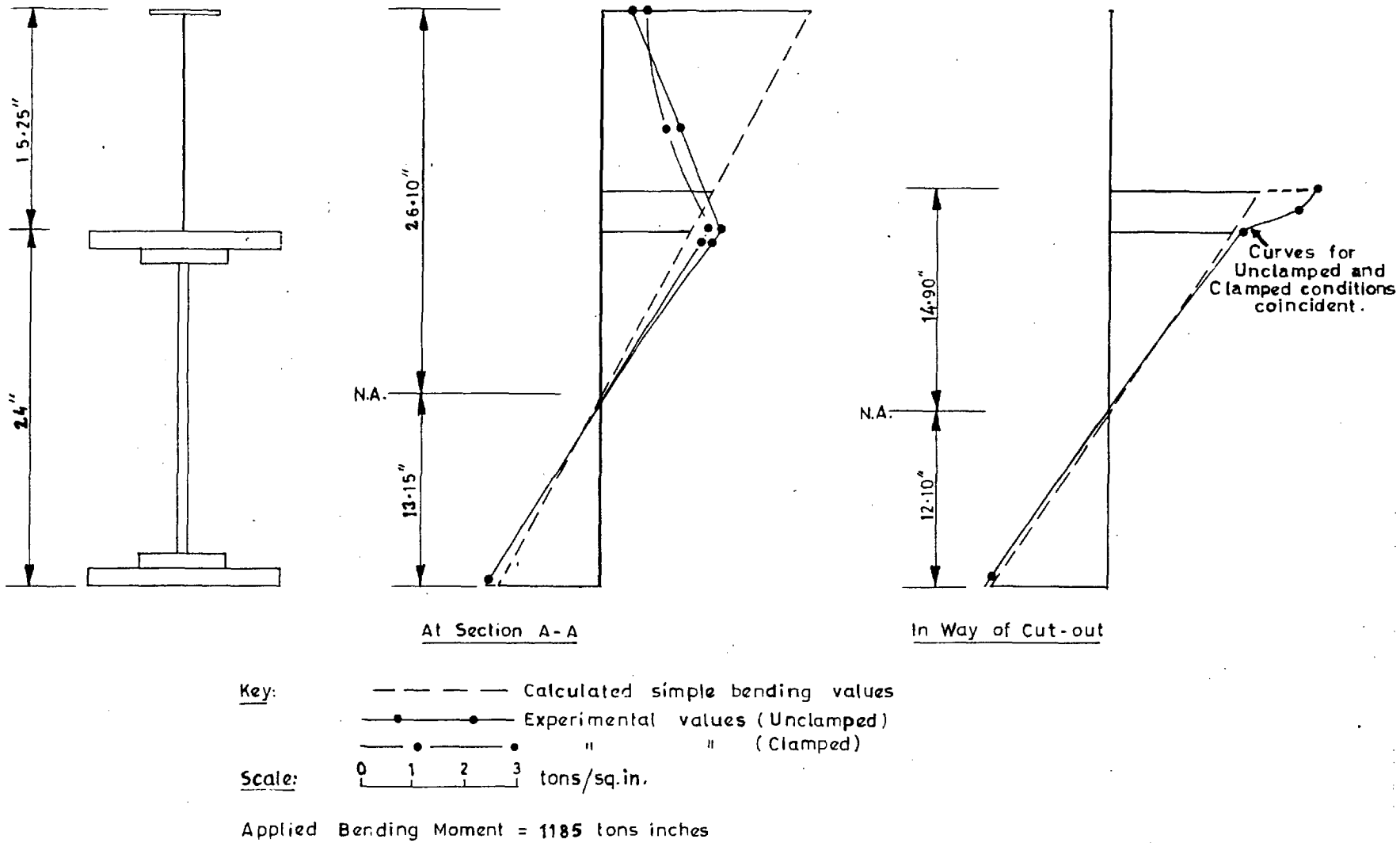

Figure. 9. Effect of vertical restraint on the distribution of longitudinal stress associated with a modified anchor cut-out

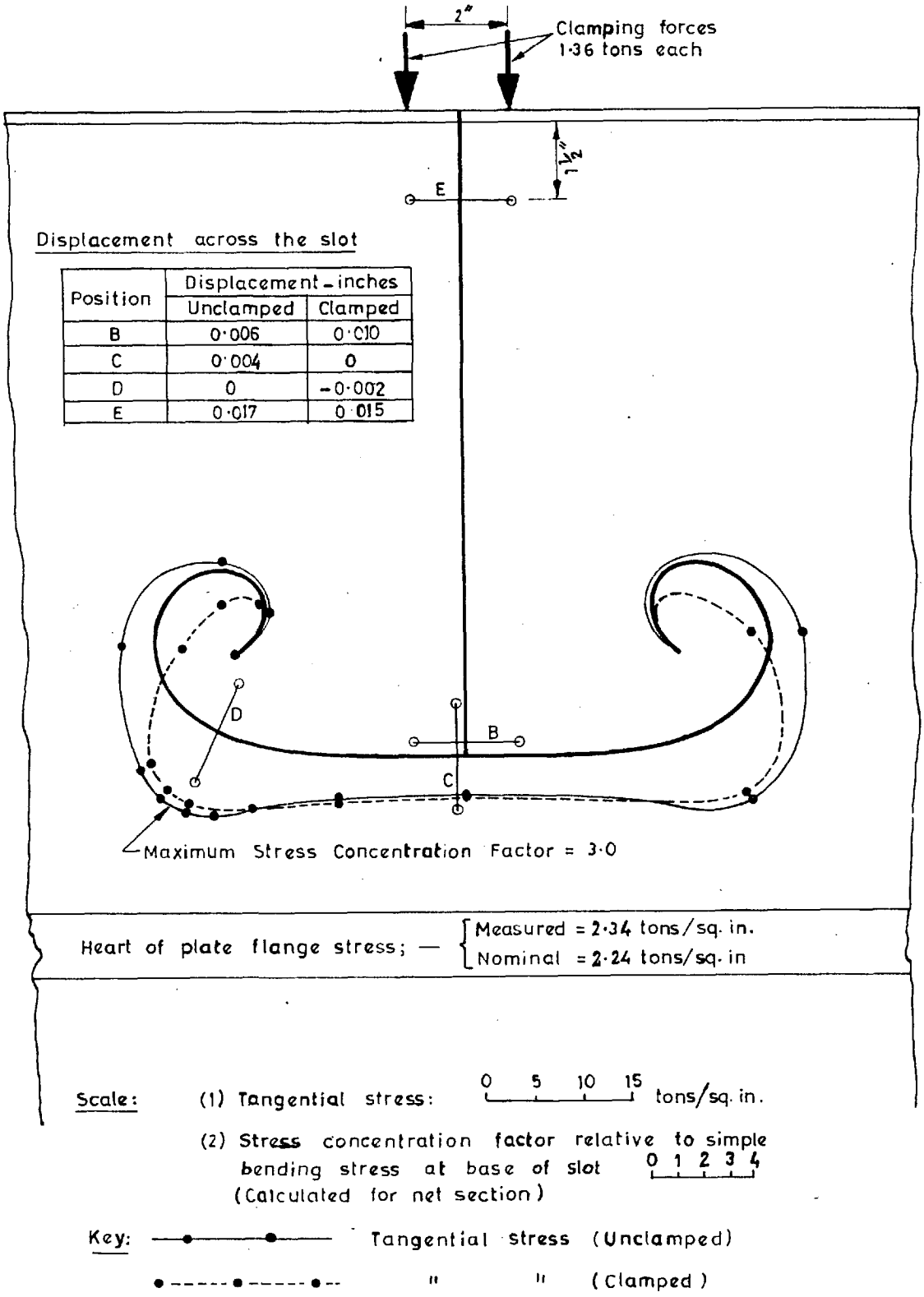

Figure.10. Effect of vertical restraint on displacements and tangential stress distribution around modified anchor cut-out.

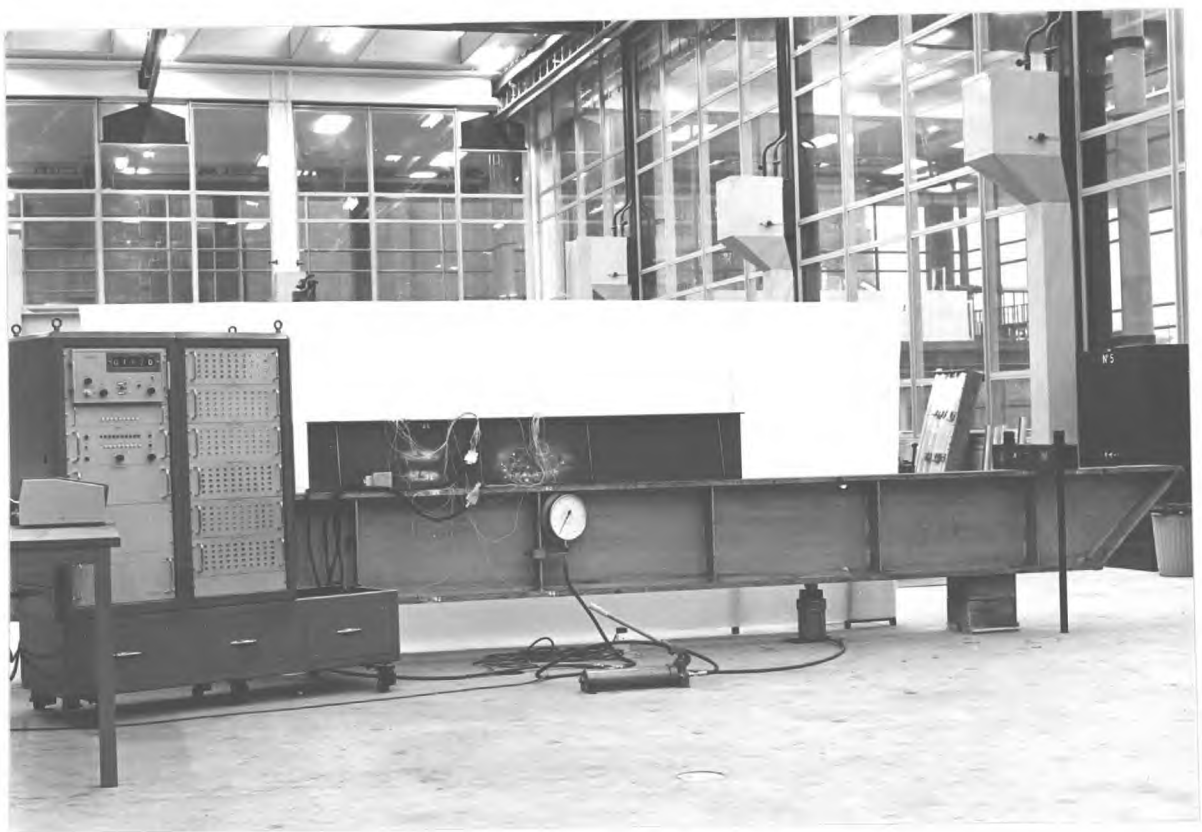

Figure 11 Specimen 3

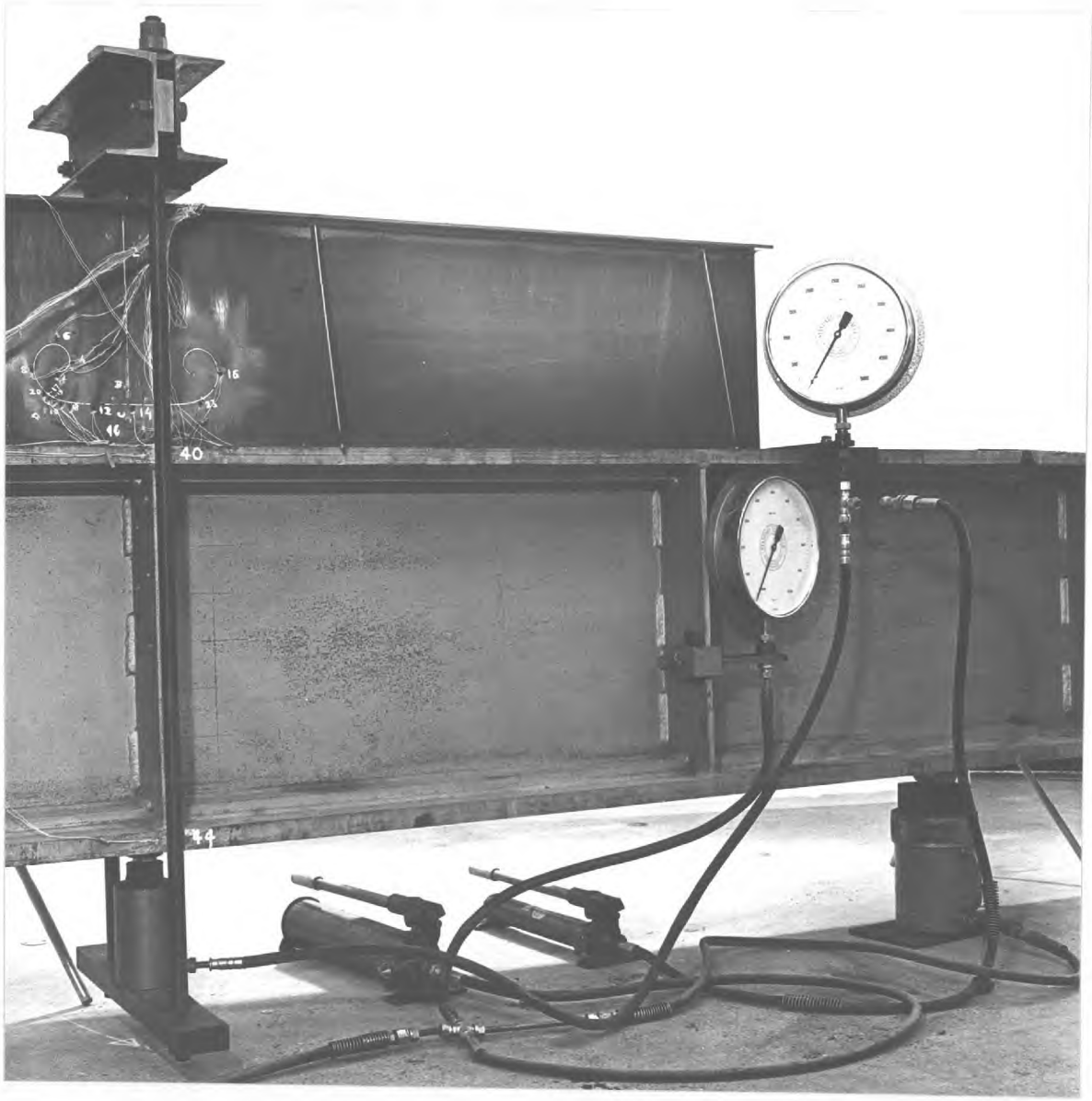

Figure 12 Vertical restraining forces applied to the projection (Specimen 3)

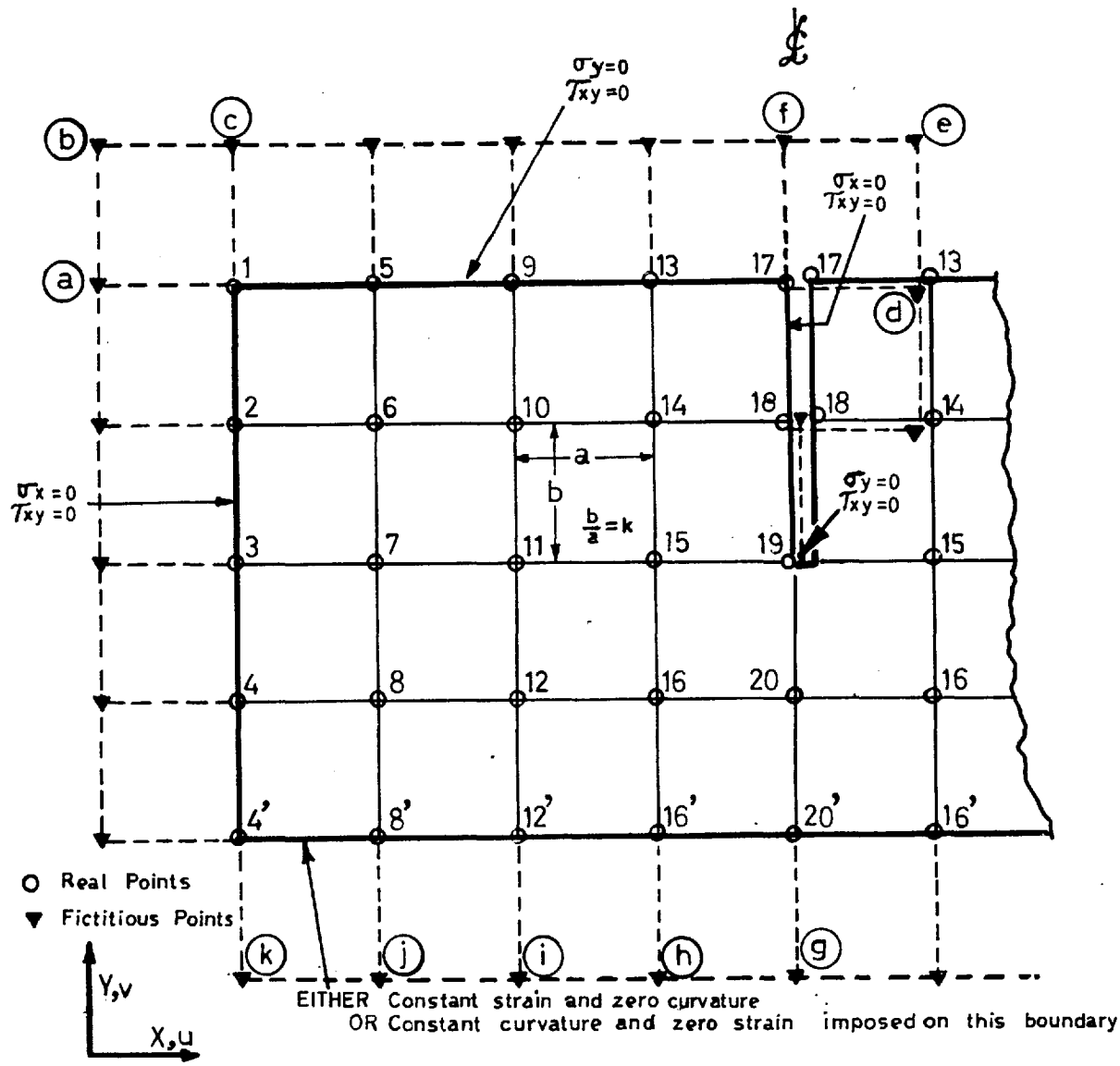

EXTRAPOLATIONS

Displacement	Type of Extrapolation
u_b	Parabolic Continuation of u_{11}, u_6, u_1
v_b	—»— v_{11}, v_6, v_1
u_e	—»— u_{11}, u_{14}, u_{17}
v_e	—»— v_{11}, v_{14}, v_{17}
u_c	$=0{\cdot}5(u_{c_1}+u_{c_2})$ $= 0{\cdot}5\left[3u_1-2u_2+u_3-k(4v_5-v_9-3v_1)\right]$
v_a	$=0{\cdot}5(v_{a_1}+v_{a_2})$ $= 0{\cdot}5\left[3v_1-2v_5+v_9+\frac{1}{k}(3u_1-4u_2+u_3)\right]$

Displacement	Type of Extrapolation
u_{c_1}	Parabolic Continuation of u_3, u_2, u_1
u_{c_2}	Obtained by solving stress condition $\tau_{xy}=0$ at corner using v_{a_1}
v_{a_1}	Parabolic Continuation of v_3, v_2, v_1
v_{a_2}	Obtained by solving stress condition $\tau_{xy}=0$ at corner using u_{c_1}
u_f	$=0{\cdot}5(u_{f_1}+u_{f_2})$; u_{f_1} and u_{f_2} calculated on the same basis as u_{c_1}, u_{c_2}
v_d	$=0{\cdot}5(v_{d_1}+v_{d_2})$; v_{d_1} and v_{d_2} calculated on the same basis as v_{a_1}, v_{a_2}

Figure.13. The finite-difference net showing boundary conditions and extrapolations. (Plate Projections)

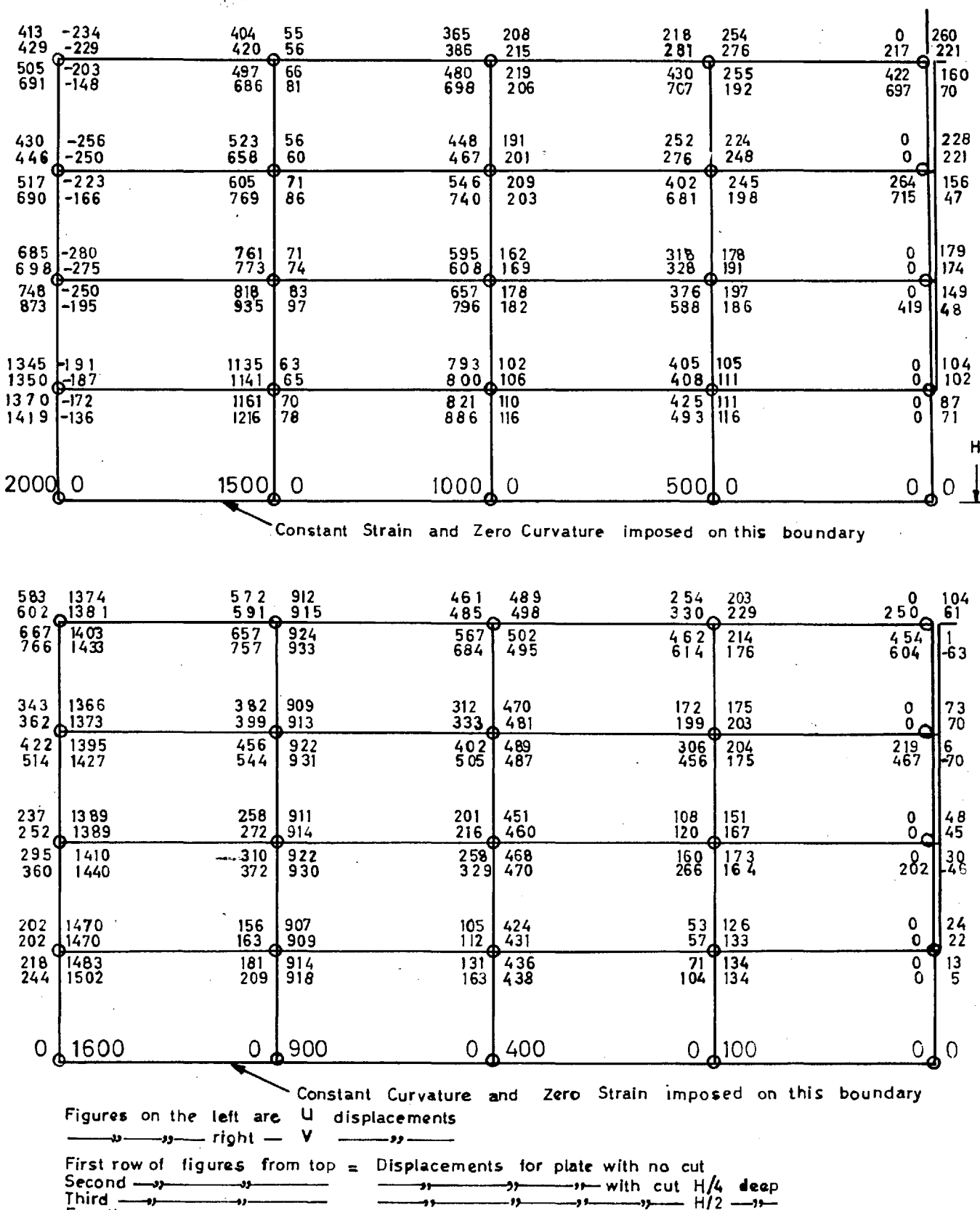

Figure.14. Effect of depth of cut on displacements (1:4 plate)

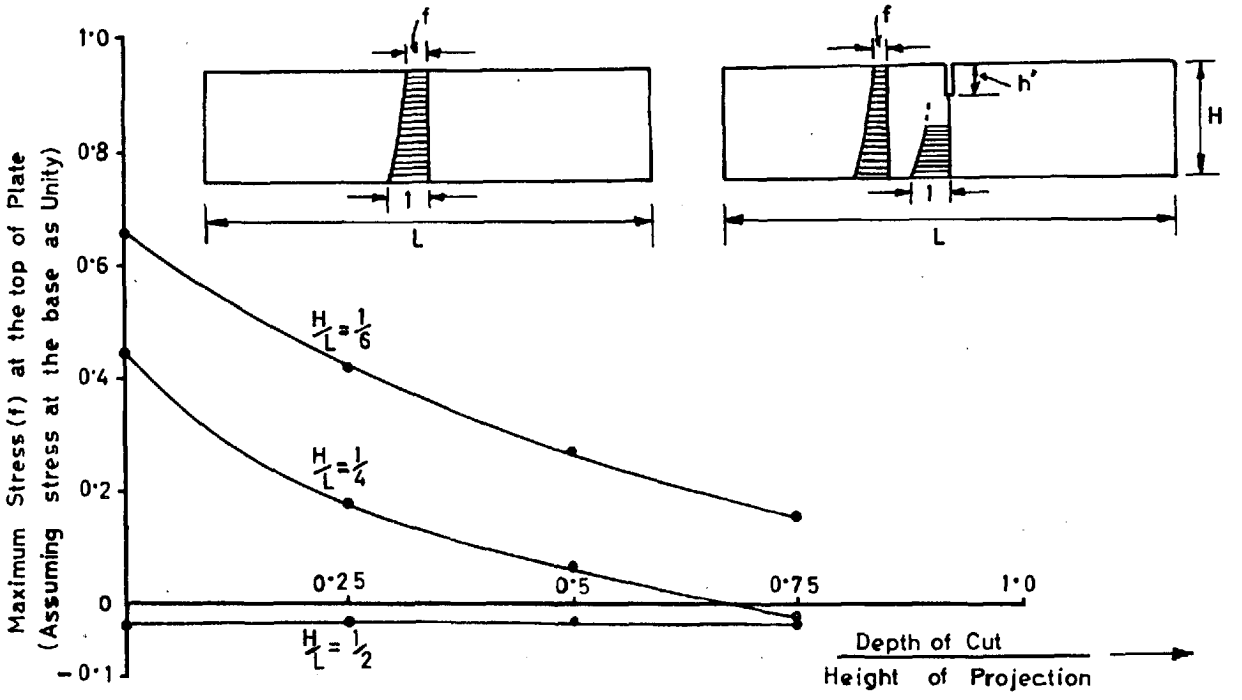

(a) Constant Strain and zero Curvature imposed along the base

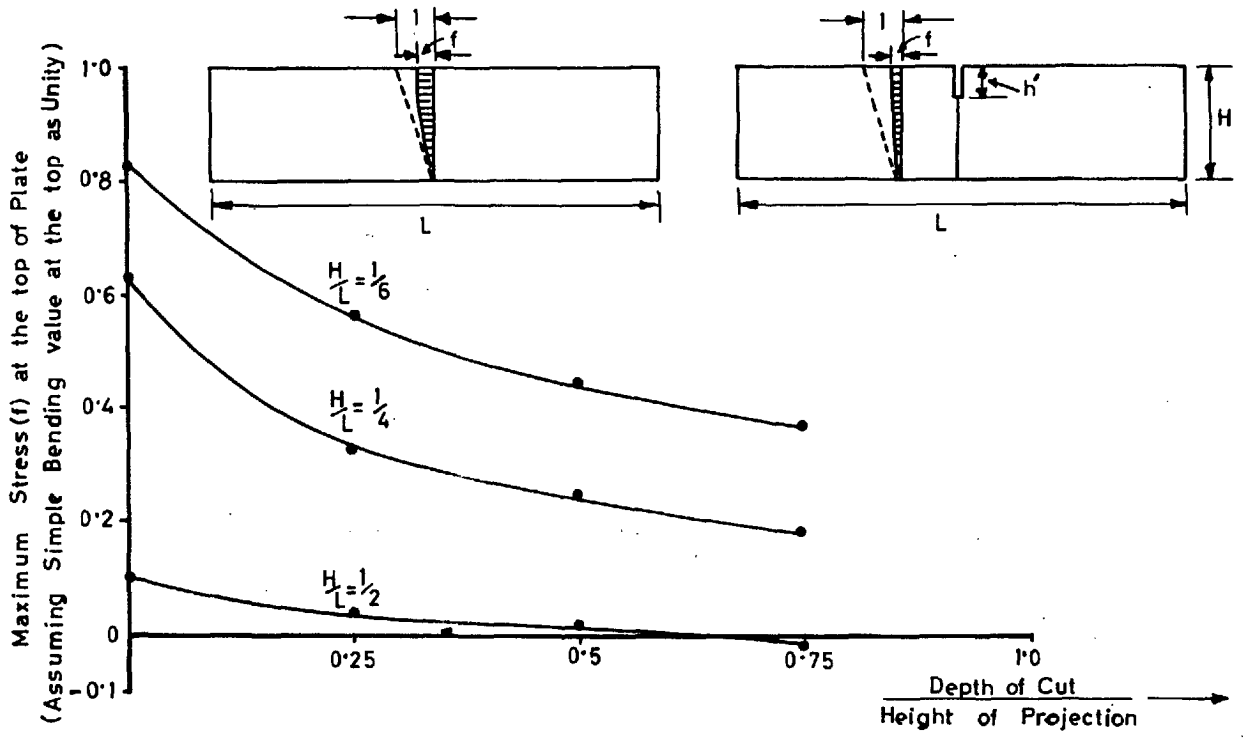

(b) Uniform Curvature and zero strain imposed along the base

Figure.15. Effect of depth of cut on longitudinal stress at the top of Plate projections of different side ratios.

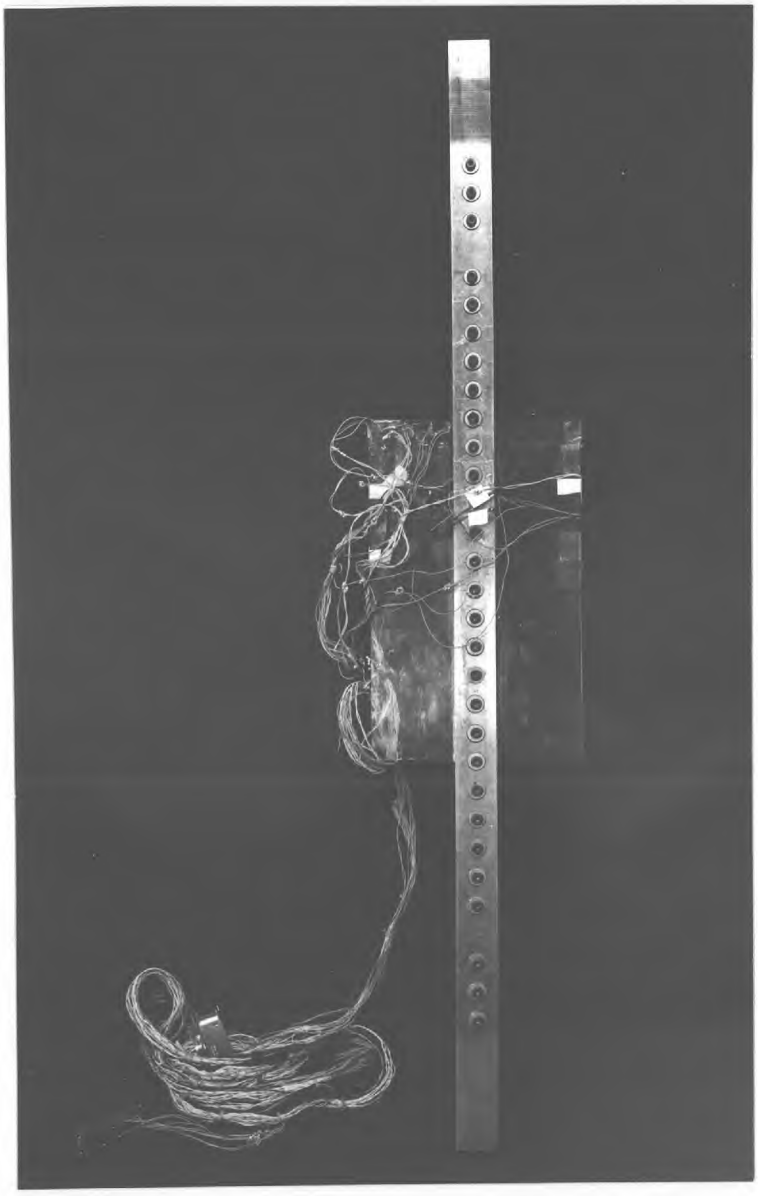

Figure 16 Experimental Projection

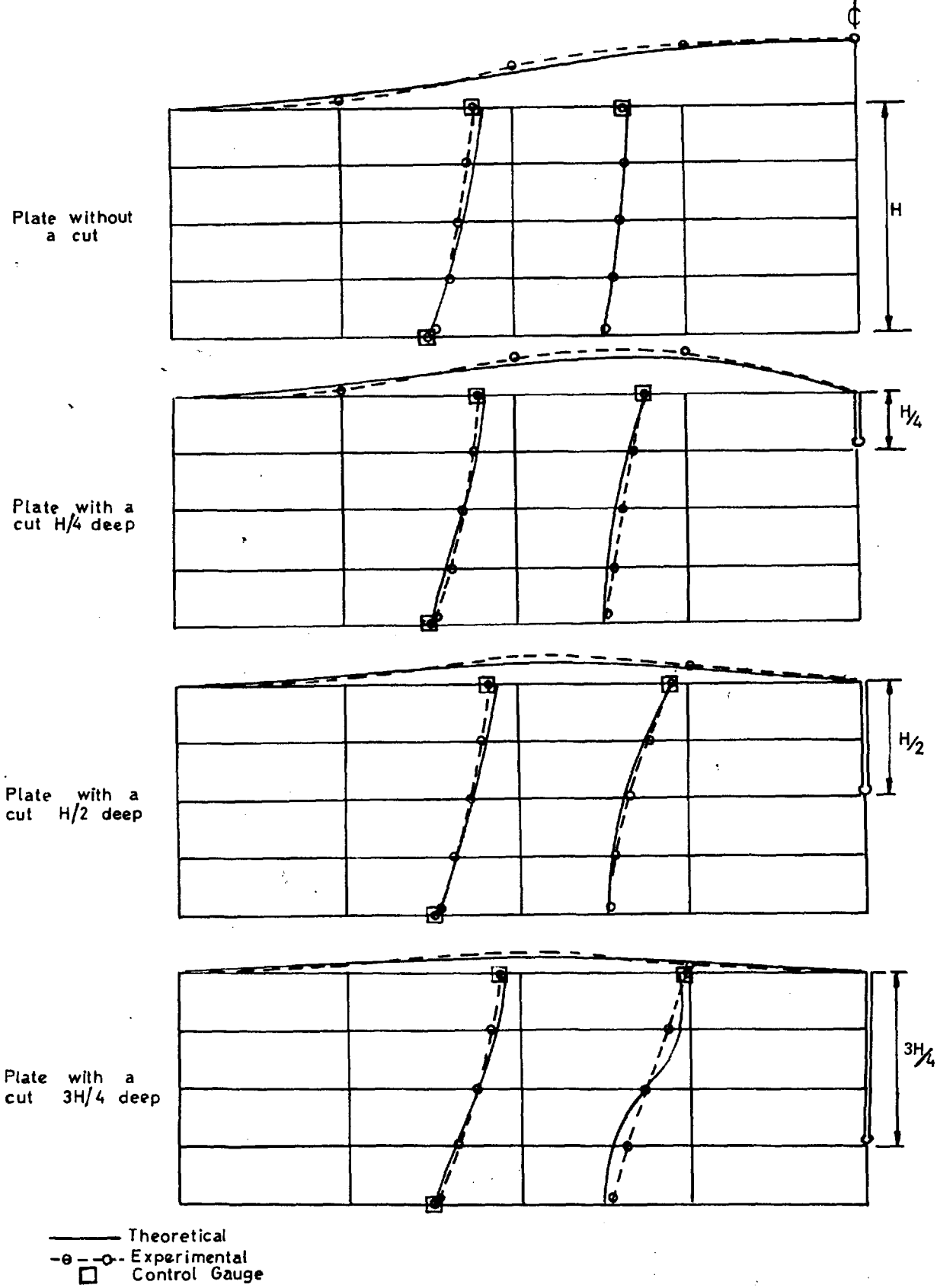

Figure.17. Experimental and theoretical longitudinal strain for 1:6 plate with a cut of varying depth (Constant strain and zero curvature imposed along the base.)

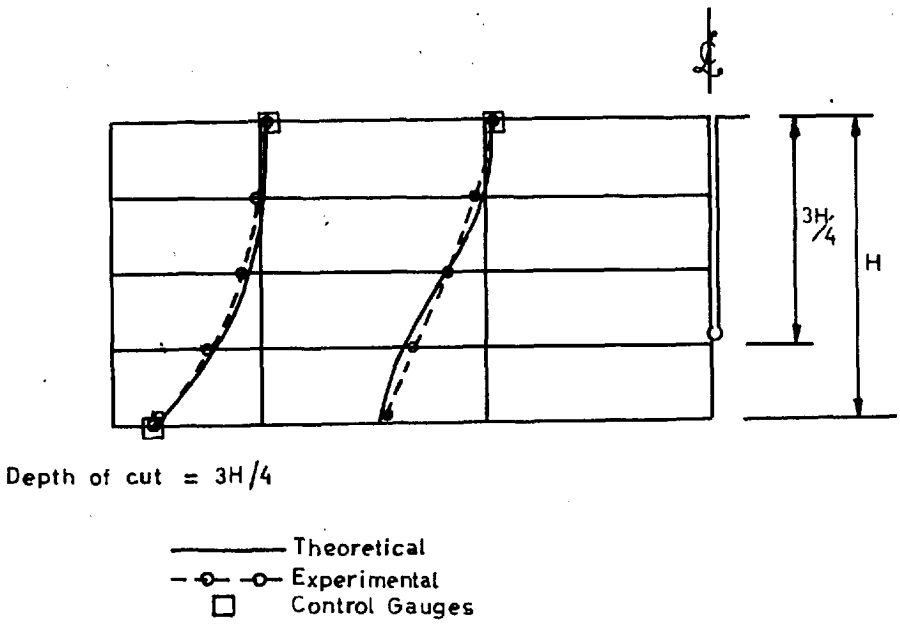

Figure.18. Experimental and theoretical longitudinal strain for 1:4 plate with a cut (Constant strain and zero curvature imposed along the base.)

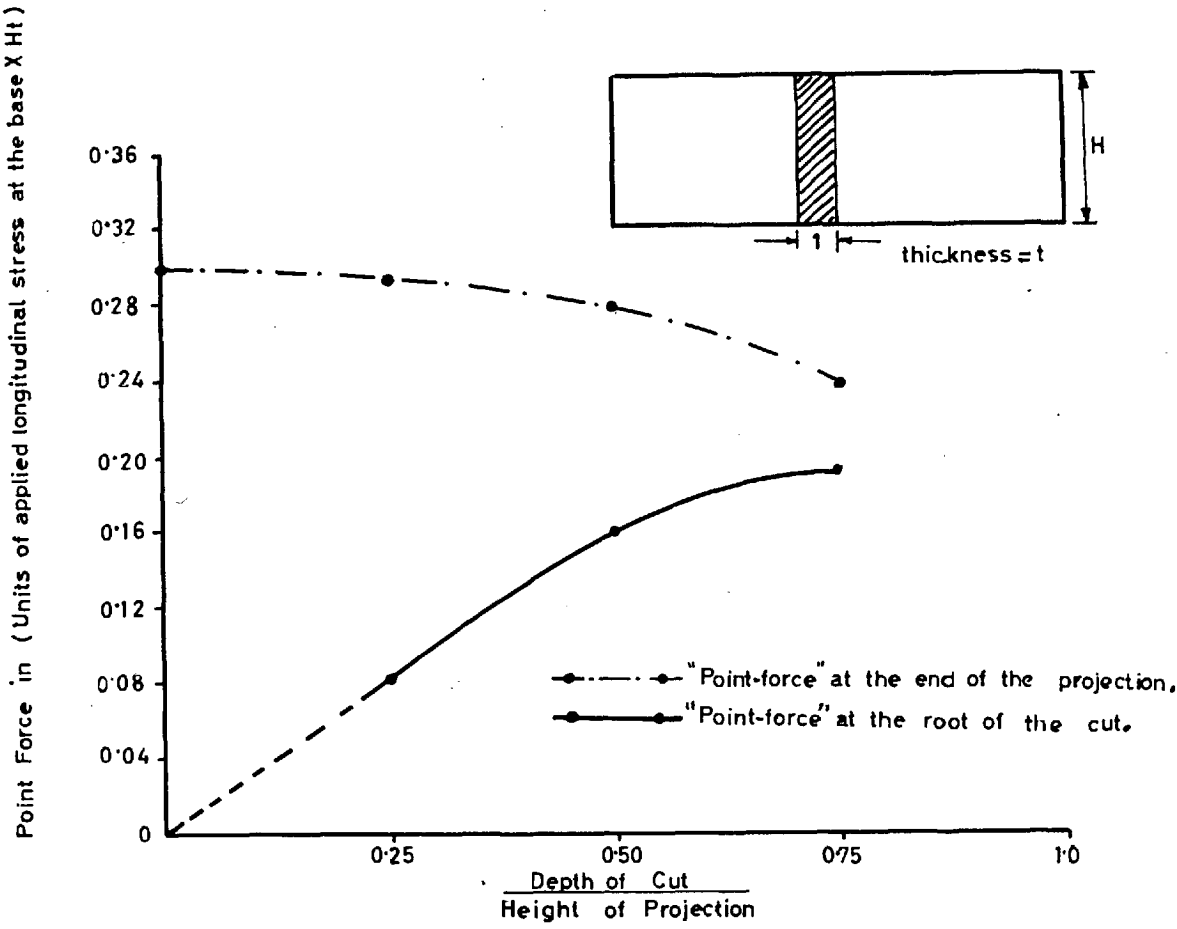

(a) Constant strain and zero curvature imposed along the base

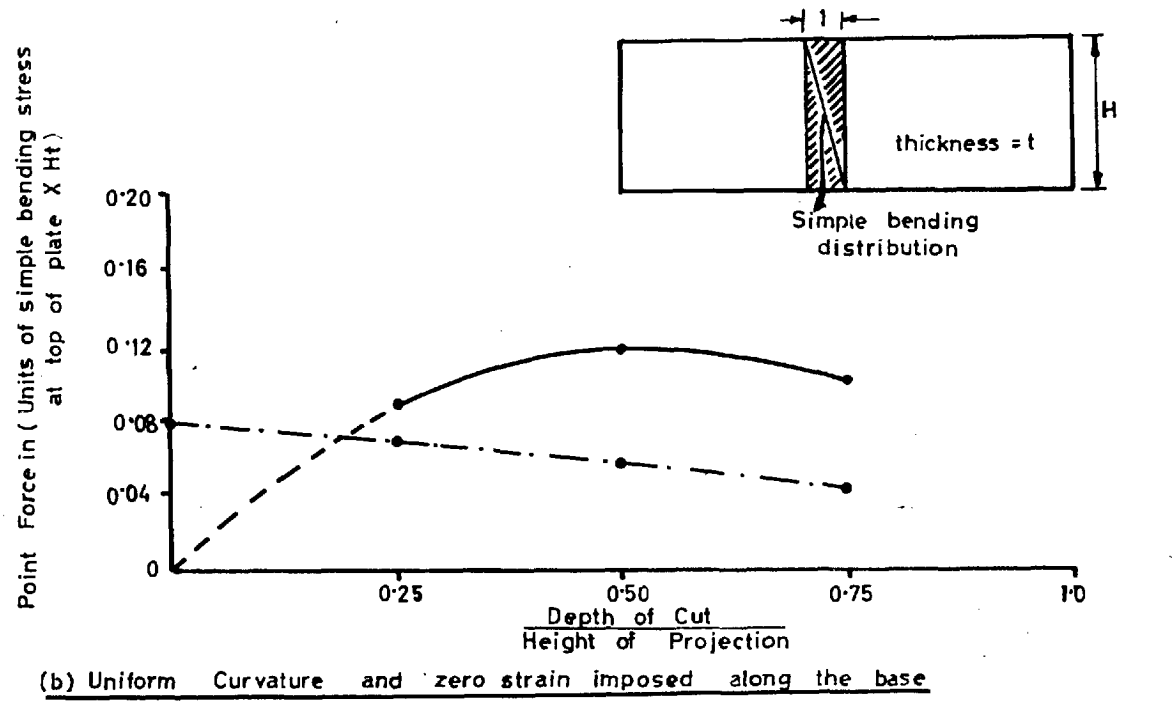

(b) Uniform Curvature and zero strain imposed along the base

Figure. 19 . Variation of "Point-Forces" at the end of the projection and at the root of a central cut, due to the depth of the cut.

(Side ratio of the projection = 1:4)

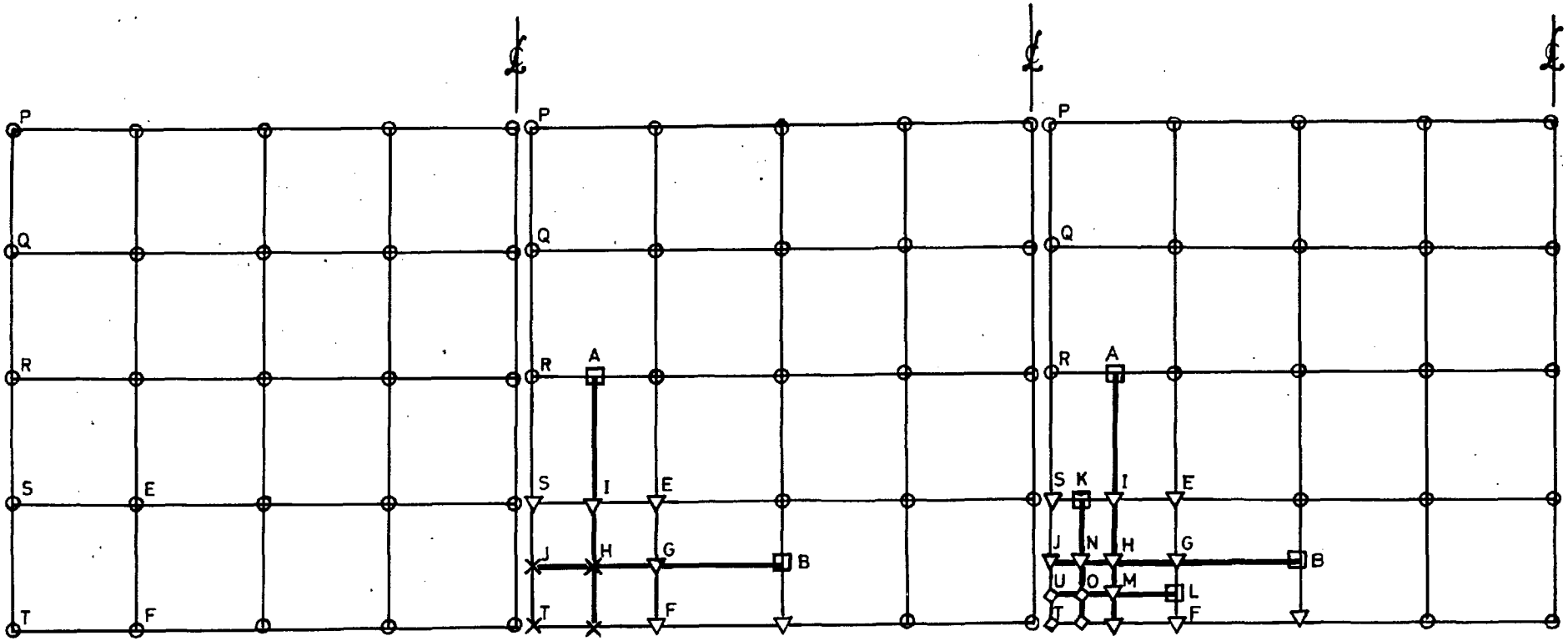

(a) COARSE MESH
(Number of equations = 36)

(b) FIRST GRADING
(Number of equations = 44)

(c) SECOND GRADING
(Number of equations = 52)

- O Coarse Mesh.
- × Fine mesh (First Grading).
- ◇ Fine mesh (Second Grading).
- ▽ Points with unequal mesh lengths in different directions.
- □ Parabolically interpolated points.

Figure.20. Stages of grading of net

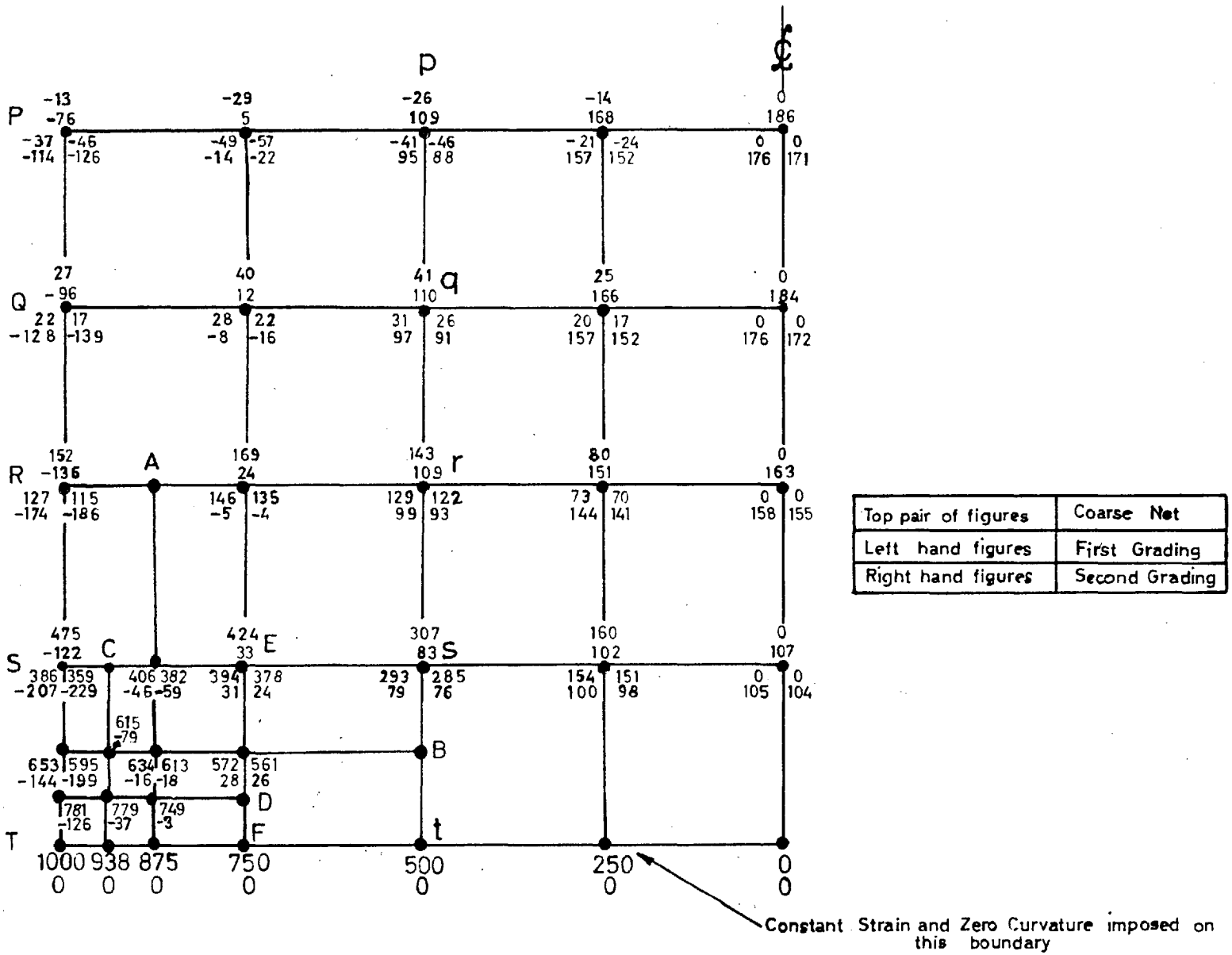

Figure.21. Effect of grading of net on displacements (u and v) for 1:2 plate.

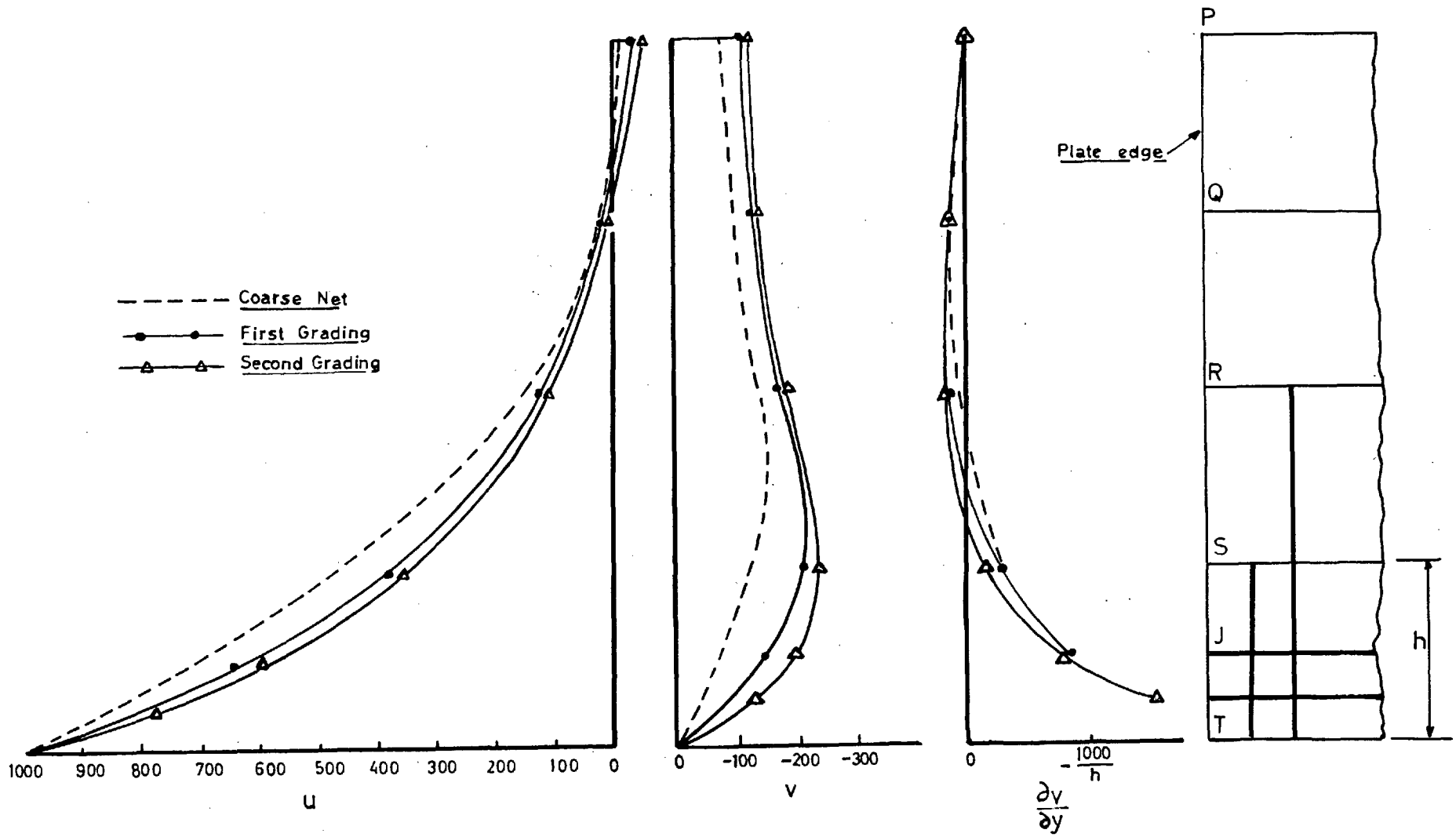

Figure.22. Effect of grading of net on u , v and $\frac{\partial v}{\partial y}$ along the free edge of the plate

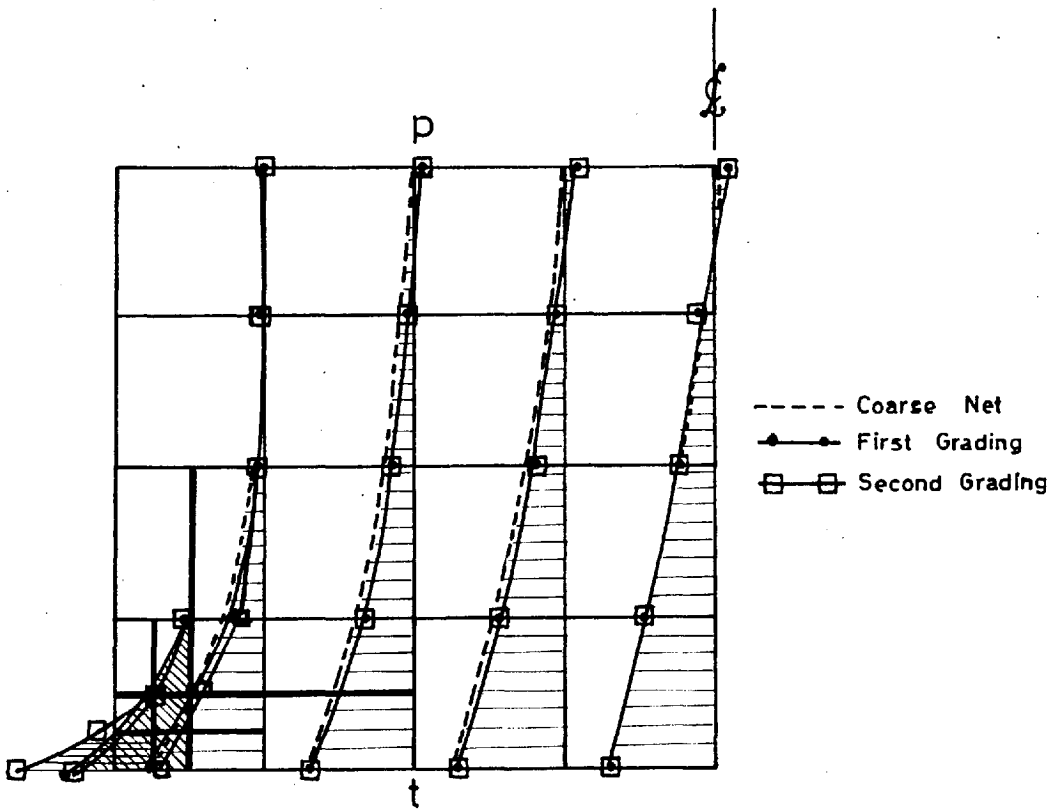

Figure. 23. Effect of grading of net on longitudinal stress σ_x (1:2 plate)

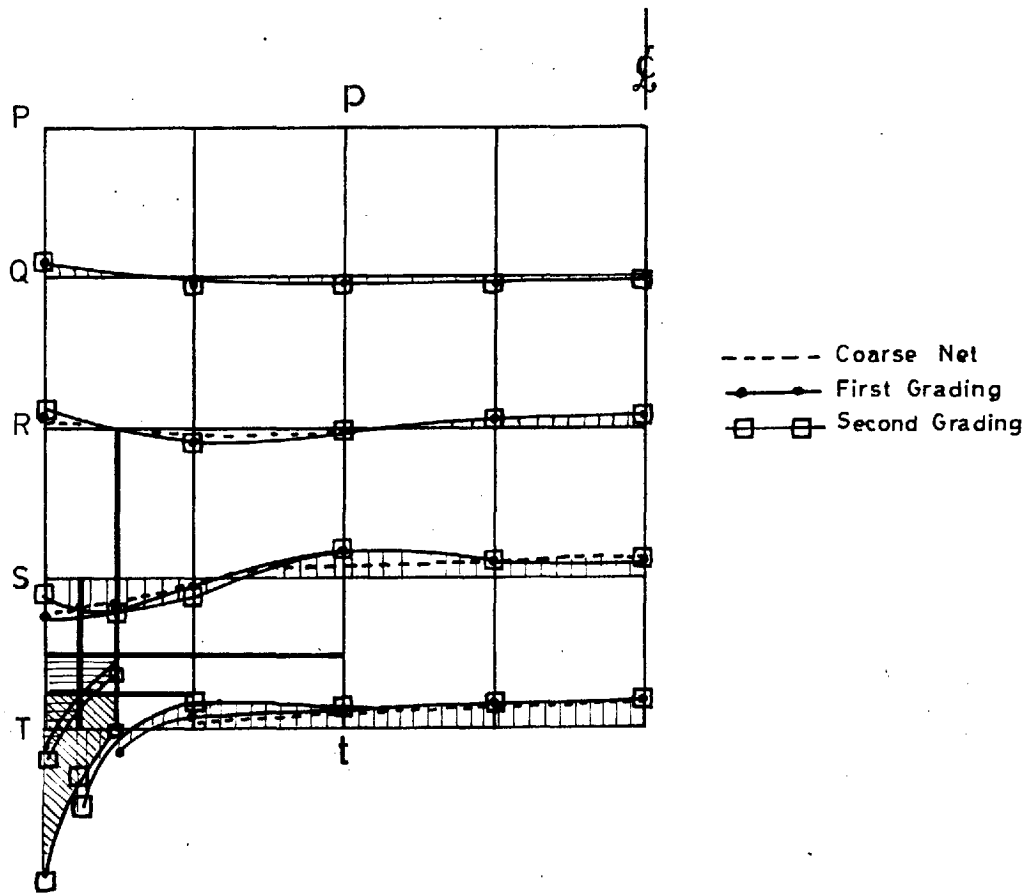

Figure. 24. Effect of grading of net on transverse stress σ_y (1:2 plate)

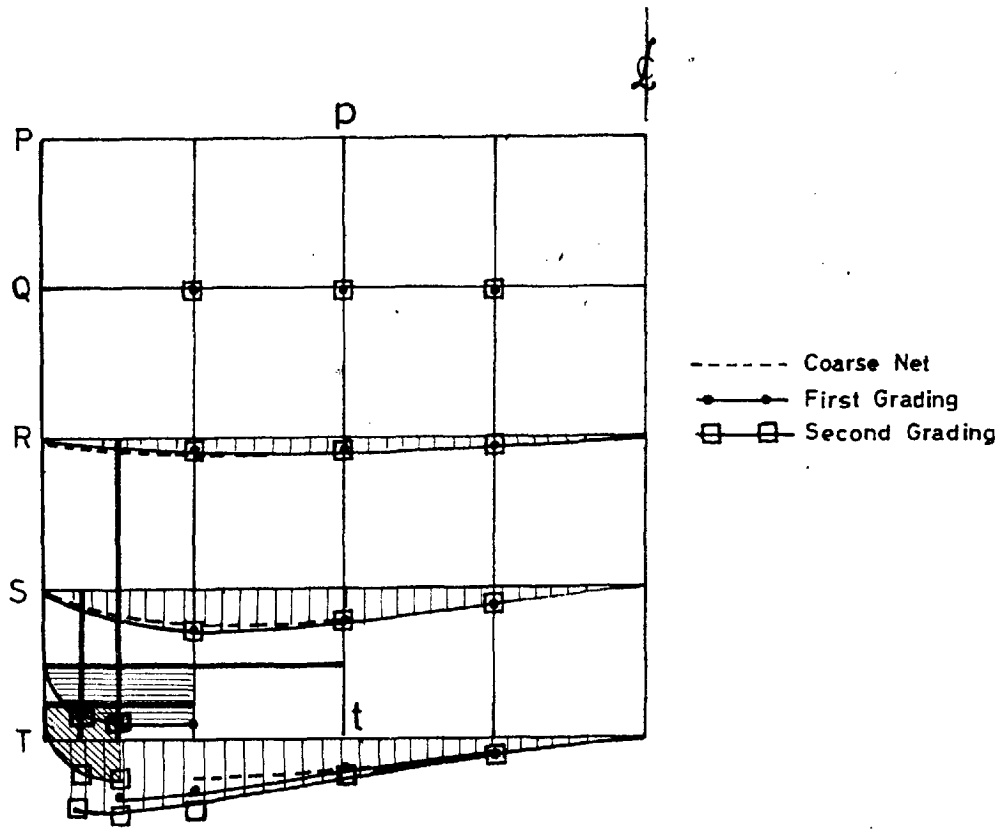

Figure.25. Effect of grading of net on shear stress τ_{xy} (1:2 plate)

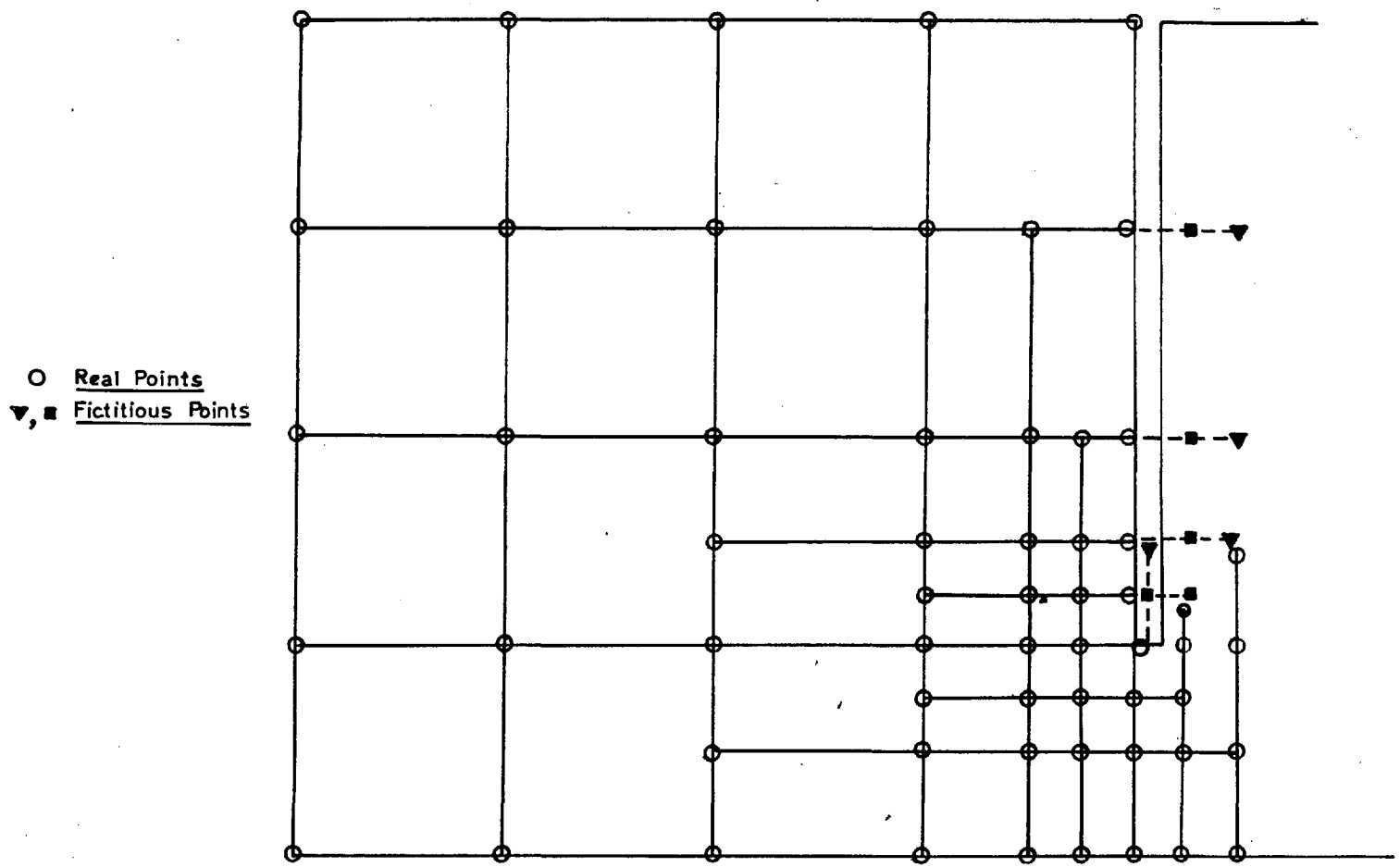

Figure.26. Possible method of grading a net around a straight cut.

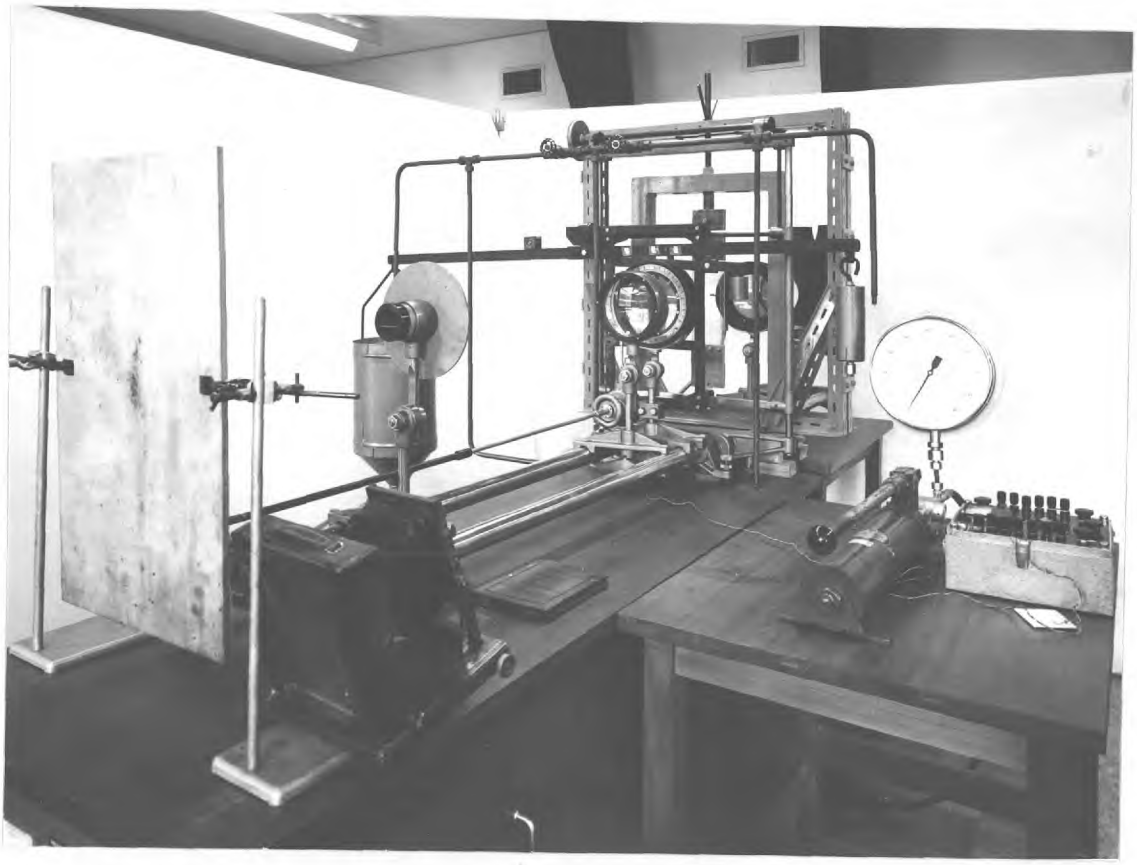

Figure 27 The Loading frame and Polariscope

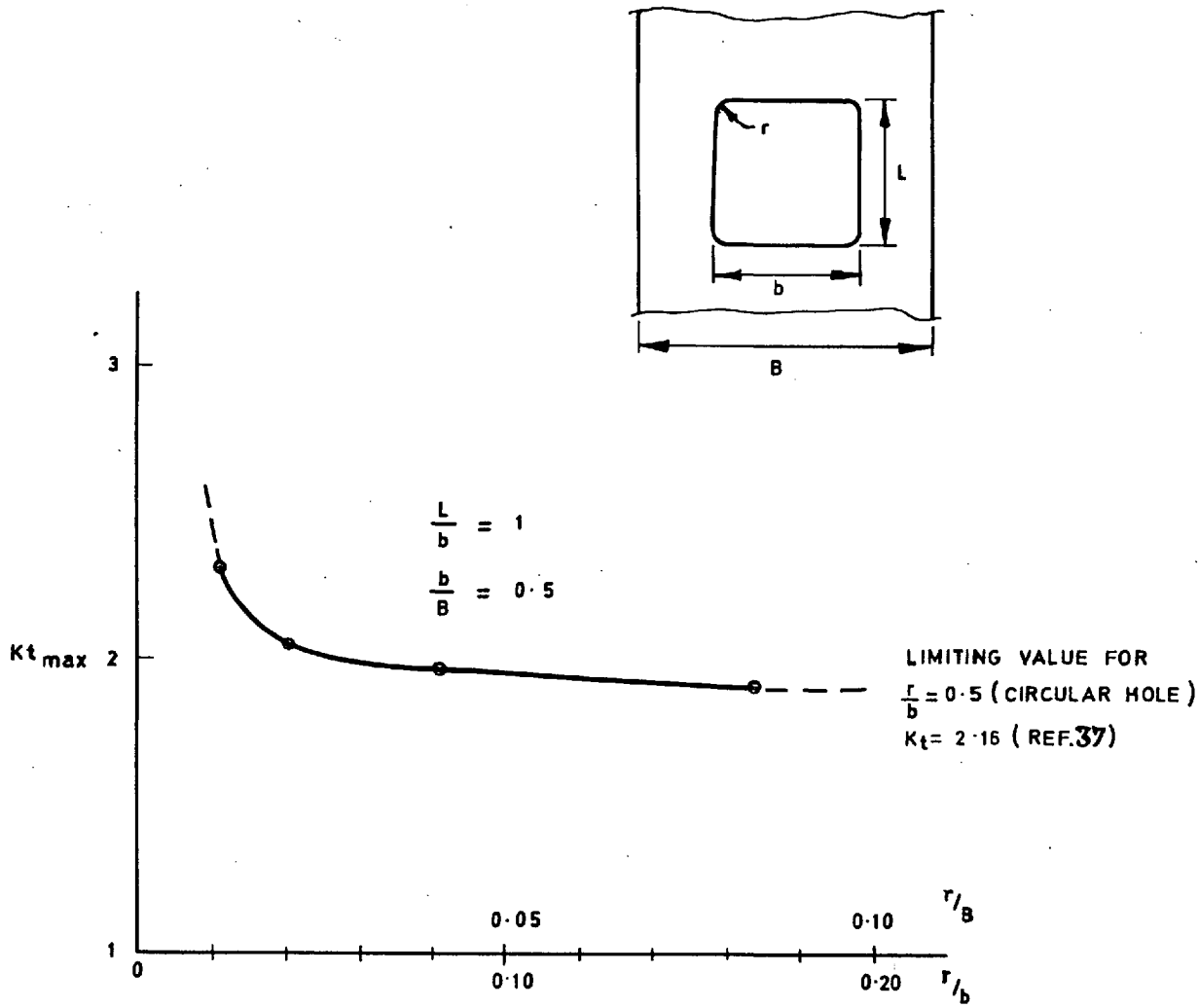

Figure 28. Variation of stress concentration with corner radius
(Photoelastic Tests)

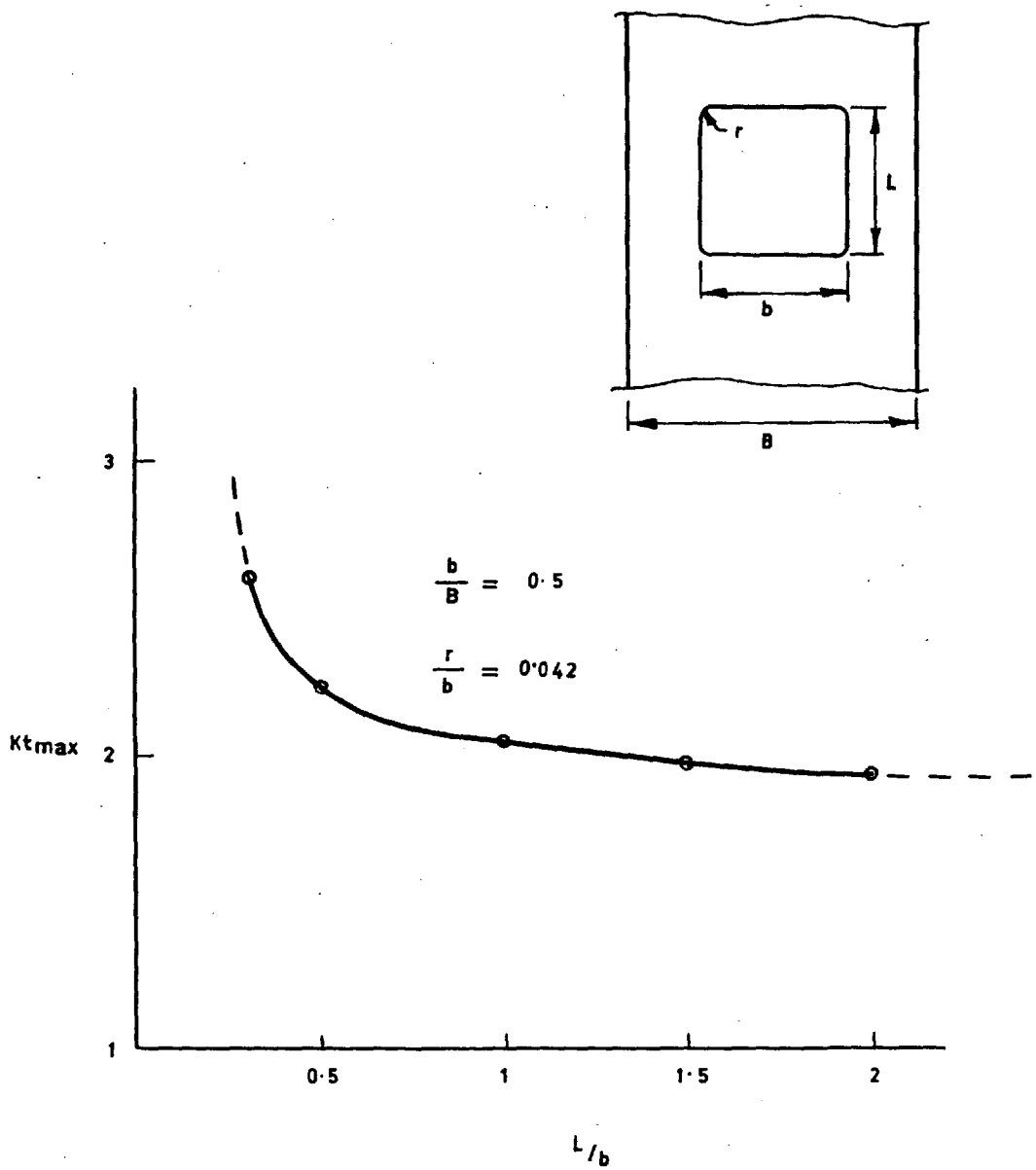

Figure 29. Variation of stress concentration with length of opening.
(Photoelastic Tests)

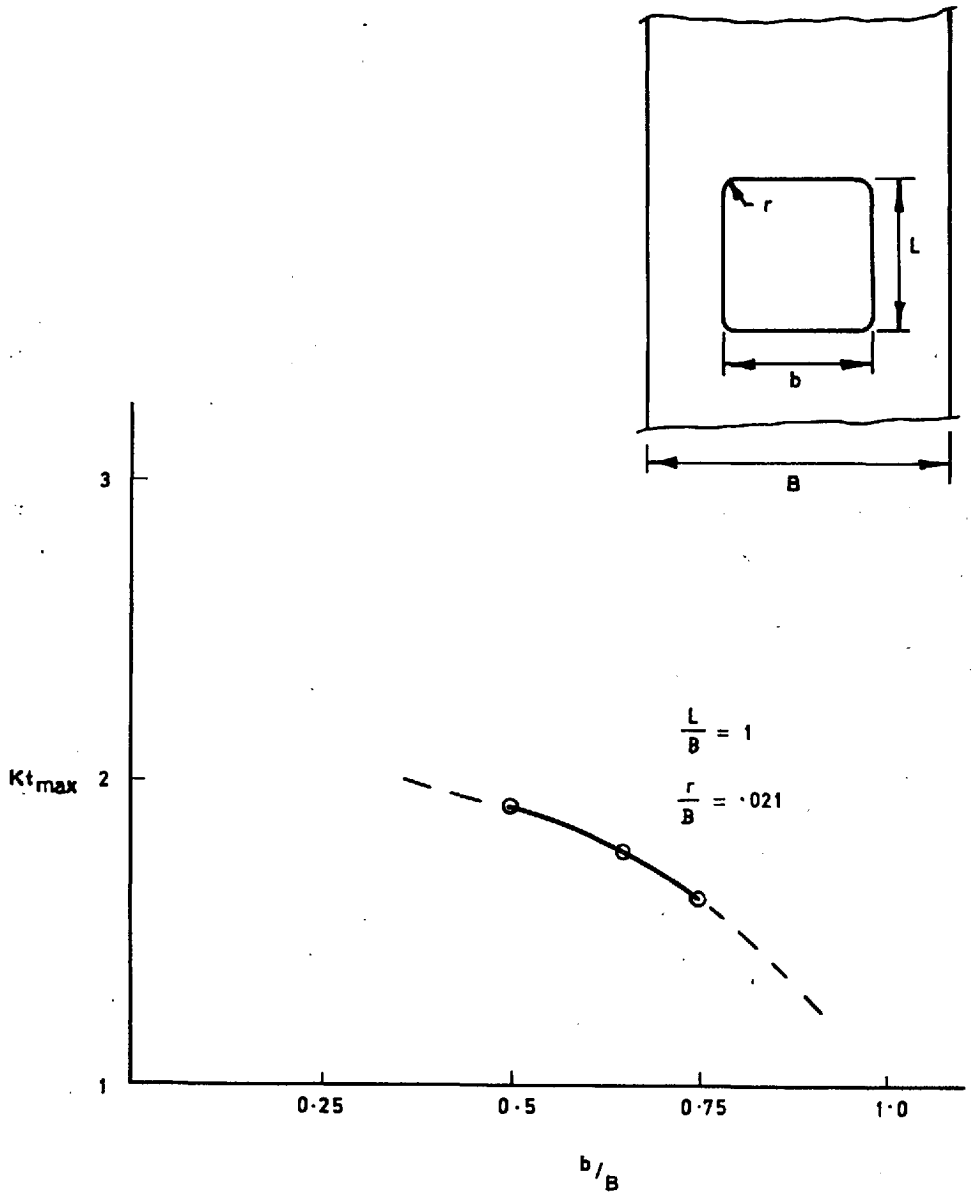

Figure.30. Variation of stress concentration with width of opening
(Photoelastic Tests)

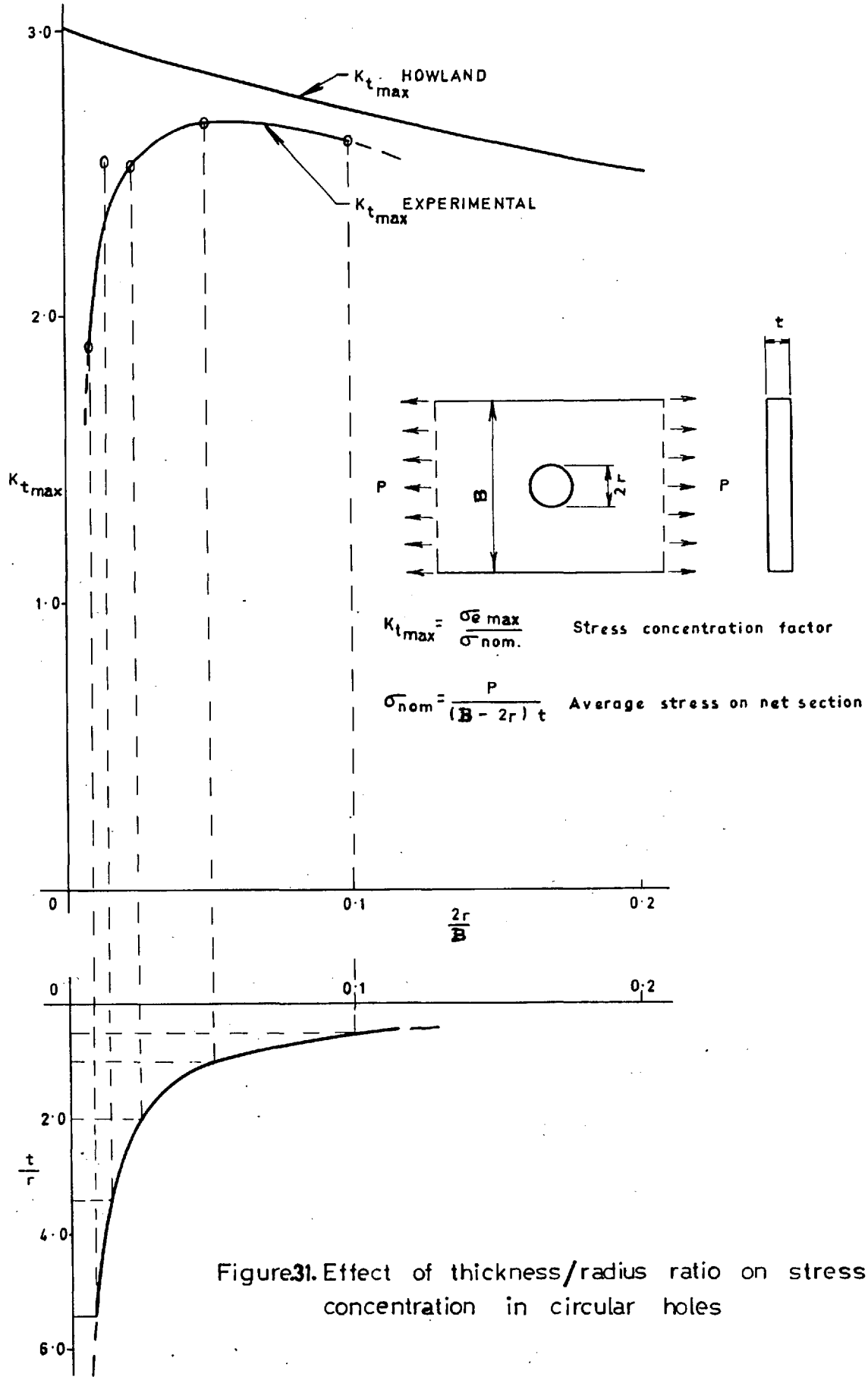

Figure 31. Effect of thickness/radius ratio on stress concentration in circular holes

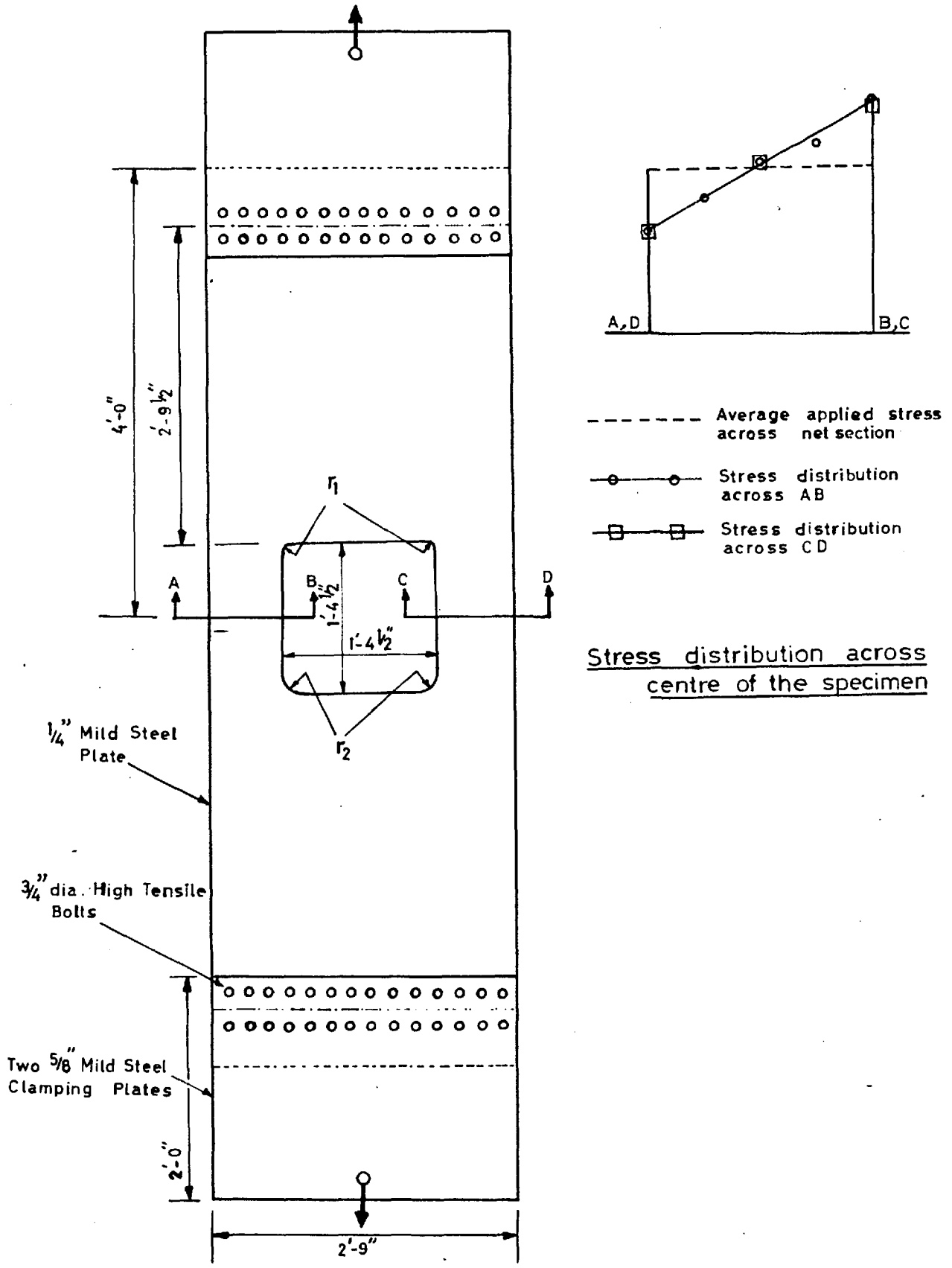

Figure 32. The Steel Specimen and the distribution of longitudinal stress at its centre.

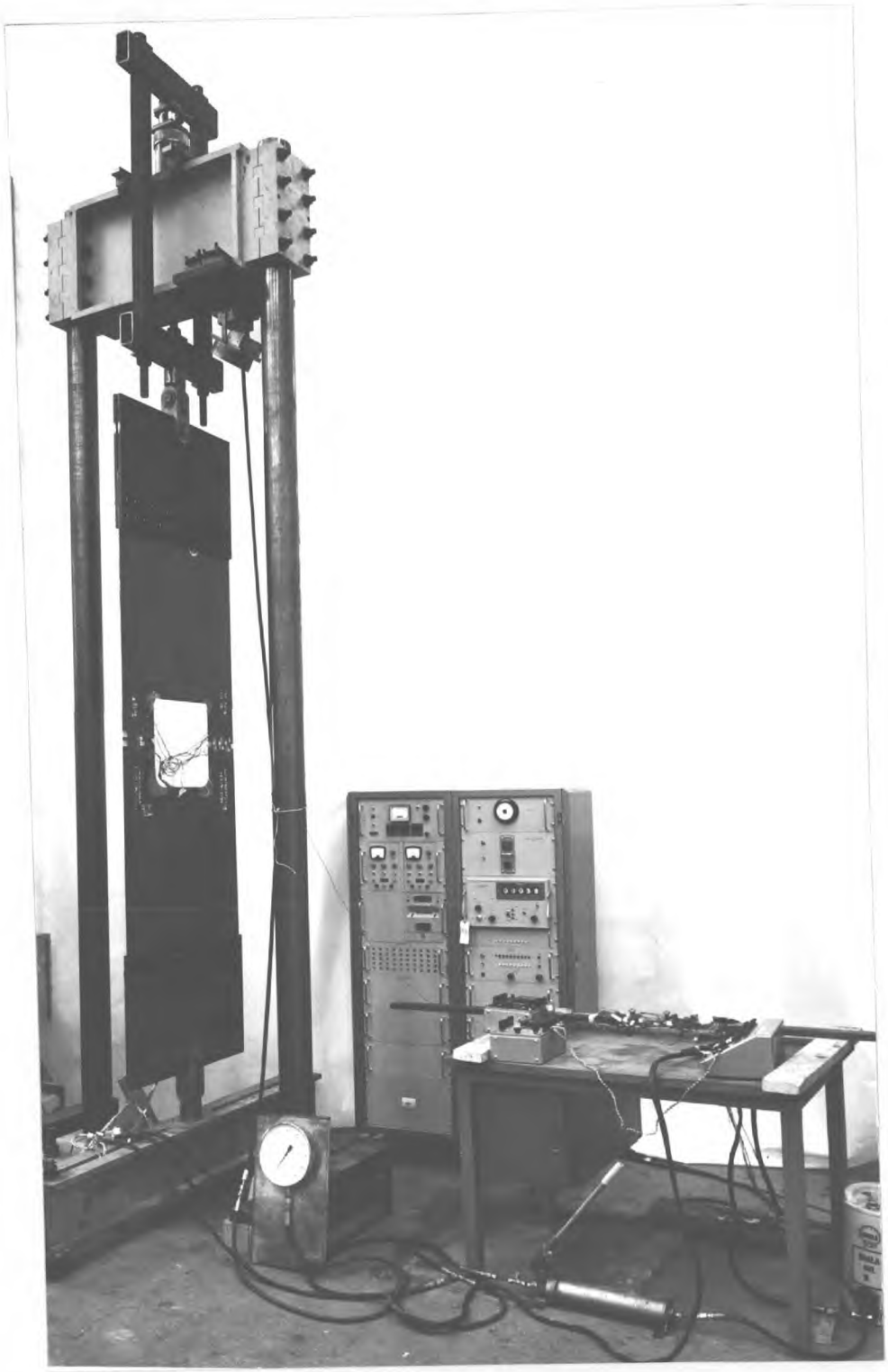

Figure 33 Test Arrangement

Steel Specimen
(Hatch openings)

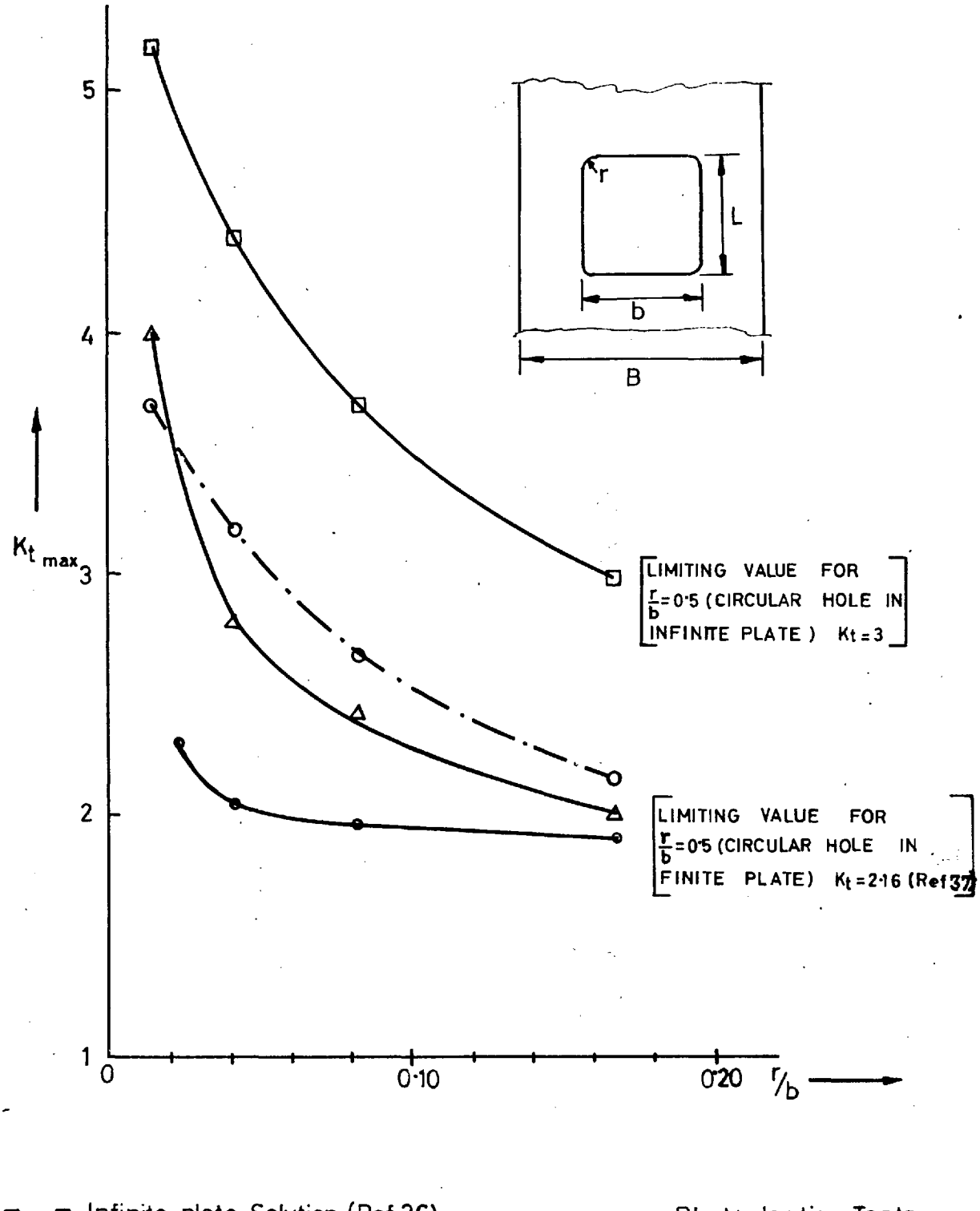

Figure.34.Variation of Stress Concentration with radius/width ratio .

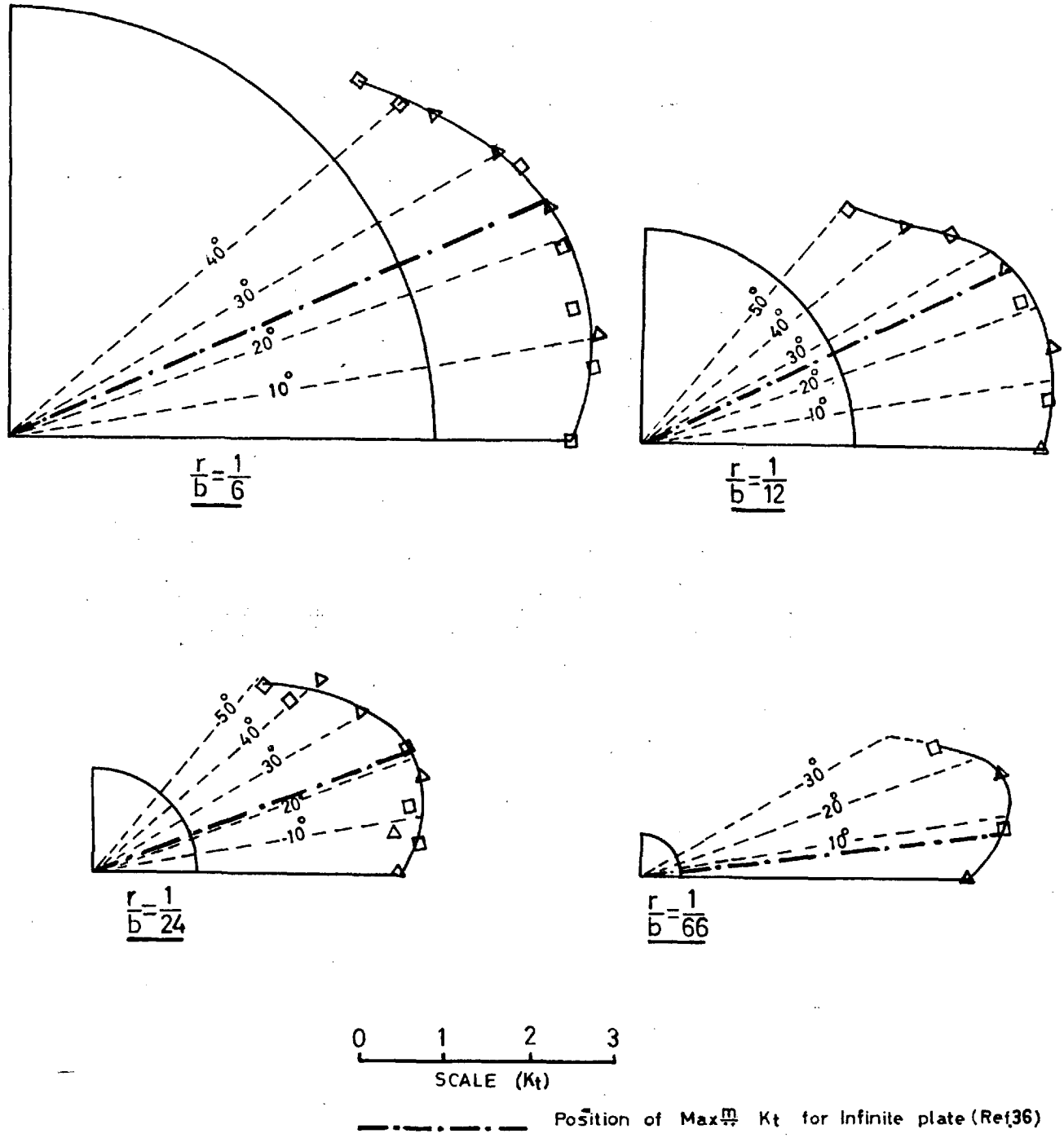

Figure 35. Variation of Stress Concentration along the Corner-radius. ($\frac{L}{b}=1$, $\frac{b}{B}=0.5$)

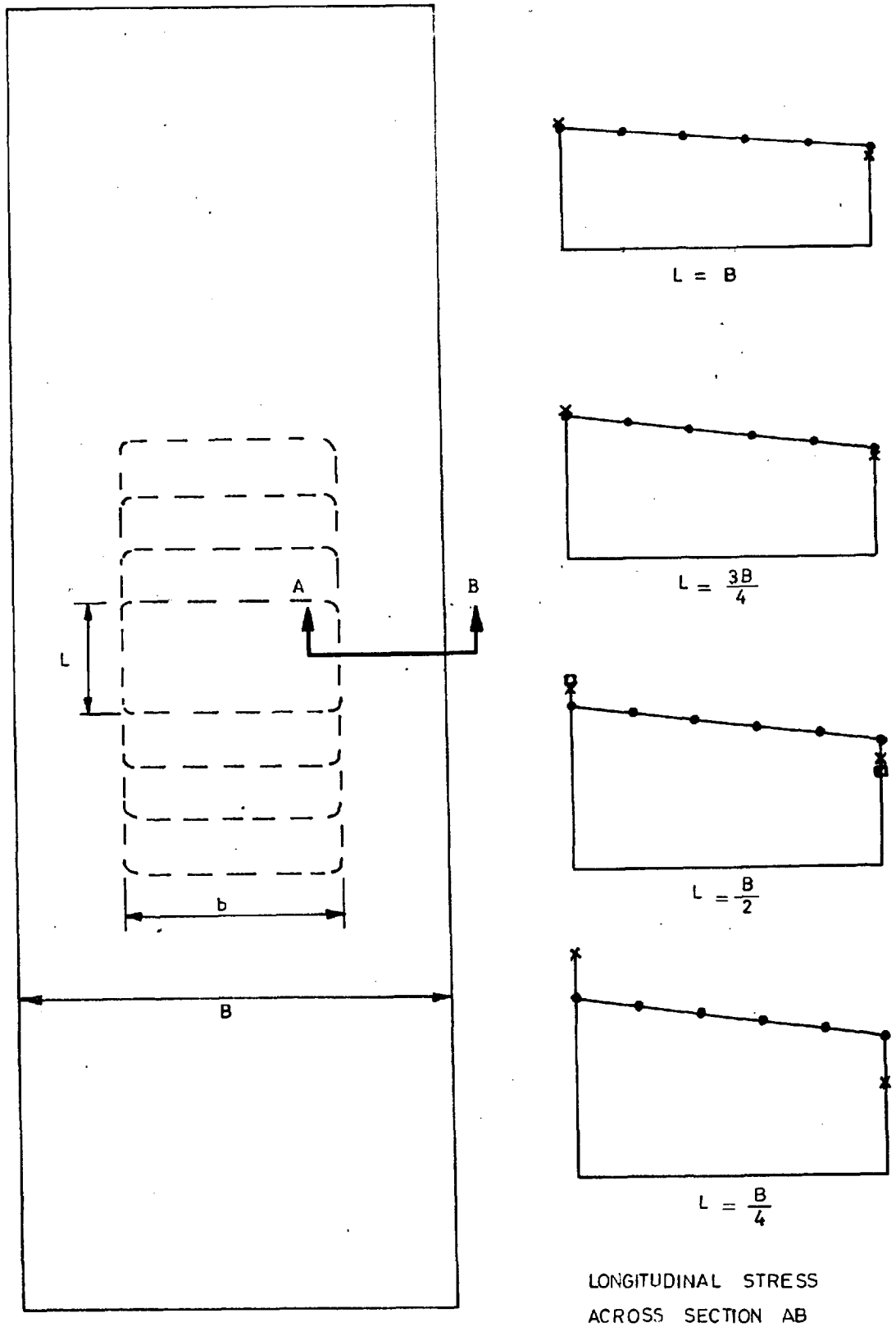

Figure.36. Stress distribution across the centre of specimen with rectangular openings.

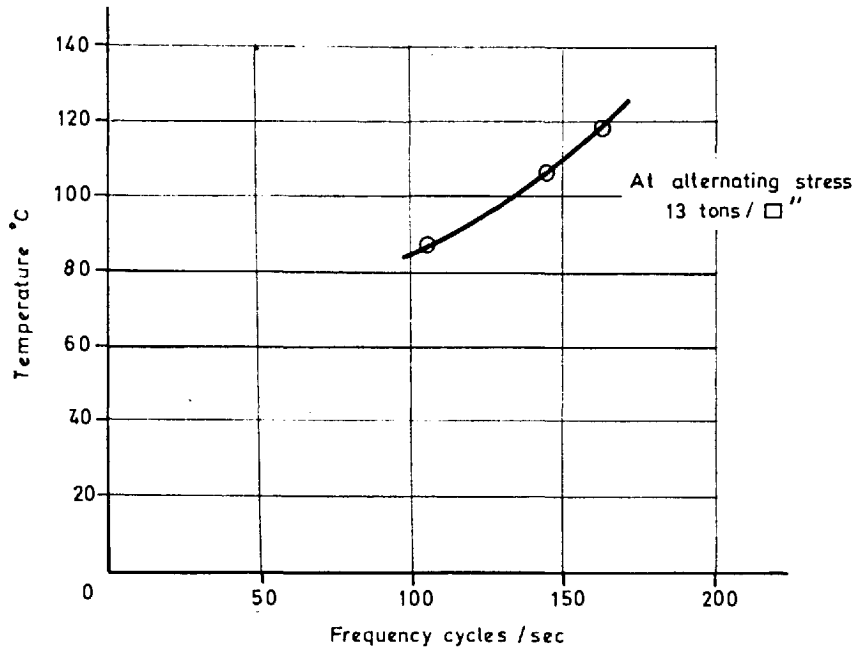

Figure .38. Effect of frequency on specimen temperature.

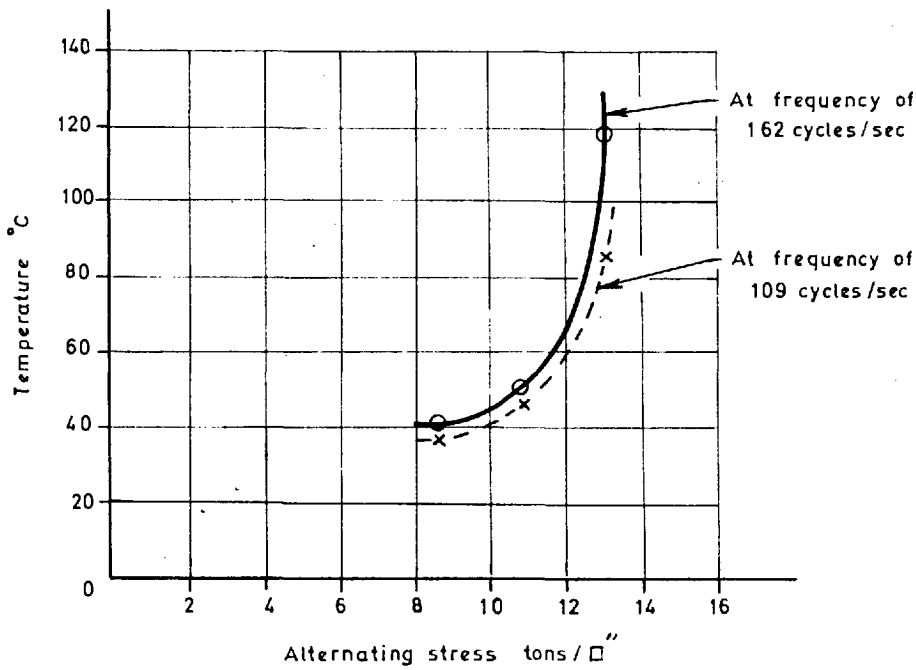

Figure.37. Effect of alternating stress on specimen temperature.

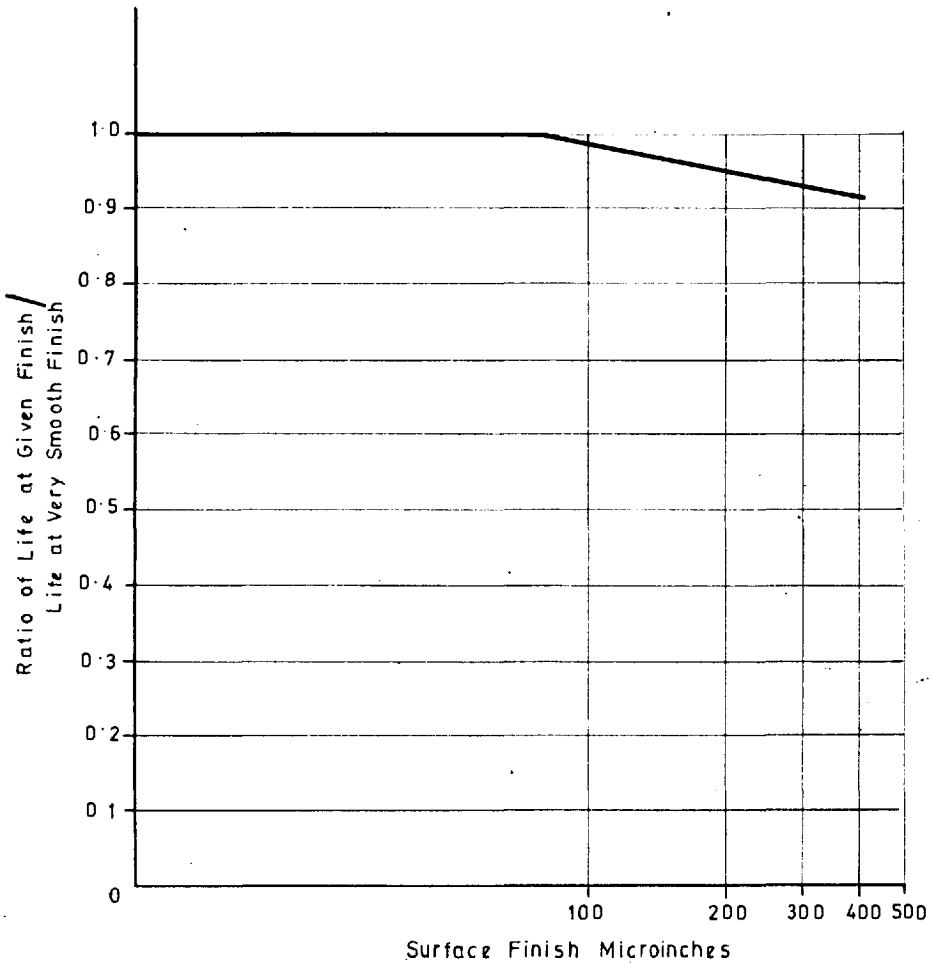

Figure 39. Effect of surface-finish on fatigue-life (Plain specimens)[38]

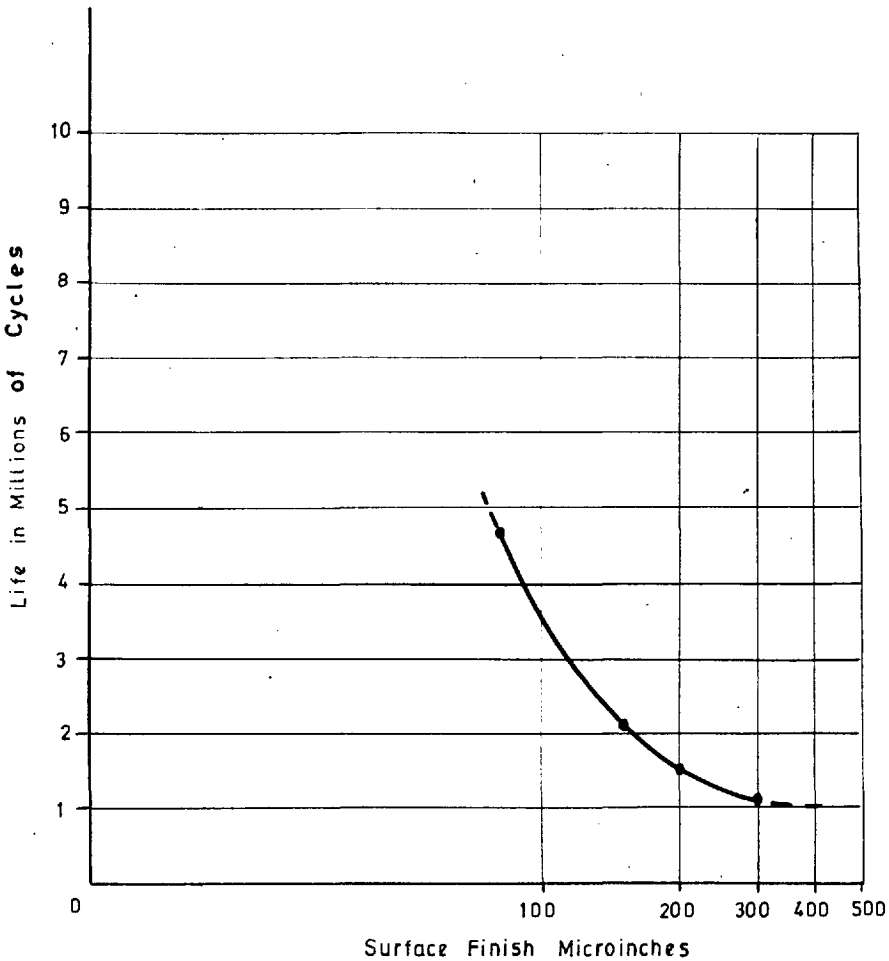

Figure 40. Effect of surface-finish on fatigue-life (Flat specimens with circular holes)

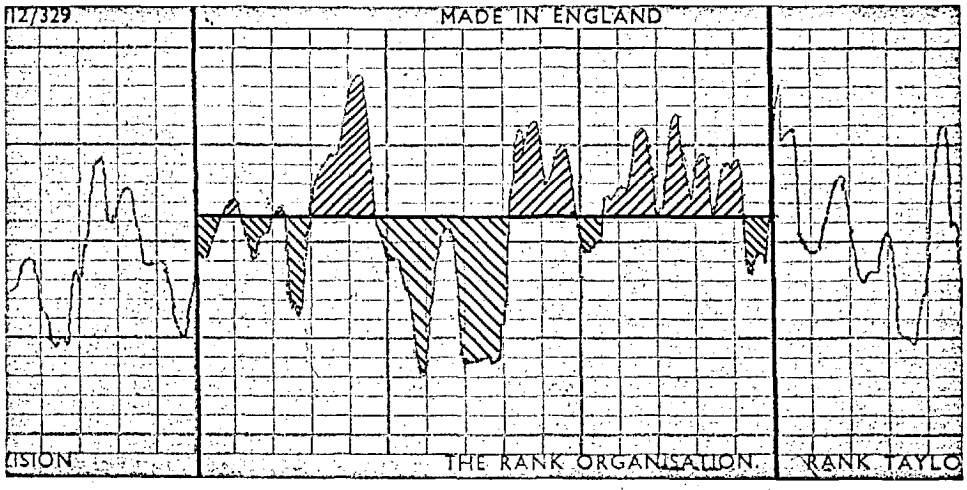

VERTICAL MAGNIFICATION 2000
HORIZONTAL MAGNIFICATION 100

Figure.41. A Typical Surface-finish Record.

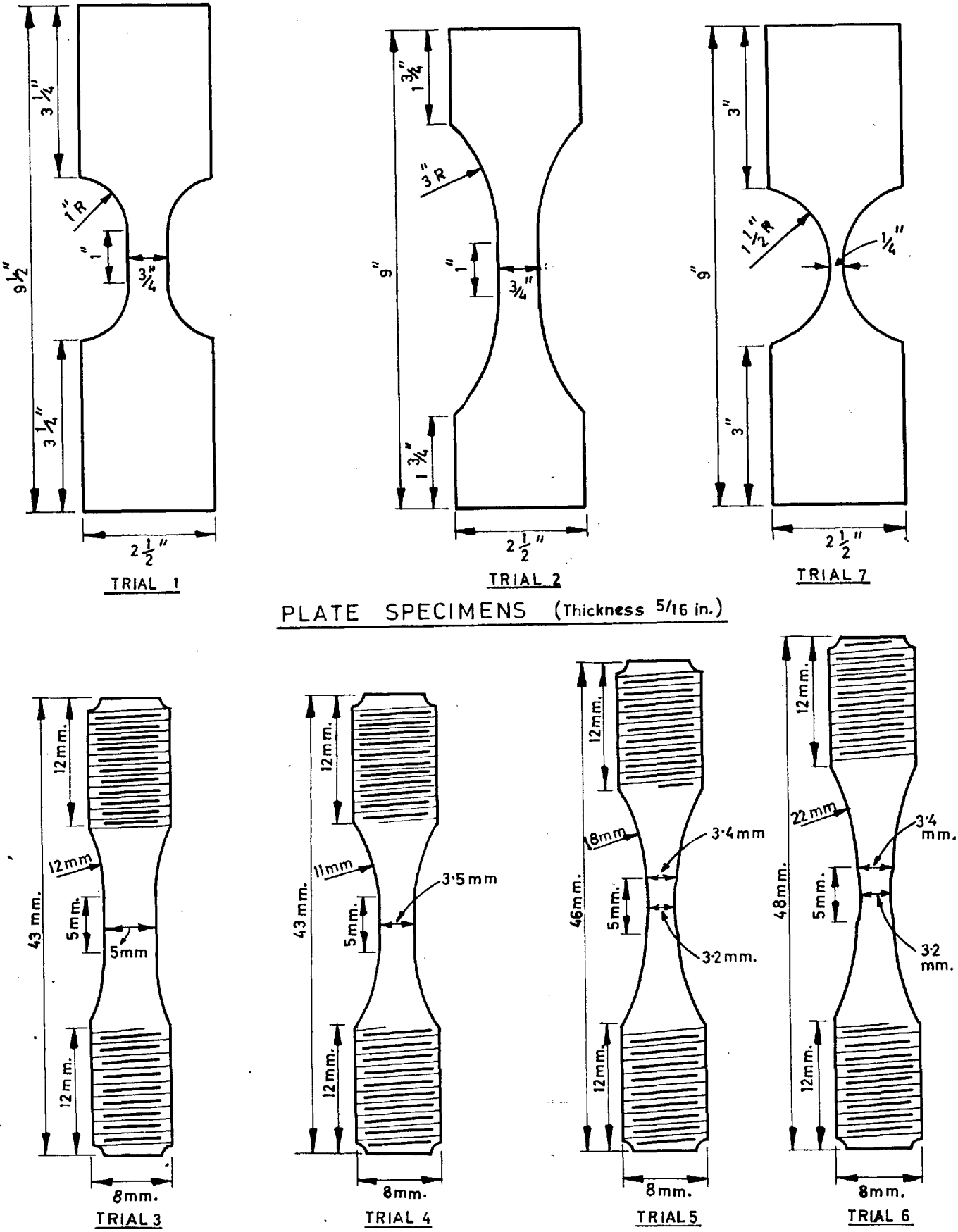

Figure 42. Trial specimens for obtaining fatigue properties of the material

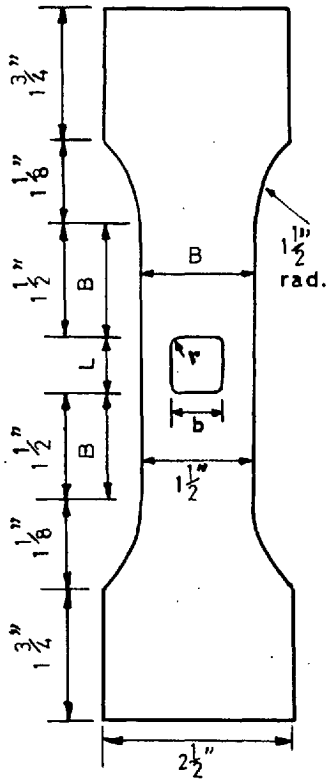

Batch No.	B in.	b in.	b/B	r in.	r/b	L in.	L/b	No. of Specimens
1	1·5	0·75	0·5	1/32	0·042	0·375	0·5	8
2	1·5	0·75	0·5	1/32	0·042	0·75	1	8
3	1·5	0·75	0·5	0	0	0·75	1	8
4	1·5	0·75	0·5	1/16	0·083	0·75	1	8
5	1·5	0·75	0·5	1/8	0·167	0·75	1	8
6	1·5	0·75	0·5	1/32	0·042	1·5	2	8
7	1·5	0·938	0·625	1/32	0·033	1·5	1·8	8
8	1·5	1·125	0·75	1/32	0·028	1·5	1·33	8

Effect of Radius

Effect of Length

Effect of Width

Thickness 5/16 in.

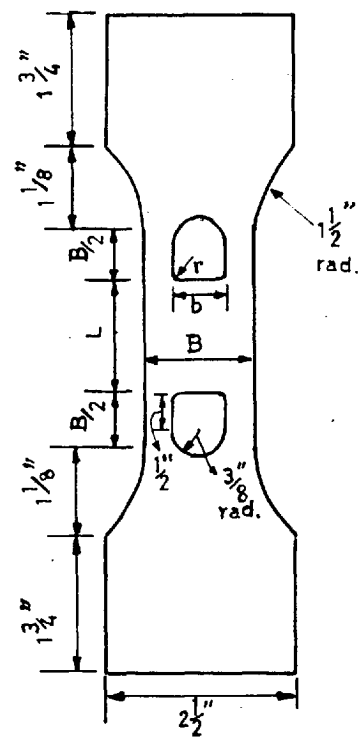

Surface Finish

Top and bottom face	Ground
Sides and edges	Machined
Inside of the opening	Spark-eroded

Figure 43. Specimens for the test-series (Only batches 1 to 5 were fabricated and tested).

Figure 44 The spark-eroding Machine and electrodes

Figure 45 Vibrophore (High frequency fatigue Testing Machine)

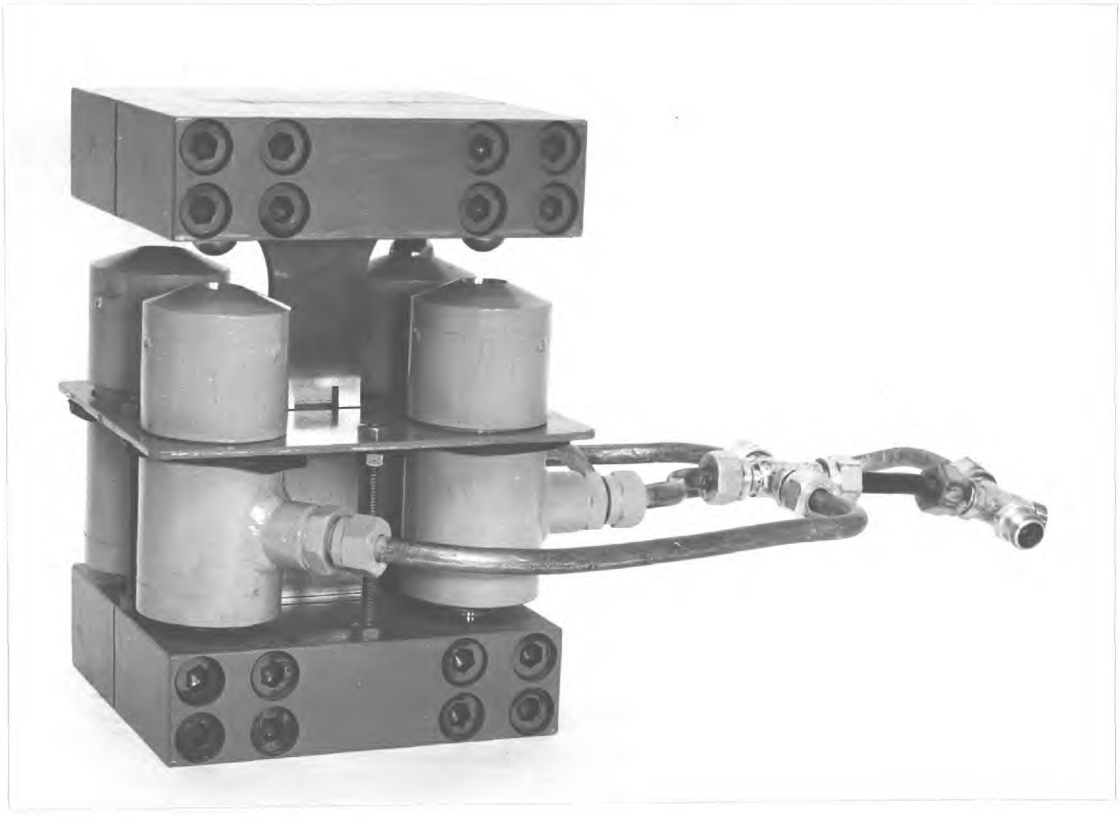

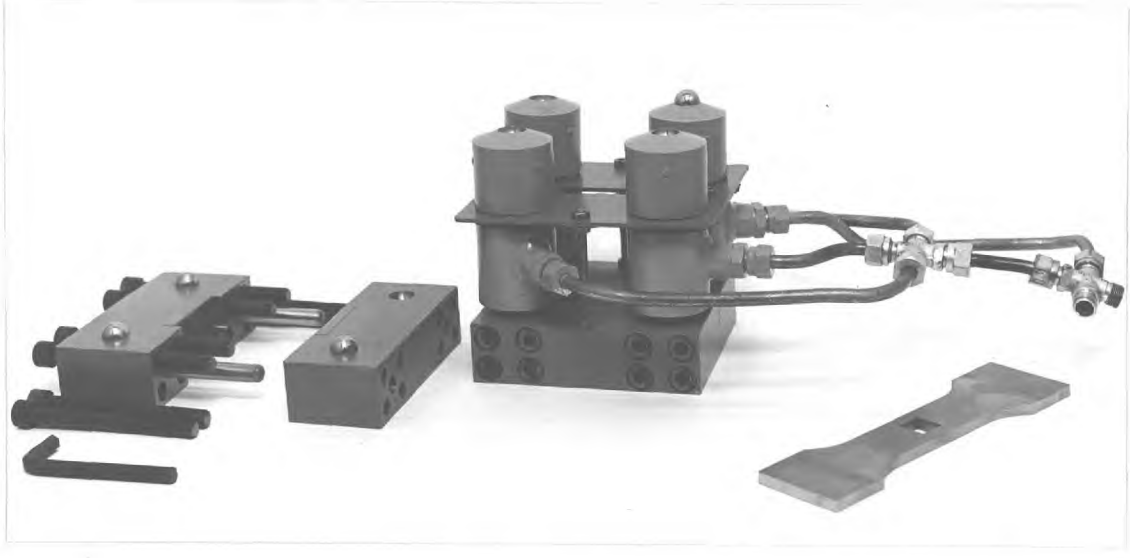

Figure 46 The Low-cycle Test Rig

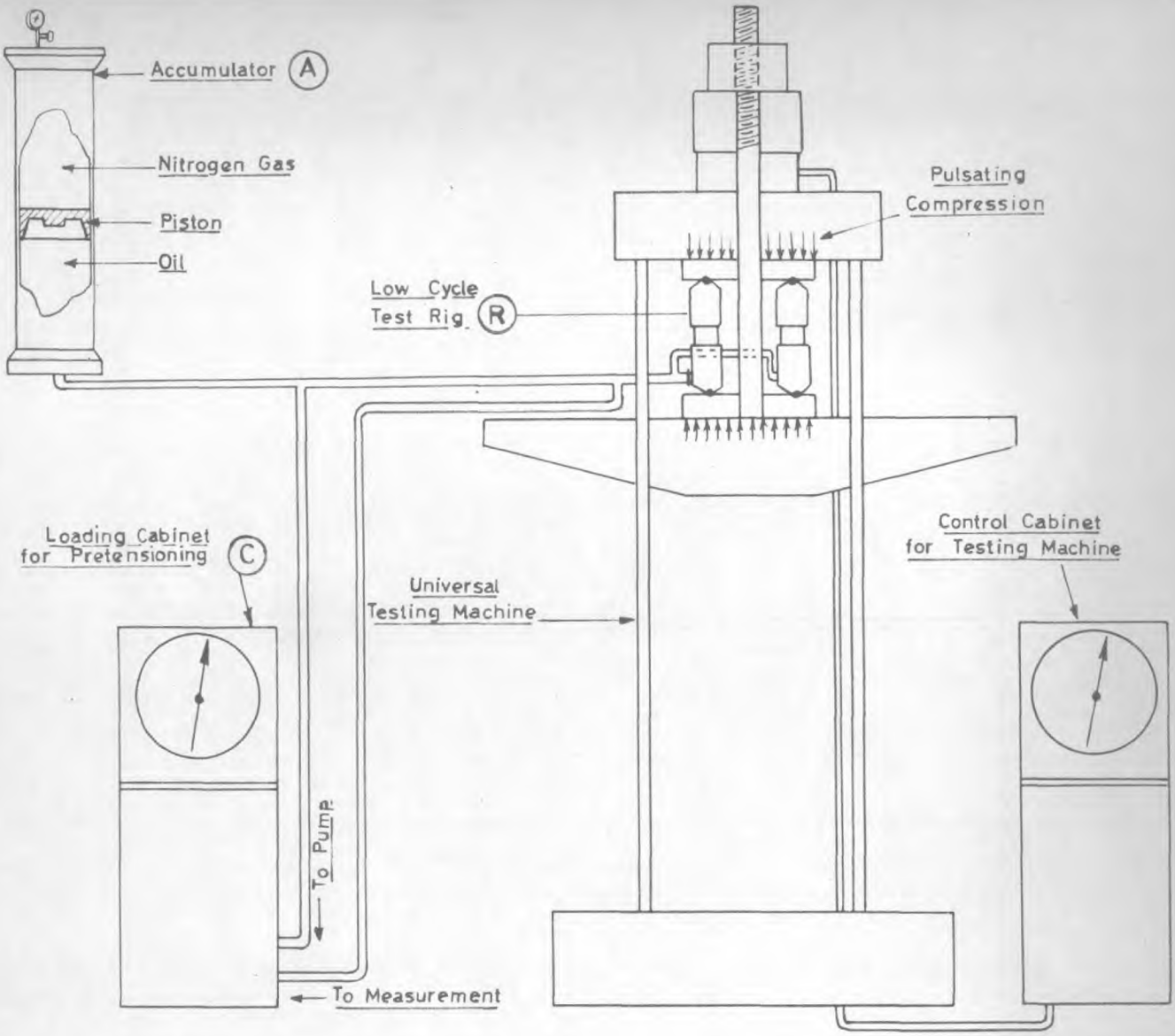

Figure 47. The Low-Cycle Test Assembly

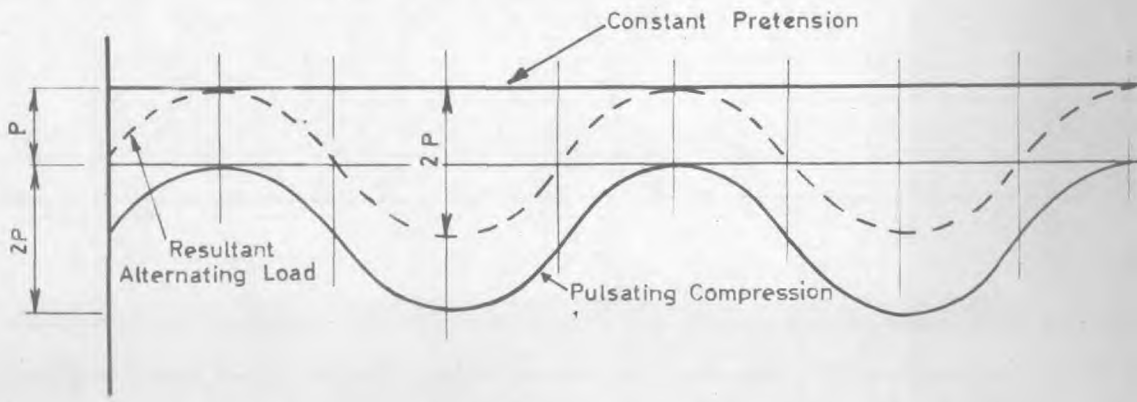

Figure.48. Alternating load obtained by superimposing pulsating compression on constant tension

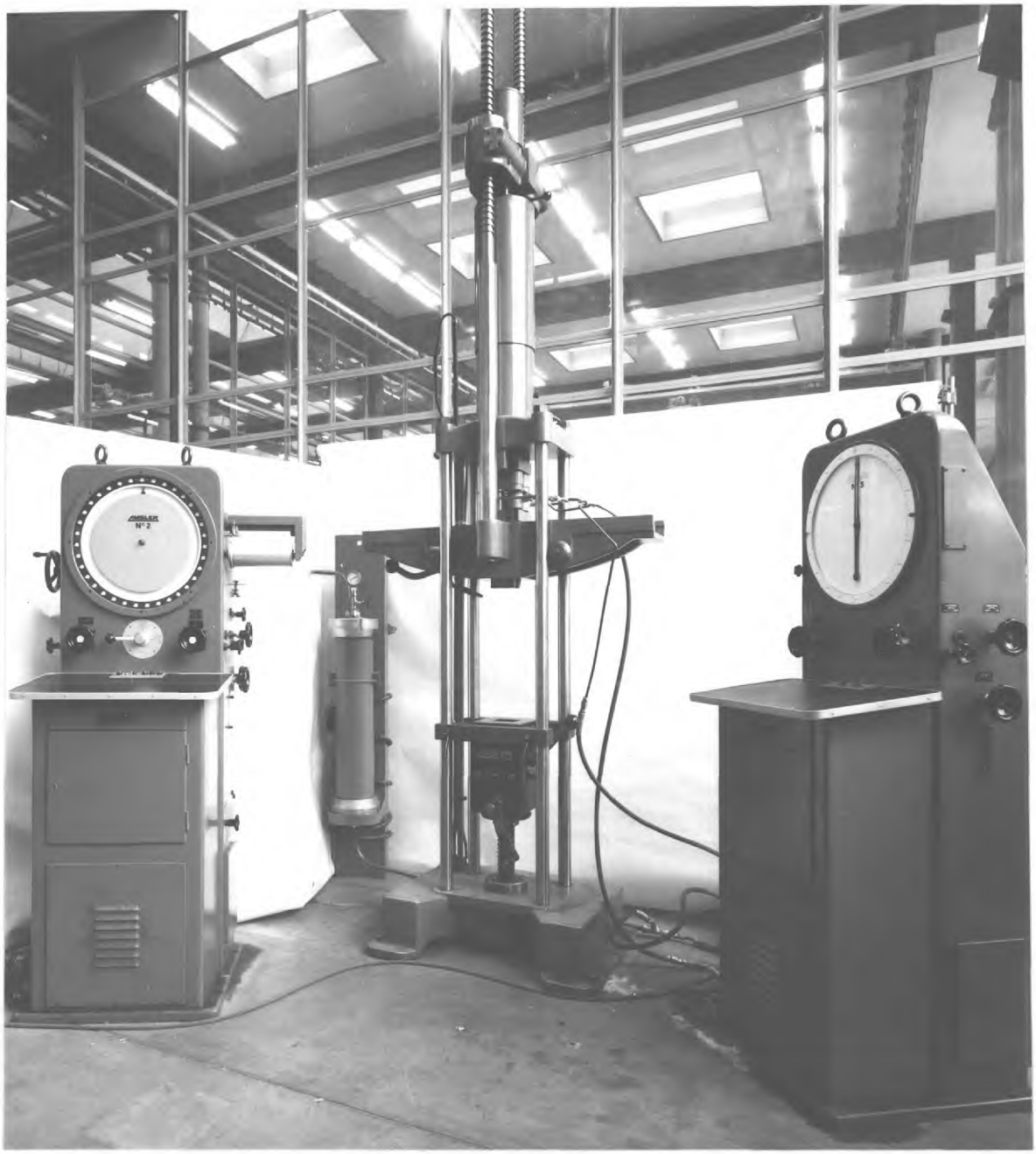

Figure 49 The Low-cycle Test Assembly

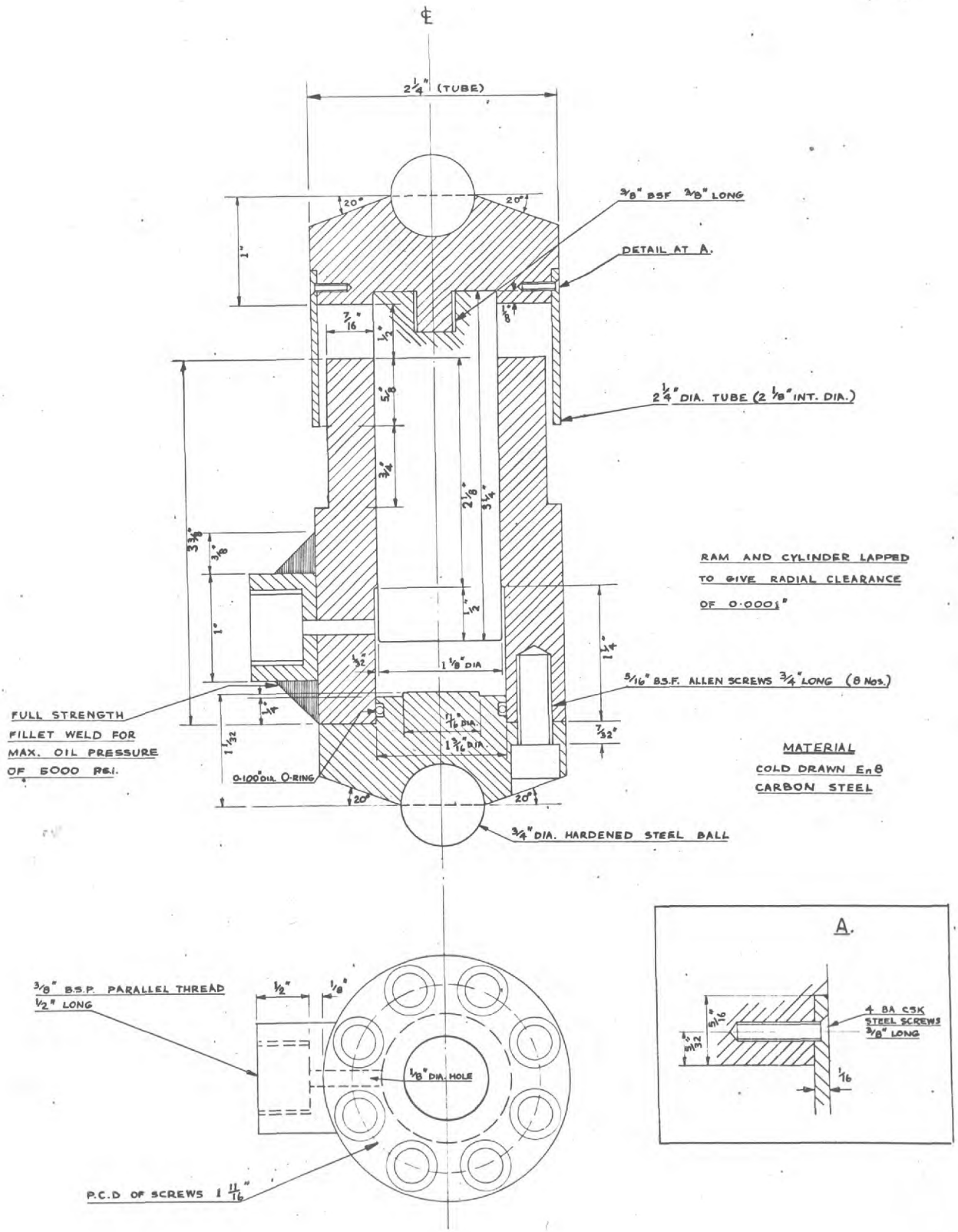

Figure.50. Working drawing of a Lapped ram.

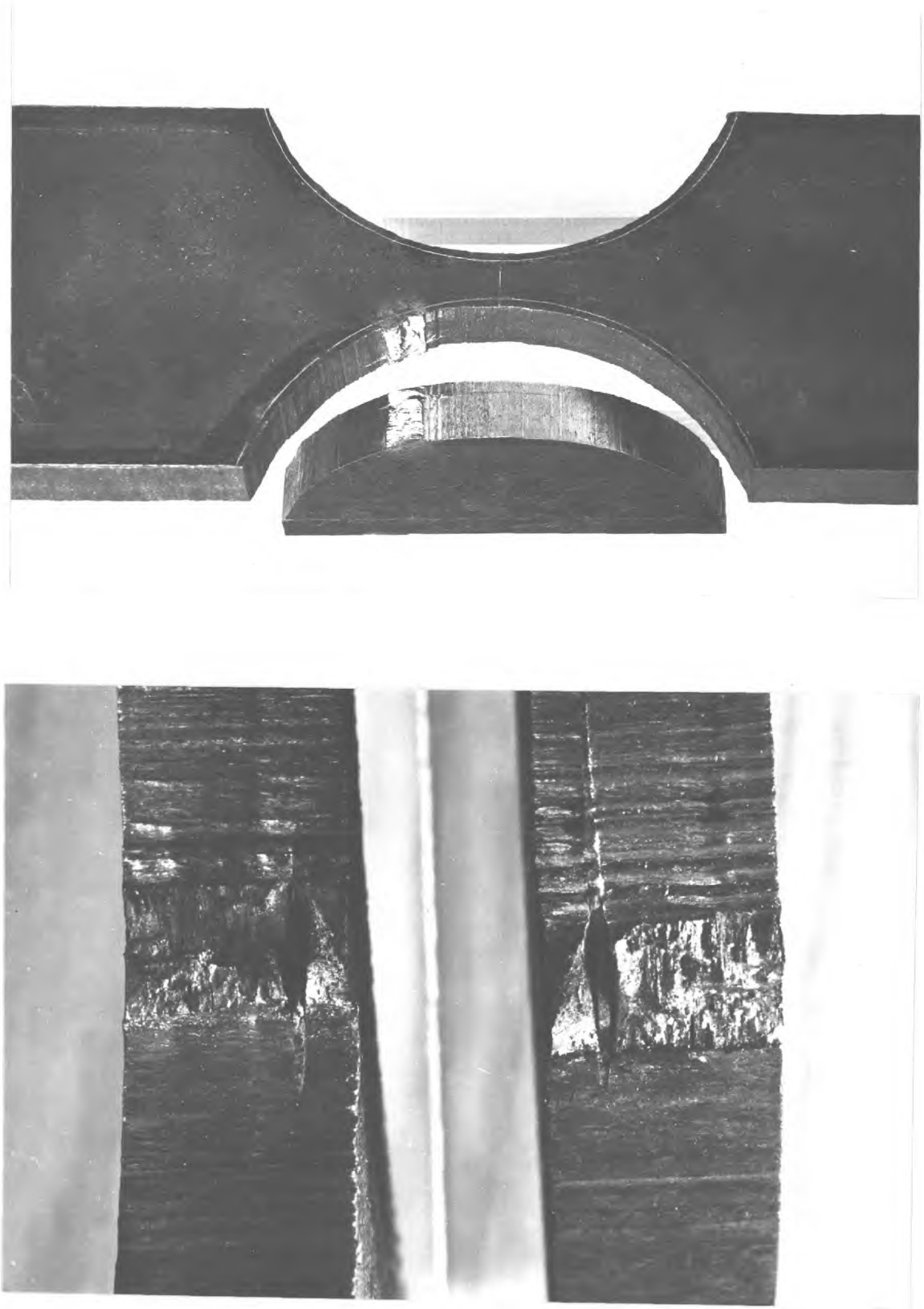

Figure 51 Flaw (Inclusion)

Figure 52 Flaw (Lamination)

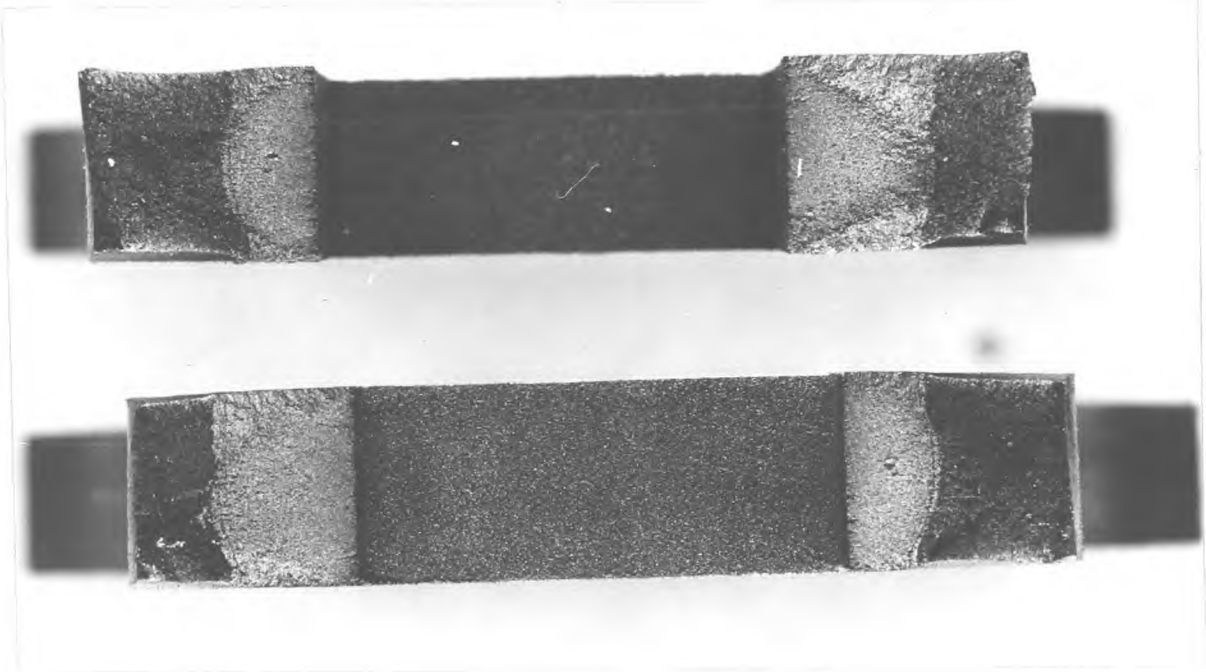

Figure 53 Fracture (Low-cycle Fatigue)

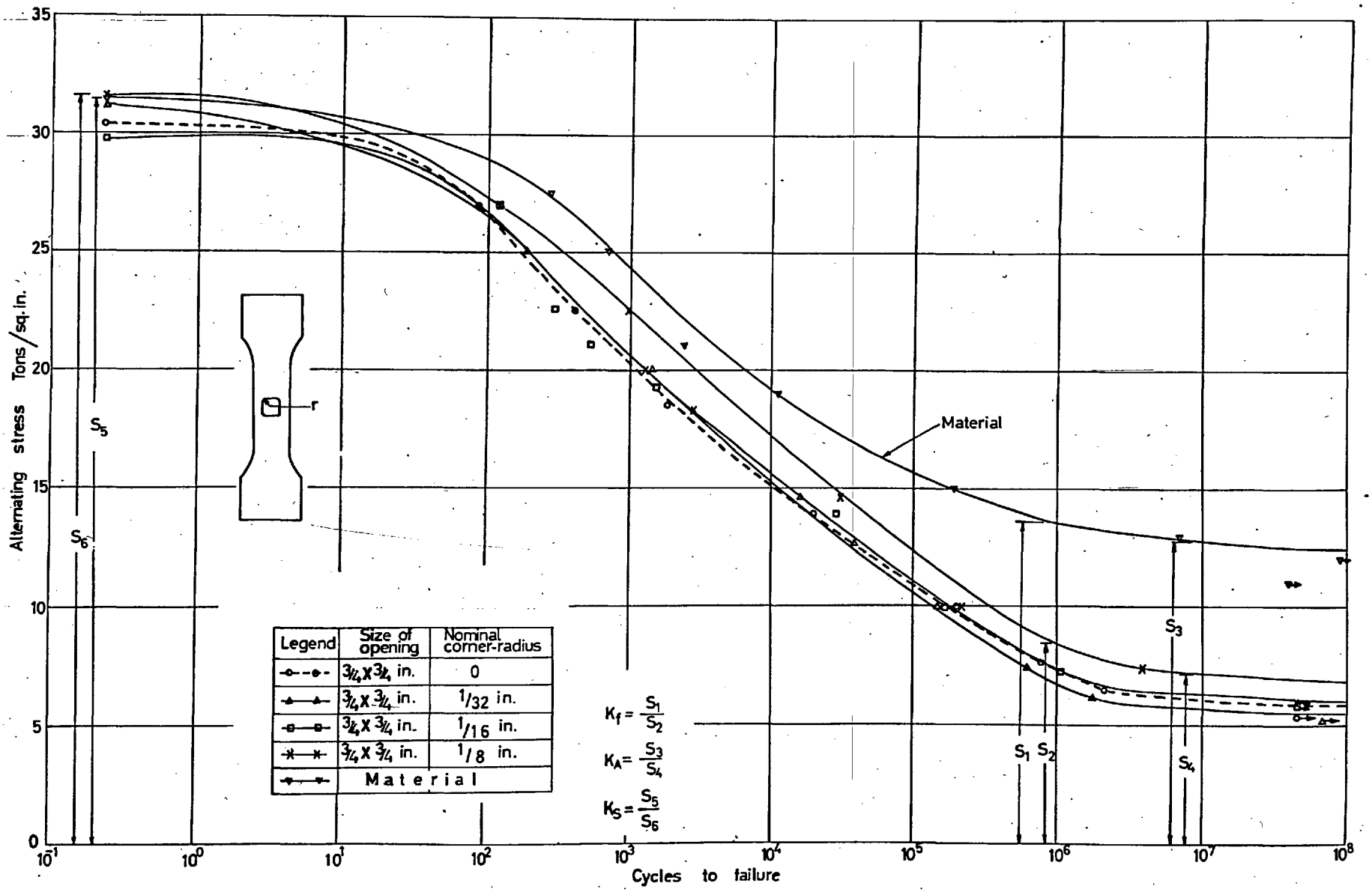

Figure.54. S-N diagram showing the effect of corner-radius (r) on the fatigue strength of plate specimens with square openings.

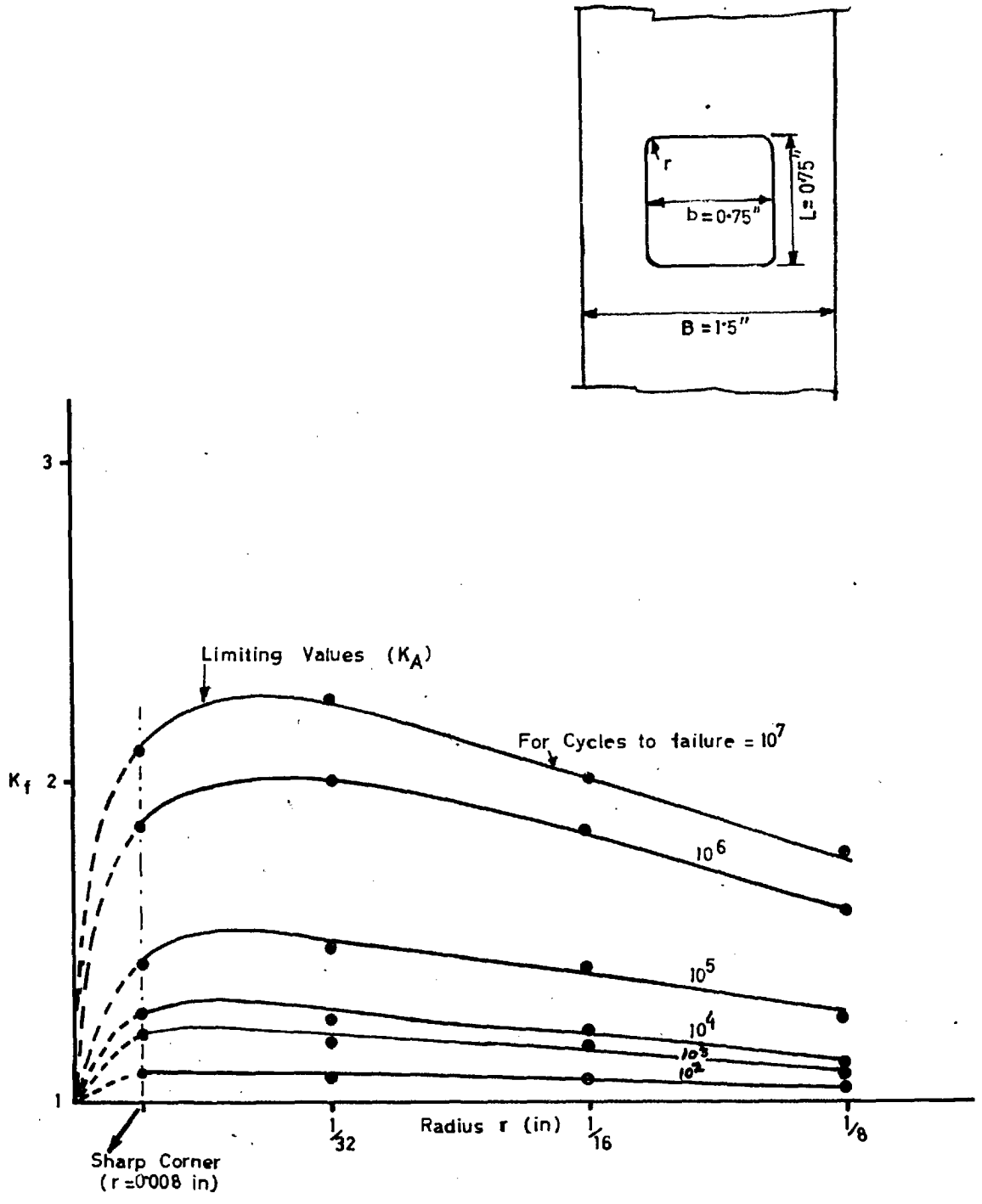

Figure.55. Variation of observed fatigue strength reduction factor with corner-radius, for specimens with square openings.

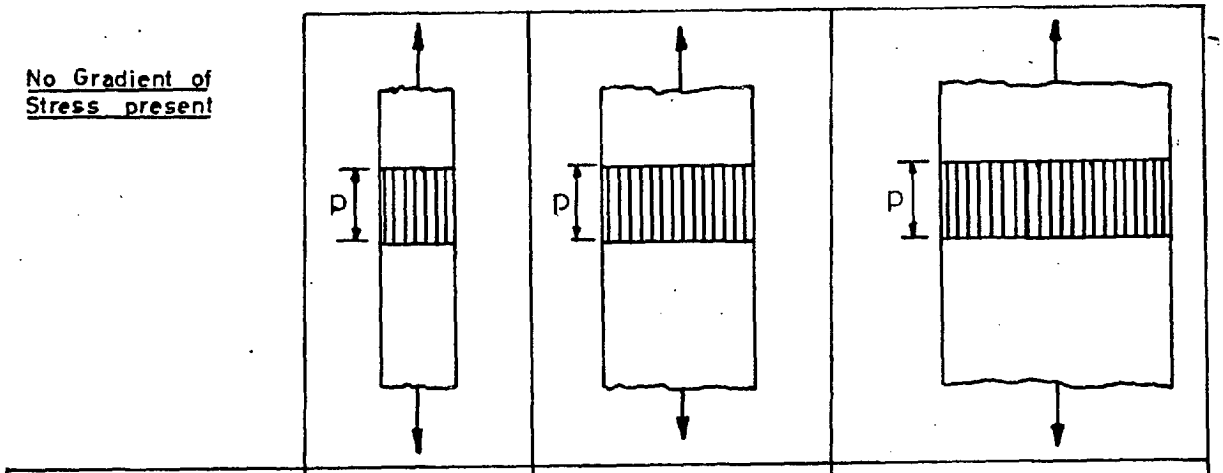

$$(\sigma_A)_1 = (\sigma_A)_2 = (\sigma_A)_3$$ NO SIZE-EFFECT

Case 1. Axially Loaded Specimens

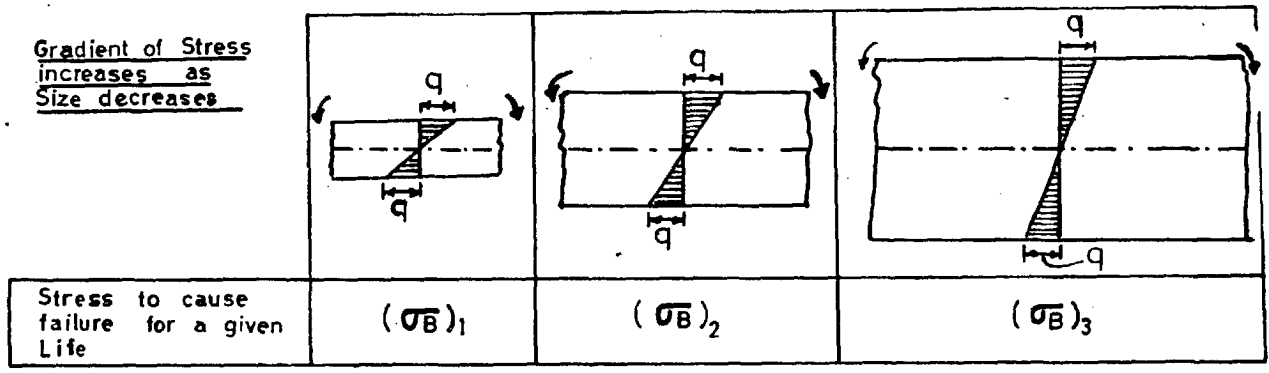

$$(\sigma_B)_1 > (\sigma_B)_2 > (\sigma_B)_3$$ SIZE-EFFECT PRESENT

Case 2. Specimens in Bending

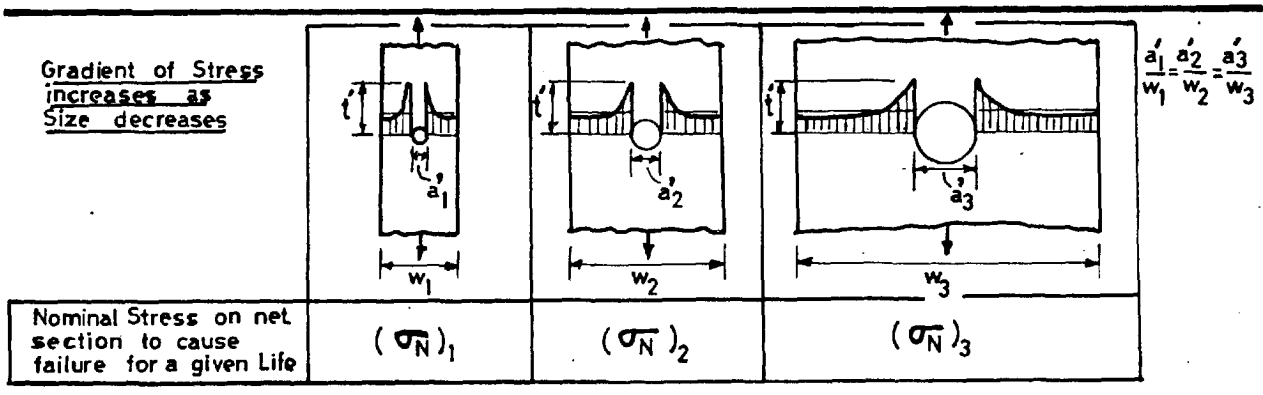

$$(\sigma_N)_1 > (\sigma_N)_2 > (\sigma_N)_3$$ SIZE-EFFECT PRESENT

Case 3. Notched Specimens

Figure.56. Relation between Stress-gradient and Size effect in Fatigue

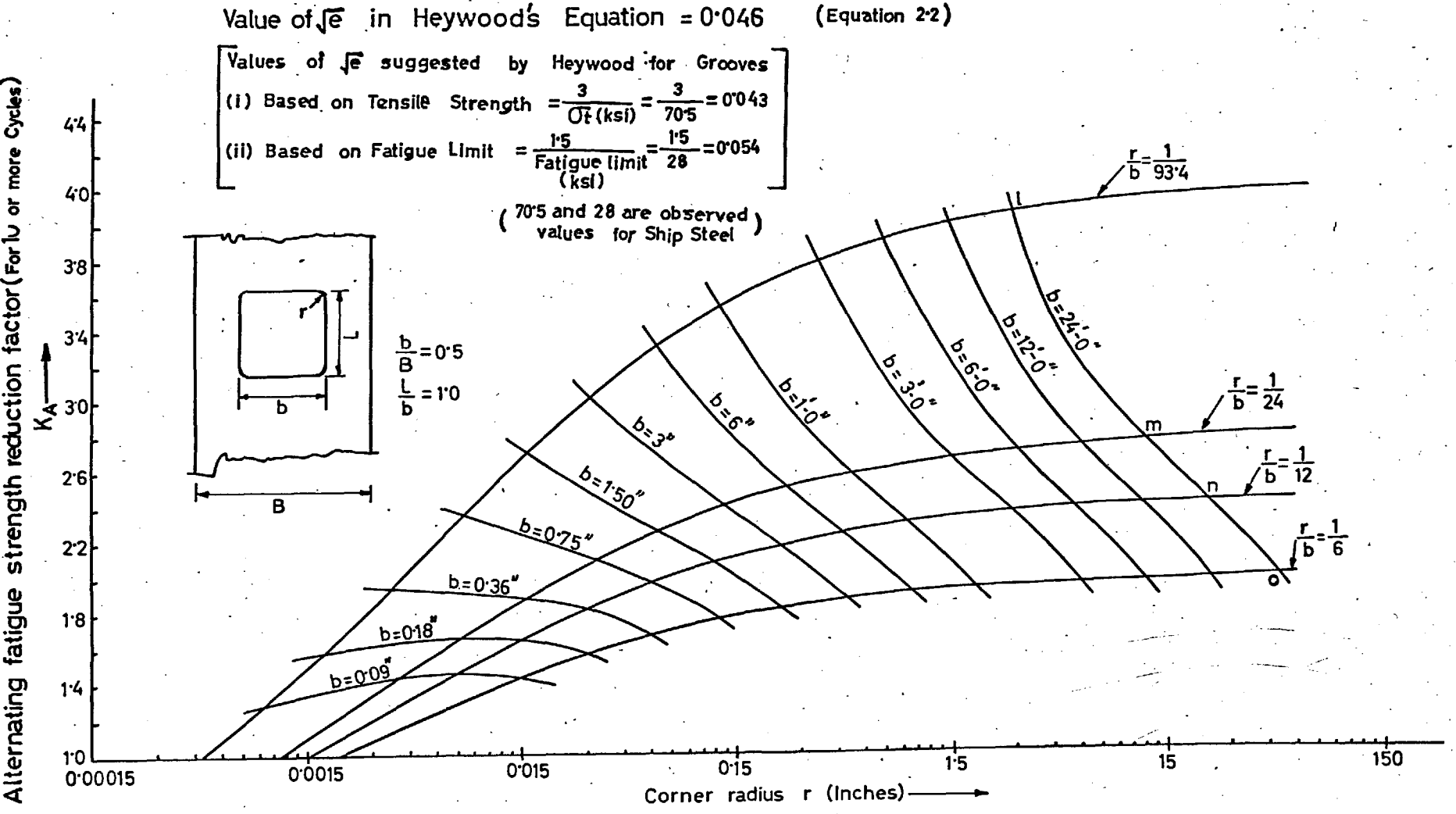

Figure.57. Fatigue Strength Reduction for Geometrically Similar Specimens.

$K_f = K_S + \psi(K_A - K_S)$ ---------(i)

where $\psi = \frac{n^4}{n^4+d}$

n = Log. of cycles to failure

$d = \left[\frac{1750}{\sigma_t}\right]^2$; σ_t = Ultimate tensile strength (Ksi)

For ship steel used $\sigma_t = 70{\cdot}5$ Ksi , d = 615

K_f = Fatigue Strength Reduction Factor at 10^n Cycles.

K_A = Limiting Fatigue Strength Reduction Factor

K_S = Static Strength Reduction Factor (Single Pull)

△ ○ × □ Values of ψ obtained by substituting Experimental values of K_f, Ks and K_A in the expression (i)

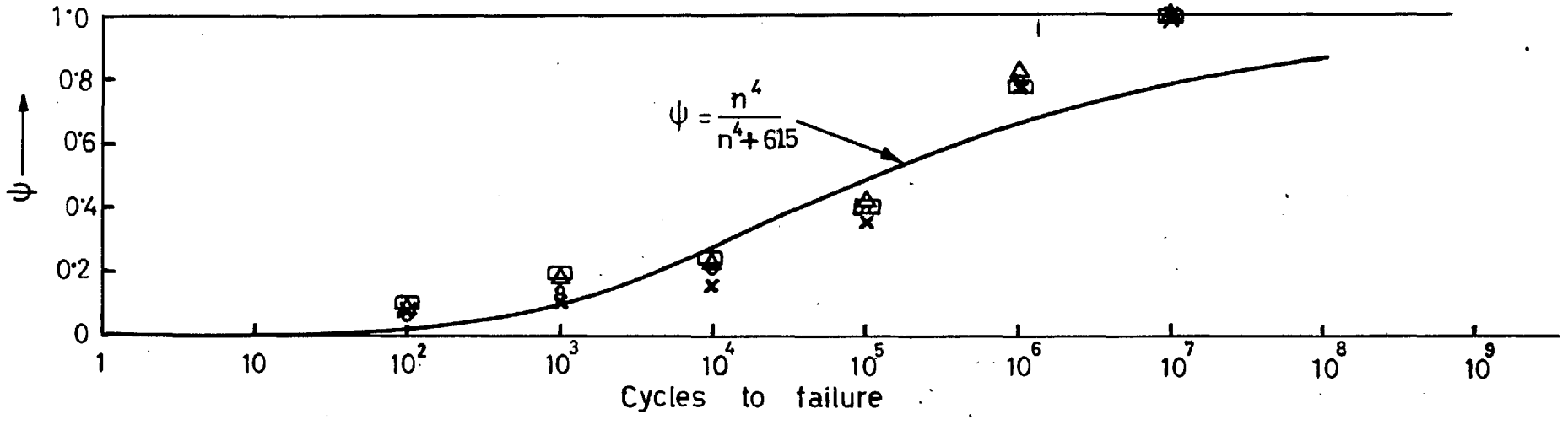

Figure.58. Empirical and Experimental variation of Ψ with Cycles to failure .

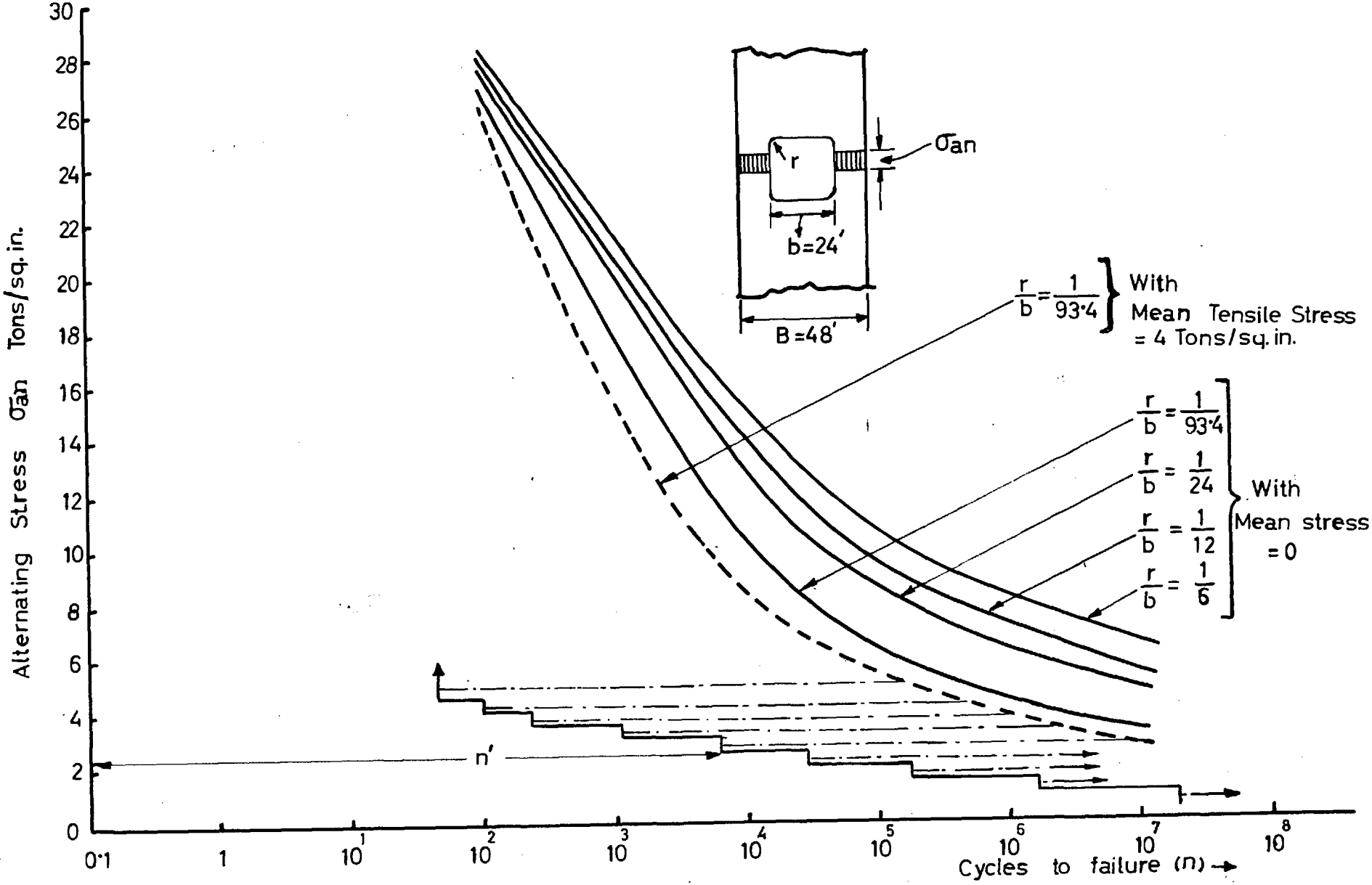

Figure.59. Fatigue performance of a large-size plate specimen with a square opening having radiused corners.

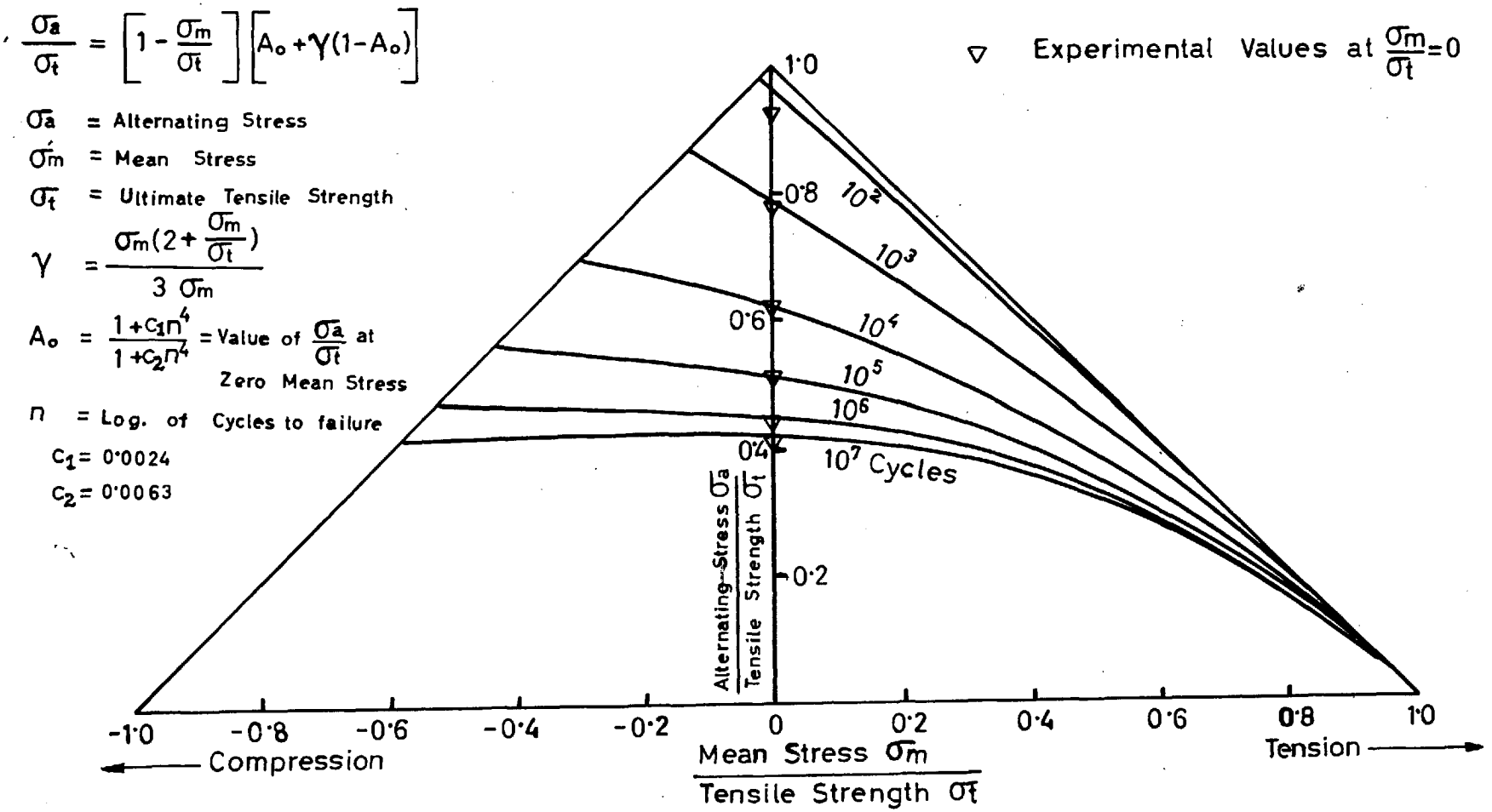

Figure.60. Master Diagram for Ship Steel

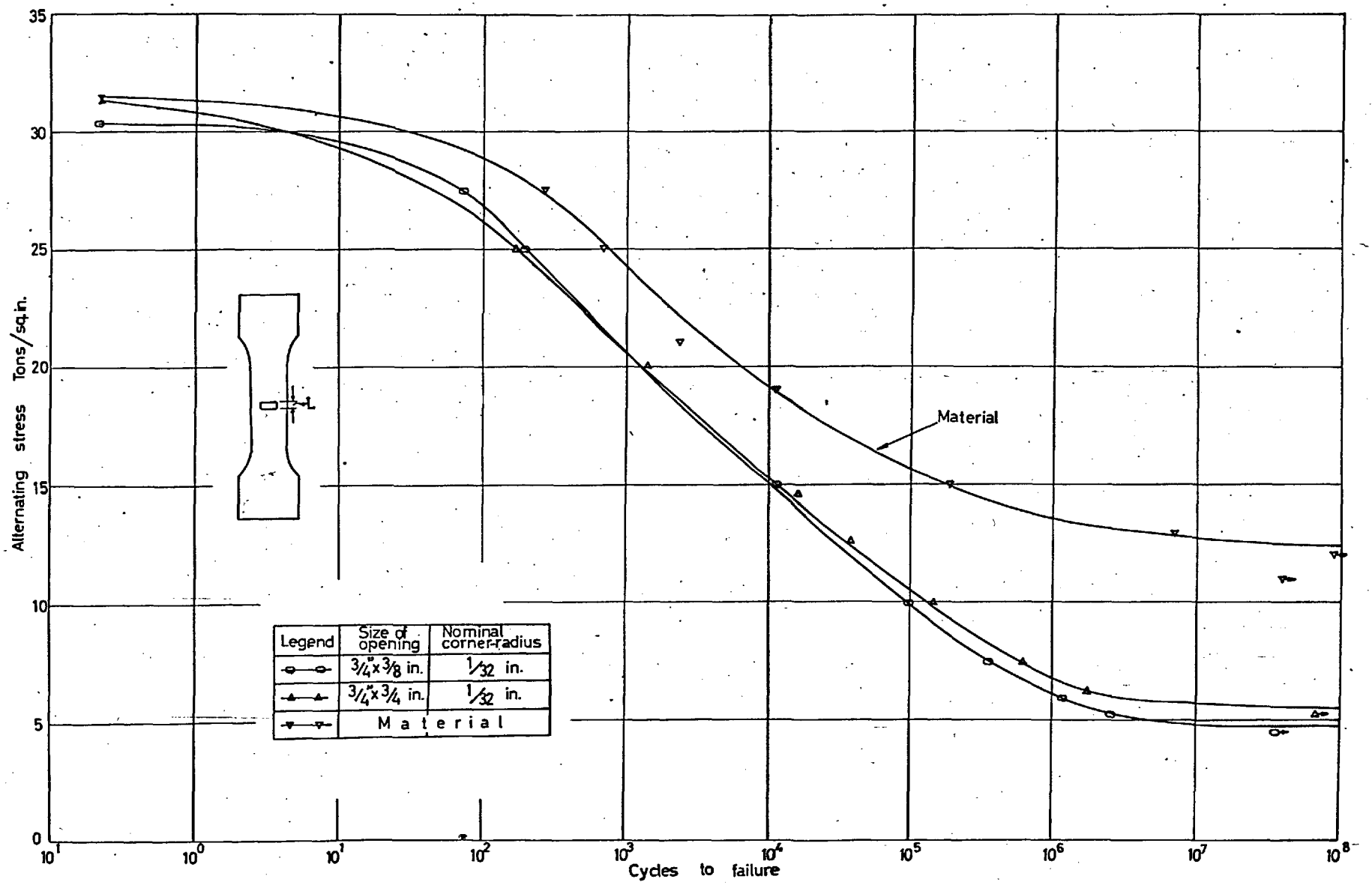

Figure.61. S-N diagram showing the effect of length of opening(L) on the fatigue strength of plate specimens

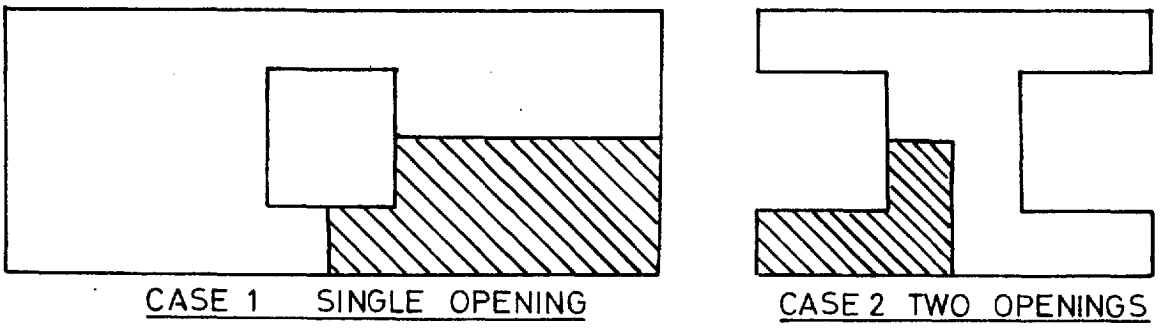

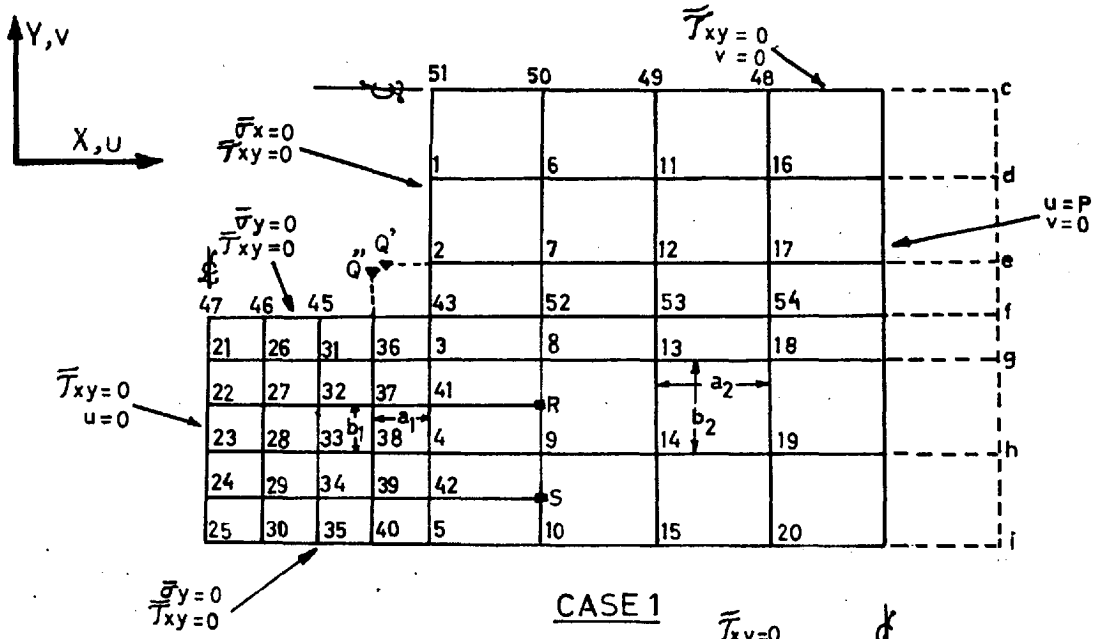

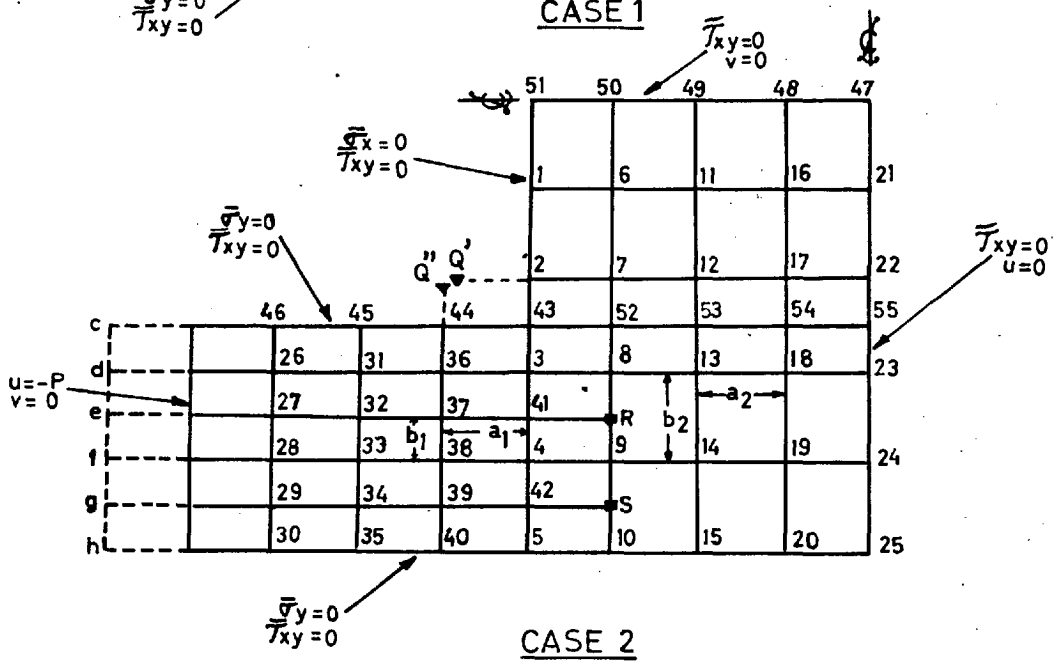

Figure.62. The finite-difference net and boundary conditions (Hatch openings)

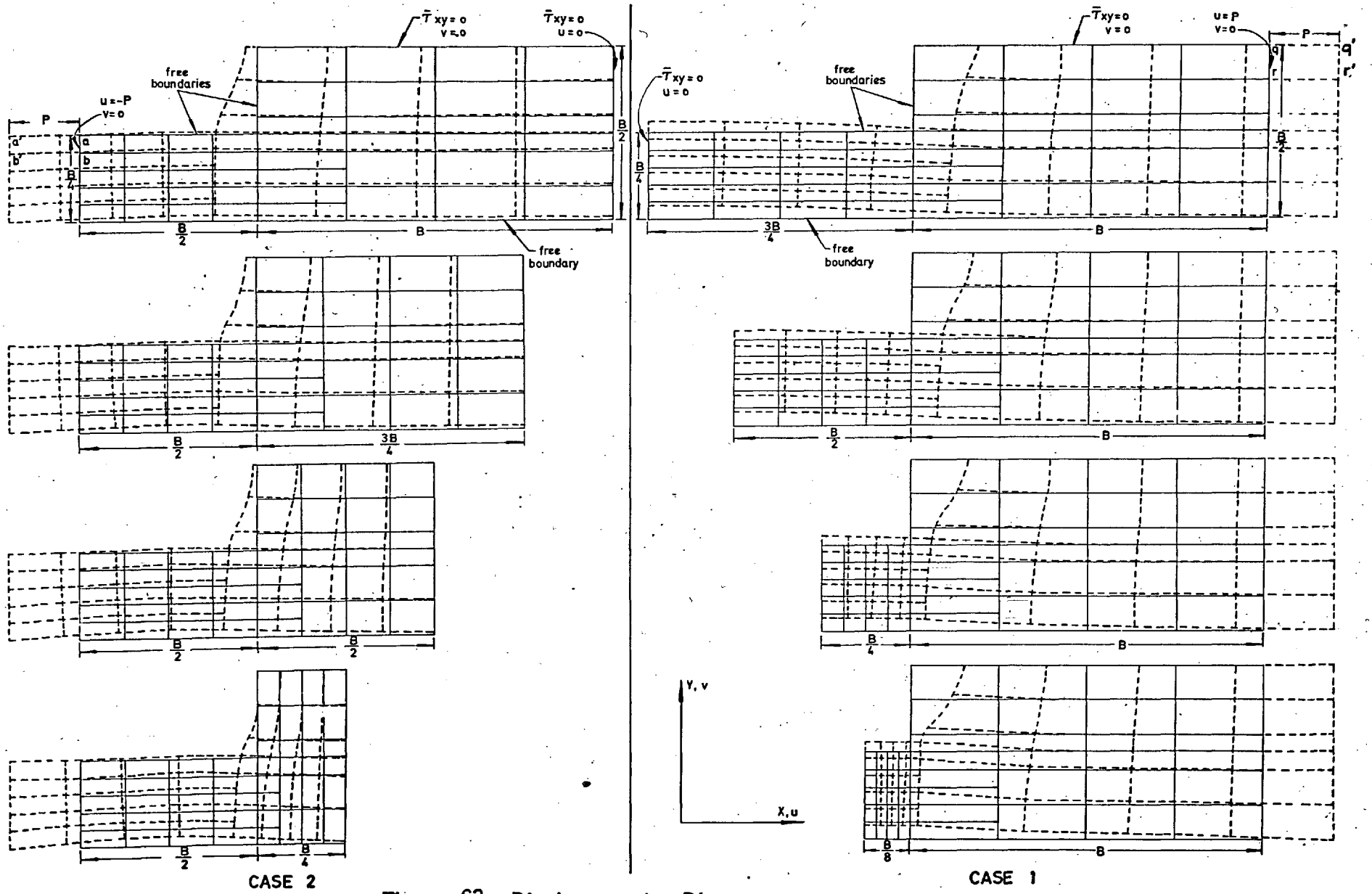

Figure. 63. Displacement Diagrams.

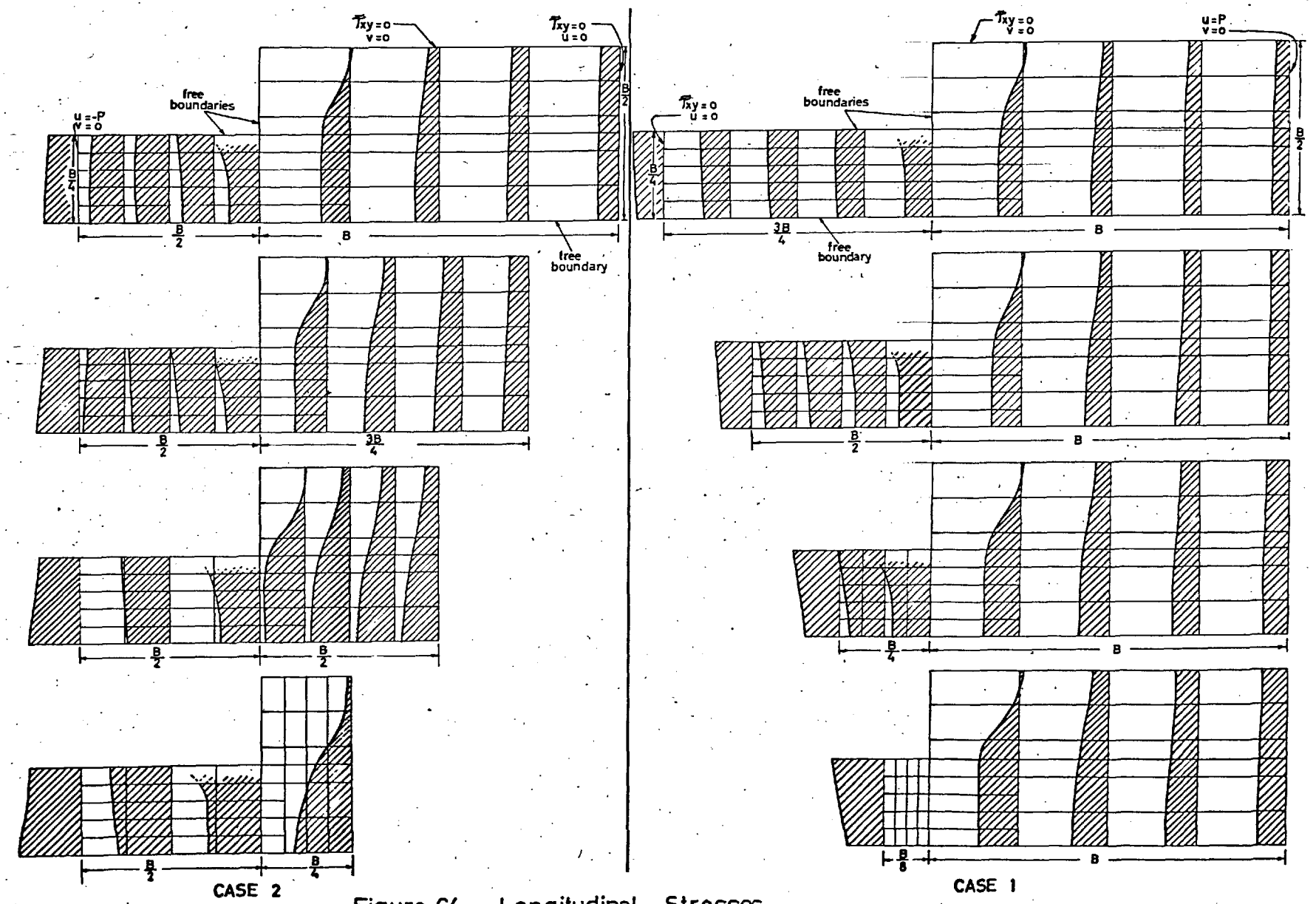

Figure.64. Longitudinal Stresses.

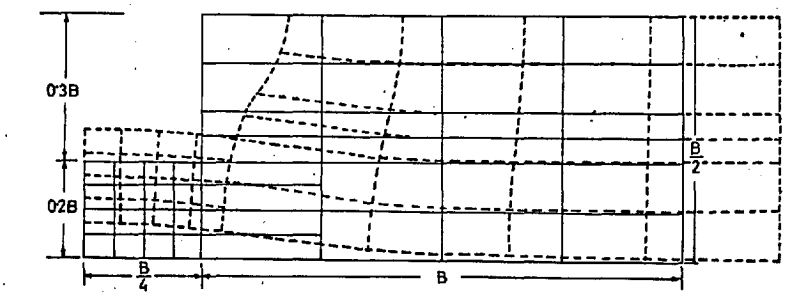

Displacement diagram

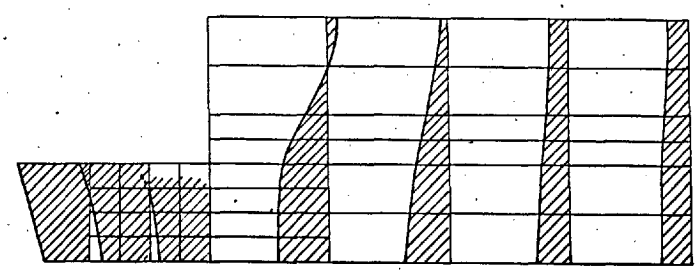

Longitudinal stress

Figure.65. Displacement diagram and Longitudinal stresses for a plate with a single opening of width 60% of the plate-width.